Characterizing Minimum-Time Collision Avoidance Maneuvers for Solar Sails in Earth Orbit

Giuseppe Ambrosio

TU Delft

Characterizing Minimum-Time Collision Avoidance Maneuvers for Solar Sails in Earth Orbit

by

Giuseppe Ambrosio

to obtain the degree of Master of Science in Aerospace Engineering at Delft University of Technology,
to be defended publicly on Thursday, February 27, 2025, at 13:00

Student Number: 5851815

Project Duration: April 2024 - February 2025

Thesis Committee:

Dr.ir. B.C. Root	TU Delft, Chair
Dr.ir. M.J. Heiligers	TU Delft, Supervisor
Dr. S. Gehly	TU Delft, External Examiner
Dr. T. Flohrer	European Space Agency

Faculty: Faculty of Aerospace Engineering, Delft

Preface

And finally also this chapter has come to an end...but what a ride! These years have literally been a rollercoaster. I am lost for words if I look back at the person I was before embarking on this journey, realizing how much I have changed.

All I feel in this moment is gratitude. I am thankful for having been able to complete this stimulating yet challenging experience. I learned so many things, and now I feel a bit more ready to enter the "real world". But I am not at all the only person that I have to thank for having made it. The only thing I had to do was study hard, grit my teeth, and just keep going. And since I am writing this page of my thesis, it means I somehow managed.

Thanks to my mom Cristina, my dad Angelo, and my sister Alina. Everything I have accomplished I owe to you, and I dedicate to you. Making you proud today (not the day I am writing this, but the graduation day) is my only goal. Whenever I feel lost, I know I only need to call you to feel safe again. And no matter how out of place I may feel, I know my place is and always will be next to you.

Thanks to my lifelong best friends: Chiara, Cristina, Giorgia, Irene, Samira (in alphabetical order so no one gets offended). You have been by my side since my hair was short and straight, which means a really long time. My life has changed so much in the last few years: I have changed cities, friends, loves, studies, habits, but you have always been a constant, and a reason to come home. Because when we are together we laugh as if we still saw each other every day.

Thanks to my family in Delft. If I feel at home here, and if I cry at the idea of leaving, the blame and the credit is only yours. Nothing would have been the same without you, and I will cherish all the memories we shared, from studying countless hours to laughing uncontrollably, from our cozy dinners to some crazy parties I will not discuss here. So thanks to Francesco, Giacomo, Luigi, Riccardo (in alphabetical order, again), for being the reason I always want to come back here. No, Ludovica, I have not forgotten about you, I just thought you deserved a separate line: whatever happens in our lives, I know you will be the first person I will think of when they ask me about these years in Delft. You know how much we shared, how much we laughed, and how much we supported each other, so I just wanted to say thank you. And no, I have not forgotten all the other wonderful people I have met in Delft either (I am talking to you, "Pizza" people, "Olimpo" guys, and beyond).

I was talking about feeling at home. I am aware I am extremely lucky, because wherever I have been I have felt at home. Partly, it is because I get attached quickly, but it is also due to the wonderful people I have met on my path. So thank you to anyone who has been a friend to me, anyone who has taught me something, in every place where a piece of my heart is: San Severo, Milan, Lisbon. If I am the person I am today, and we will assume this is a good thing :), I owe it to you as well.

Last but not least, thanks to Jeannette Heiligers, my supervisor, for her support and guidance throughout these months, and to Tim Flohrer, for his invaluable advice.

Giuseppe Ambrosio
Delft, February 2025

Contents

List of Figures

List of Tables

Nomenclature and Constants

Abbreviations

ACS3	Advanced Composite Solar Sail System
ARES	Assessment of Risk Event Statistics
CAM	Collision Avoidance Maneuver
CARA	Collision Avoidance Risk Assessment
CDM	Conjunction Data Message
CoM	Centre of Mass
CSM	Conjunction Summary Message
ECI	Earth-Centered Inertial
ESA	European Space Agency
GEO	Geostationary Earth Orbit
GPOPS-II	General Purpose Optimal Control Software (Second Version)
GPS	Global Positioning System
IADC	Inter-Agency Space Debris Coordination Committee
IKAROS	Interplanetary Kite-craft Accelerated by Radiation Of the Sun
IPOPT	Interior Point Optimizer
LEO	Low Earth Orbit
LGR	Legendre-Gauss-Radau
LTAN	Local Time of the Ascending Node
MATLAB	MATrix LABoratory
NAIF	Navigation and Ancillary Information Facility
NaN	Not-a-Number
NASA	National Aeronautics and Space Administration
NEA	Near Earth Asteroid
NLP	Non-Linear Programming
OCP	Optimal Control Problem
PDF	Probability Density Function
PoC	Probability of Collision
RAAN	Right Ascension of the Ascending Node
RSO	Resident Space Object
RTN	Radial-Transverse-Normal
SMA	Semi-Major Axis
SMD	Squared Mahalanobis Distance
SPICE	Spacecraft, Planet, Instrument, C-matrix, Events
SRP	Solar Radiation Pressure
SSO	Sun-Synchronous Orbit
SWEEP	Space Waste Elimination around Earth by Photon Propulsion
TCA	Time of Closest Approach
TLE	Two-Line Element
UTC	Universal Time Coordinated

Symbols

Roman Symbols

$\tilde{0}$	Zero matrix		K	Generic reference frame	
a	Acceleration	$[\frac{m}{s^2}]$	m	Mass	[kg]
$\mathbf{a}$	Acceleration vector	$[\frac{m}{s^2}]$	M	Encounter frame	
$\tilde{a}$	Semi-major axis	[m]	$\mathbf{n}$	Normal vector	
A	Area	$[m^2]$	N	Number	[-]
$\tilde{A}$	Azimuth angle	[deg]	O	RTN frame of the sail	
A/m	Area-to-mass ratio	$[\frac{m^2}{kg}]$	P	Orbital period	[s]
b	Coefficient of the B matrix		PoC	Collision probability	[-]
B	Dynamics sub-matrix		q	Regression function	
C	Position covariance matrix	$[m^2]$	Q	RTN frame of the debris	
d	SMD	[-]	r	Position	[m]
e	Eccentricity	[-]	$\mathbf{r}$	Position vector	[m]
$\mathbf{e}$	Unit vector		R	Rotation matrix	
$\tilde{E}$	Eccentric anomaly	[deg]	$\tilde{R}$	Radius	[m]
$\mathbf{f}$	Dynamics function		s	Size	$[m^2]$
g	Generic function		S	Sunlight frame	
G	Dynamics matrix		t	Time	[s]
h	Angular momentum	$[\frac{m^2}{s}]$	tol	Tolerance	
$\mathbf{h}$	Angular momentum vector	$[\frac{m^2}{s}]$	$\mathbf{u}$	Control vector	
$\tilde{h}$	Altitude	[m]	v	Velocity	$[\frac{m}{s}]$
i	Inclination	[deg]	$\mathbf{v}$	Velocity vector	$[\frac{m}{s}]$
I	ECI frame		W	Energy flux	[W]
$\tilde{I}$	Identity matrix		$\hat{\mathbf{x}}$	First basis vector	
J	Cost function		$\hat{\mathbf{y}}$	Second basis vector	
$J2$	J2 coefficient		$\hat{\mathbf{z}}$	Third basis vector	

Greek Symbols

α	Cone angle	[deg]	$\boldsymbol{\lambda}$	Optimal direction	
β	Aspect angle	[deg]	μ	Gravitational parameter	$[\frac{m^3}{s^2}]$
γ	Distance from the Sun	[m]	ν	Shadow factor	[-]
δ	Clock angle	[deg]	ξ	Encounter angle	[deg]
$\tilde{\delta}_{\tilde{j},\tilde{i}}$	Kronecker delta	[-]	$\boldsymbol{\rho}$	State vector	
$\Delta\mathbf{r}$	Relative position	[m]	σ	Position standard deviation	[m]
Δt	Maneuver time	[s]	τ	Regression coefficient	
$\Delta\mathbf{v}$	Relative velocity	[m/s]	Φ	State transition matrix	
ϵ	Small perturbation		$\boldsymbol{\psi}$	Direction of basis vector	
ζ	Time interval before TCA	[s]	ω	Argument of perigee	[deg]
η	Efficiency	[-]	Ω	RAAN	[deg]
θ	True anomaly	[deg]			

Indexes

Superscripts

T	Transpose
ψ	Direction of basis vector

Subscripts

0	Initial
abs	Absolute
c	Characteristic
CDM	CDM
$circ$	Circumscribing Sphere
$class$	Orbital class
D	Debris
dim	Size
e	Eccentricity
E	Earth
f	Final
$guess$	Initial guess
i	Inclination
I	Inertial frame
$\tilde{i}$	Generic row
$\tilde{j}$	Generic column
$J2$	J2 perturbation
k	Generic object
K	Generic reference frame
M	Encounter frame
MAN	Maneuver
max	Maximum
min	Minimum
$miss$	Miss vector
new	New iteration
O	RTN frame of the sail
old	Old iteration
opt	Optimal
p	Perigee
Q	RTN frame of the debris
rel	Relative
req	Required
S	Sunlight frame
S/C	Sail
SRP	SRP perturbation
TLE	TLE
x	Coordinate along $\hat{\mathbf{x}}$
$\hat{\mathbf{x}}_Q$	$\hat{\mathbf{x}}_Q$ direction
$(\hat{\mathbf{x}}_M, \hat{\mathbf{z}}_M)$	Projection onto encounter plane
y	Coordinate along $\hat{\mathbf{y}}$
$\hat{\mathbf{y}}_Q$	$\hat{\mathbf{y}}_Q$ direction
z	Coordinate along $\hat{\mathbf{z}}$
$\hat{\mathbf{z}}_Q$	$\hat{\mathbf{z}}_Q$ direction
$\mu_\oplus$	Earth's central gravity
Ω	RAAN

Notation

w	Scalar/Norm of vector
$\mathbf{w}$	Vector
$\hat{\square}$	Unit vector/Direction
$\dot{\square}$	First-order derivative
$\ddot{\square}$	Second-order derivative
$\frac{d}{dw}$	Total derivative with respect to w
$\frac{\partial}{\partial w}$	Partial derivative with respect to w
$\lvert\square\rvert$	Module/absolute value operator
$\lVert\square\rVert$	Norm operator
$\Delta\square$	Difference operator
$\cdot$	Scalar product
$\times$	Cross product

Physical Quantities

deg	degree
g	gram
m	meter
N	Newton
s	second
W	Watt

Astronomical Symbols

$\oplus$	Earth
$\odot$	Sun
Υ	First point of Aries

Number Sets

$\mathbb{R}$	Real numbers

Prefixes

c	centi	10^{-2}
k	kilo	10^{3}
m	milli	10^{-3}

Units

au	Astronomical unit	$1\,49597870700 \cdot 10^{11}$ m (Wakker, 2015)
day	Mean solar day	86400 s (Wakker, 2015)

Constants

$\tilde{c}$	Speed of light	$2.99792458 \cdot 10^{8}$ $\frac{\mathrm{m}}{\mathrm{s}}$ (Wertz and Larson, 1991)
$J2$	J2 coefficient	$1.082626925639 \cdot 10^{-3}$ (Wertz and Larson, 1991)
$\tilde{R}_{\oplus}$	Mean Earth's equatorial radius	6378.14 km (Wakker, 2015)
$\tilde{R}_{\odot}$	Mean solar radius	$6.95508 \cdot 10^{5}$ km (Wakker, 2015)
W_E	Mean solar flux at Earth	1361 $\frac{\mathrm{W}}{\mathrm{m}^2}$ (Wakker, 2015)
$\mu_{\oplus}$	Earth's gravitational parameter	$3.986004418 \cdot 10^{14}$ $\frac{\mathrm{m}^3}{\mathrm{s}^2}$ (Wakker, 2015)

Executive Summary

Nowadays, solar sails are being considered for a plethora of applications around Earth, due to their ideally infinite lifetime. As a matter of fact, their thrust generation mechanism does not rely on a finite reaction mass, but on an ambient source: Solar Radiation Pressure (SRP). Envisioning their applications in Earth orbit, collision avoidance analyses ought to be conducted. Collision avoidance operations are indeed a reality for all spacecraft orbiting Earth, due to the increasing number of space-debris objects. Conjunction Data Messages (CDMs) are sent to notify spacecraft operators of threatening encounters, and the flight control team decides whether to maneuver based on the value of the Probability of Collision (PoC).

Literature, however, has so far neglected the investigation of Collision Avoidance Maneuvers (CAMs) for solar sails around Earth, and only considered CAMs for sails in the deorbiting phase. Therefore, the objective of the thesis is to investigate, for the first time, the performance of solar sails in executing collision avoidance maneuvers. CAMs that require the minimum time, before the closest approach, are targeted.

The dynamical model comprises, along with Earth's central gravity, perturbations due to Earth's oblateness (the J2 effect) and SRP. Atmospheric forces are neglected since the minimum operating altitude is assumed to be 1000 km, where such effects are negligible. A conical model is employed for the eclipses, and simulations are centered around the vernal equinox, which represents the "worst-case scenario" in terms of the fraction of the orbit spent in shadow by a satellite around Earth.

For a comprehensive and realistic set of conjunctions to be built, different values of area-to-mass ratios are selected, taking the latest flown Advanced Composite Solar Sail System (ACS3) mission as a reference. The sail state, at the point of closest approach, is defined in terms of altitude, inclination, right ascension of the ascending node, and illumination condition. The debris state is characterized by the miss vector (in magnitude and direction) and the angle between the velocities of the two objects at the closest approach. Moreover, the debris size is varied, given its influence on the PoC computation (through Foster's method) and uncertainty retrieval. To derive uncertainties, a mapping factor is obtained, for a reference orbital class, between the regression functions coming from the Two-Line Elements (TLEs) uncertainty propagation and from a publicly available CDM dataset. The mapping factor is then applied to all orbital classes.

The optimization is carried out, by means of the second version of the General Purpose Optimal Control Software (GPOPS-II), to search for time-optimal maneuvers while constraining the collision probability. Based on the choice of the PoC to be targeted by the maneuver and of the time interval between the position uncertainty retrieval and the maneuver execution, two scenarios are created: an "ideal" and a "real" (more conservative) case. In the former, the covariance is retrieved exactly at the maneuver start epoch, and the target PoC for the maneuver is 10^{-4}; in the latter, a decision time is introduced, thus the covariance is retrieved one day before the maneuver start epoch, and the target PoC is 10^{-6}.

For all considered scenarios, the total maneuver time is below one day, which is regarded as the latest time to decide whether to execute a maneuver. CAMs for solar sails are therefore feasible, as

the results fit the current operational framework. The average maneuver time is 25 and 47 minutes, in the "ideal" and "real" cases, respectively. The maneuver time is intuitively longer in the "real" case, yet most maneuvers (99% of the scenarios) do not exceed two orbital revolutions. A relation between collision probability and maneuver time is identified, through the parameters that define the debris state and position uncertainty. The better the knowledge of the debris state, the shorter the maneuver time. Also, a negative correlation, for the maneuver time, is found with the area-to-mass ratio, and a positive one with the altitude. Solar-sail-specific effects are highlighted. First, eclipses cause an increase in the maneuver time, since sails cannot be maneuvered when in shadow. Second, if the debris is displaced along the sunlight direction, the sailcraft will tend to move toward (rather than escape from) the object, yielding longer maneuver times. The orbit orientation mainly affects the optimal control profile but does not significantly impact the maneuver time, which is thus independent of the Earth-Sun configuration.

In terms of the optimal thrusting profile throughout the maneuver, it is found that the sail largely thrusts along the direction of sunlight and that there is always an in-plane component of the sail acceleration. This shows that in-plane maneuvering is unavoidable to execute CAMs. The locally optimal control laws that better approximate the final state of the sailcraft obtained by the optimized maneuvers are those to change either the semi-major axis or the eccentricity, which indeed require an in-plane acceleration. In the "real" case, characterized by longer maneuver times, simulating the locally optimal steering complies with the PoC requirement at the closest approach in most scenarios (95%). This could streamline solar-sail CAM planning.

1 Introduction

The problem of space waste originated at the dawn of space exploration, but only more recently it has been recognized as a global threat, that could hamper access to space. For this reason, space agencies are acting to reduce debris production and to enhance mitigation strategies, for instance by investing in active debris removal applications.

Amongst other propulsive methods, solar sails are considered for active debris removal, due to their propellantless nature. Thrust generation relies on solar radiation pressure, through photons, which is converted into force upon reflection and momentum transfer. Envisioning the usage of solar sails in Earth orbit requires assessing their performance in executing collision avoidance maneuvers.

Collision avoidance is indeed a reality for every mission around Earth, and the number of conjunction data messages, sent to inform satellite operators about a dangerous encounter, is growing as the amount of space objects increases. Upon the notification of a close approach with a threatening object, it is decided whether to execute a maneuver based on the value of the probability of collision.

However, studies on collision avoidance for solar sailing missions are limited to considering deorbiting sails. Literature is therefore lacking studies to characterize the performance of solar sails in executing collision avoidance maneuvers. This thesis aims at investigating such performance, for a plethora of scenarios. Specifically, minimum-time maneuvers are targeted, to identify the "dead zone", after which the collision probability cannot be reduced below a set threshold, for the different simulated scenarios.

The thesis structure is as follows. First, relevant background information, from existing literature, is provided in Chapter 2. Second, the research gap is identified in Chapter 3, and the research objective and questions are formulated. Then, Chapter 4 outlines the design choices regarding the dynamical model, the collision scenario, and the optimization setup, explaining the simplifying assumptions and the implemented algorithms. The results of the thesis project are presented in the form of a research paper, in Chapter 5. Finally, the research questions are answered, and suggestions for future work are provided, in Chapter 6. Supplementary information, deemed necessary for a better understanding of the content of the thesis, is given in the Appendices, from Page 81.

2
Literature Review

This chapter introduces relevant pieces of literature, used to outline the research gap that leads to formulating the objective of the thesis project. The chapter is articulated in four main sections. Firstly, in Section 2.1, the issue of space debris is introduced. Secondly, Section 2.2 presents a promising propulsion method for several mission applications around Earth: solar sailing. Thirdly, the potential danger of a space collision is dealt with in Section 2.3. Finally, Section 2.4 presents existing research regarding collision avoidance maneuver design for a sail.

2.1 Space Debris

Space is not an infinite resource, and it should be treated as such (Byers and Boley, 2023). The threats posed by the presence of space debris orbiting Earth are multiple: unique applications and functionalities on which humanity relies could be lost (Peter, 2024). In this section, the overview of the population of space objects is given in Subsection 2.1.1, while Subsetion 2.1.2 presents potential mitigation strategies.

2.1.1 Orbital Population

Figure 2.1, from the space environment report by the European Space Agency (ESA) (ESA's Space Debris Office, 2024), shows the increasing trend in the evolution over time of the number of tracked space objects: the objects which stay in orbit around Earth are a substantial fraction of the total number of objects ever launched into space.

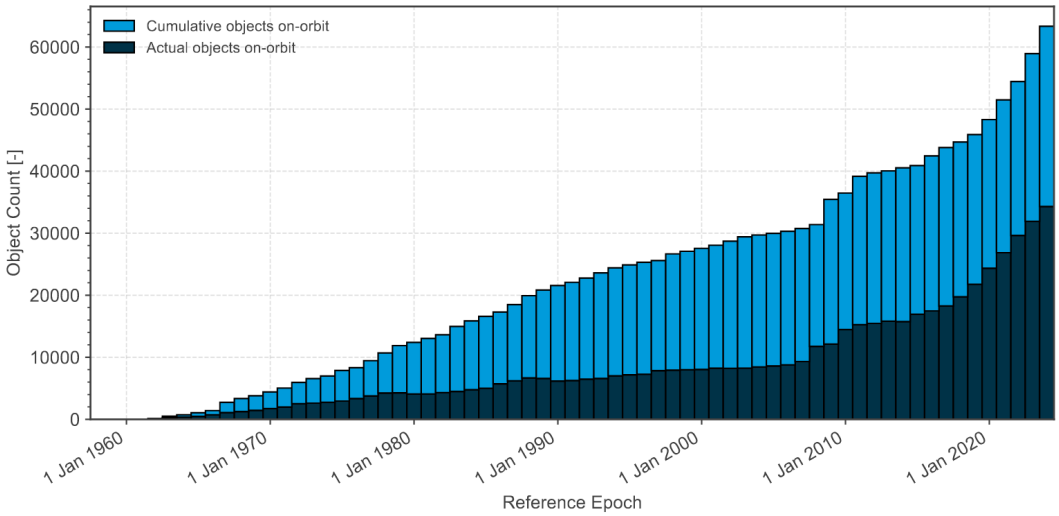

Figure 2.1: Evolution over time of the number of tracked space-debris objects currently in orbit, compared to the total number of objects ever launched into space (ESA's Space Debris Office, 2024)

In his thorough characterization of space debris, Klinkrad (2006) started from the first launch of a satellite in orbit, in 1957. Objects released into space result from launch activities, with the deployment of payloads, upper stages, and associated mission-related objects; further items are released unintentionally, such as slag particles of solid rocket motor burns. The most important single source of space objects is on-orbit explosions of spacecraft and rocket stages. A non-negligible source of debris is collisions, as space debris is so abundant that impacts are frequent, usually at very high relative velocities.

The debris population (as of November 2016) is composed of (ESA's Space Debris Office, 2024):

- 34,000 objects greater than 10 cm;
- 900,000 objects from 1 to 10 cm;
- 128 million objects from 1 mm to 1 cm.

Among such objects, quasi-deterministic information is available only for large-sized ones, due to limitations in the sensitivities of ground-based radars (for lower altitudes) and optical telescopes (for higher altitudes) (Rossi, 2004). For tracked objects, datasets are available, with the most comprehensive being the satellite situation report from the National Aeronautics and Space Administration (NASA), together with the so-called Two-Line Element (TLE) catalog (Klinkrad, 2006). Data can be publicly accessed [1]. More than 90% of the catalog is represented by uncontrollable space debris.

One of today's challenges is to foresee the future evolution of space debris. The task can be cumbersome due to the unpredictability of several factors, from the number of launches to the success of removal strategies. ESA's Space Debris Office (2024) simulated that an unstable environment with collision rates increasing exponentially will be reached, if no modifications are made to the current behavior; nevertheless, even under the "no future launches" scenario, the amount of debris objects is observed as increasing in all cases. The debris population is indeed expected to grow exponentially, just like every other natural population (Lewis and Marsh, 2021).

Rossi (2004) modeled the debris population similarly to the asteroid belt, since a process of high–velocity mutual collisions is present. The situation is more complex than for the asteroids, because, around Earth, the source and sink mechanisms are (partially) subject to human control, as shown in Table 2.1: in red are the perturbations, beyond human control, in yellow are the proliferation mechanisms, which can be mitigated if preventive measures are taken, and in green are the launches and removal strategies, which solely depend on human activity.

Source	Sink
Launches	Non-gravitational perturbations
Explosions	Gravitational perturbations
Collisions	Removal/Mitigation strategies

Table 2.1: Main sources and sinks in the long-term evolution of the space-debris population (based on Rossi (2004)): red, yellow, and green indicate null, partial, and total reliance on human interaction, respectively

What is important is to prevent what was theorized by Kessler and Cour-Palais (1978): a process of mutual collisions between the objects presently in orbit that could lead to the creation of a debris belt surrounding the planet and jeopardizing, if not preventing, all space activities. The phenomenon,

[1] https://www.space-track.org (Accessed: 22 April 2024)

known as the "Kessler's syndrome" would be detrimental to humanity, as essential utility services heavily rely on the space segment (Mariappan and Crassidis, 2023).

2.1.2 Debris Mitigation

To preserve access to space, ESA has the bold goal of significantly limiting the production of debris in Earth and lunar orbits by 2030 for all future missions: the so-called "Zero Debris Approach" (ESA's Space Debris Mitigation working group, 2023). Its main pillars focus on reducing in-orbit collisions (also improving risk assessment performed on ground) and guaranteeing a safe and successful disposal of the orbiting spacecraft, which includes investigating removal strategies.

When dealing with debris removal strategies, a distinction ought to be made between passive and active methods: passive methods require no further active control after deployment, whereas active methods involve separate, dedicated spacecraft that attach to decommissioned satellites to place them into decaying or graveyard orbits (NASA, 2024). Solar sailing technologies can be applied both to passive and active debris removal missions.

The studies by Colombo et al. (2017, 2018, 2019) are taken as reference for the use of drag or solar sails in passive deorbiting missions. Simulations show an intuitively larger number of collisions if a sail is attached to the spacecraft, compared to the simulations where no sail is attached, due to the larger impact area, yet the total number of debris fragments in the long term is smaller, as these collisions do not generate large fragments clouds. Using sails is thus advisable. Successful examples are provided by the technological demonstrations of drag sails, such as InflateSail, launched in 2017 (Underwood et al., 2019).

As for active debris removal missions, several concepts have been proposed for solar sails. TugSat is a CubeSat, equipped with a high-performance solar sail, to deorbit multiple satellites on the order of 1000 kg in Geostationary Orbit (GEO) (Kelly et al., 2018). The Space Waste Elimination around Earth by Photon Propulsion (SWEEP) project has a similar purpose: employing solar sailing technologies to "clean up space and preserve the near-Earth environment" [2]. Along with Delft University of Technology, the consortium includes universities, space agencies, and companies from around the world, and is supported by ESA's Space Debris Office.

2.2 Solar Sails

After Johannes Kepler, in 1608, first mentioned the idea that sails, just like ships, could have been adapted to navigate through the *"heavenly breezes"*, it took centuries for the first solar-sail spacecraft to be designed (McInnes, 1999). The uniqueness of solar sails lies in the absence of propellant on board: they could theoretically enable long-lasting missions, for as long as the spacecraft's lifetime. In this section, first, the principles underlying the functioning of a sailcraft are explained in Subsection 2.2.1, and typical solar sail designs are presented in Subsection 2.2.2. Then, flown solar sailing missions are listed in Subsection 2.2.3.

2.2.1 Fundamentals of Solar Sailing

As explained by McInnes (1999), solar sails are only limited by the lifetime of the sail film, as the thrust is generated from an ambient source: sunlight, by means of photons. Conventional

[2] https://www.tudelft.nl/lr/sweep (Accessed: 26 April 2024)

forms of propulsion, instead, from high to low-thrust, rely on the acceleration of a reaction mass to generate thrust and are limited by the finiteness of the propellant. Solar sails exploit Solar Radiation Pressure (SRP), through photons, both upon transfer of momentum and upon reflection (Fu et al., 2016).

One of the most important performance metrics for a solar sail is the characteristic acceleration, namely the acceleration experienced by the sail when the sail is perpendicular to the sunlight, at the Earth-Sun distance of 1 au (Wright, 1993). Typical values are below 0.1 $\frac{mm}{s^2}$, but future applications could reach values as high as 2.0 $\frac{mm}{s^2}$ or more (Ceriotti and Wilson, 2021).

Relying on the SRP, the thrust is constrained in its direction, since it cannot point toward the Sun; moreover, thrust direction and magnitude are coupled, since the magnitude depends on the relative orientation between the acceleration vector and the incoming sunlight (Ceriotti and Wilson, 2021). While other propulsion systems have an envelope that is a solid sphere (i.e., in principle the thrust can be steered in the three-dimensional space), the shape of the envelope of a solar sail spacecraft resembles that of a "bubble" (see Fig. 2.2, where the radial component, on the vertical axis, is aligned with sunlight, whereas the tangential component, on the horizontal axis, is perpendicular to sunlight). Thrust vector control can be achieved by modifying the attitude of the sail with respect to the incoming sunlight within the acceleration envelope.

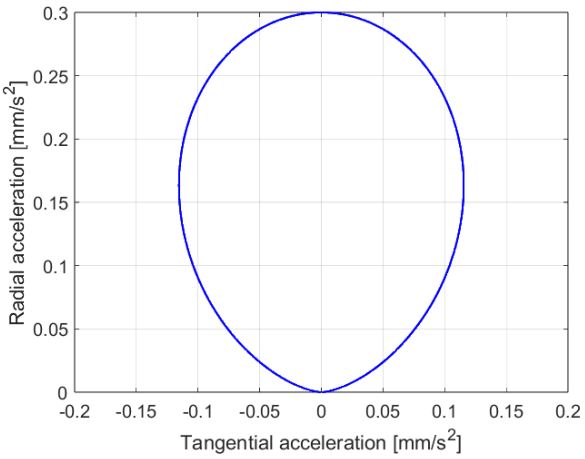

Figure 2.2: Sample bidimensional envelope of the acceleration of a solar sail with a characteristic acceleration of 0.3 $\frac{mm}{s^2}$, in a Sun-centered reference frame

2.2.2 Solar Sail Design

Since the momentum carried by an individual photon is very small, an extended surface is required, to intercept a large number of photons. Furthermore, to maximize the acceleration from the momentum exchange, solar sails must also be extremely lightweight (McInnes, 1999).

To achieve a large area and a small weight, three main sail configurations (presented in Fig. 2.3) have been developed: the square sail, the heliogyro, and the disc sail. To date, the square sail is the configuration with the highest technology readiness level, and is usually the preferred design for most mission applications (Jordaan, 2016).

Tensile strength of the sail is required so that, when fully deployed and under tension, the sail film does not fail and create tears. To avoid multiple reflections and the creation of hot spots, the sail film must also be free of wrinkles. Moreover, the sail front should be highly reflective. The substrate

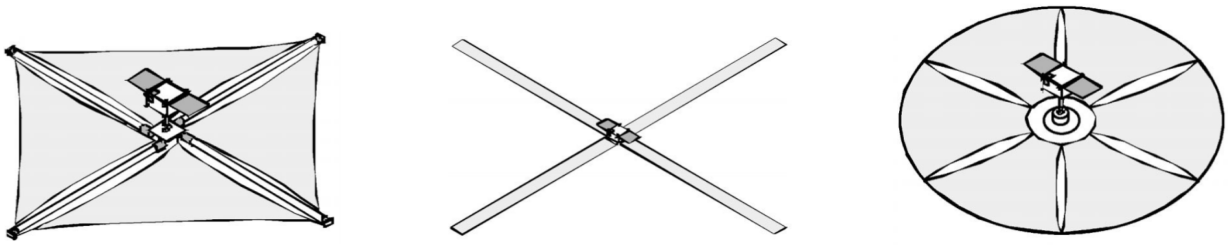

(a) Square sail **(b)** Heliogyro **(c)** Disc sail

Figure 2.3: Different solar sail configurations (Wie, 2004)

should allow handling, folding, packing, and deployment of the sail film. The back coating should be thermally emissive, to dissipate the absorbed radiation and keep the sail temperature within a given range. Thus, suitable materials must be chosen for the substrate, front, and back coating: a typical choice is represented by Kapton, aluminium, and chromium, respectively (McInnes, 1999).

2.2.3 Mission Heritage

Solar sailing is a flight-proven technology, and this subsection lists the flown solar sailing missions. Table 2.2 summarizes key performance metrics, namely the sail area, mass, area-to-mass ratio, and characteristic acceleration, for such missions.

The first real solar sailing mission, after two tests from Russia, between 1992 and 1999 (Garner, 2000), was the Interplanetary Kite-craft Accelerated by Radiation Of the Sun (IKAROS), by the Japanese Aerospace Exploration Agency, launched in May 2010 (Mori et al., 2014). After completing the sail deployment and passing by Venus in December 2010 with the assistance of SRP, IKAROS was left flying under an extended mission phase operation, and was declared a success (Tsuda et al., 2013).

NanoSail-D2 (a 3U CubeSat sailcraft developed by NASA) was launched in 2010, with deployment in 2011. This was the first successful in-orbit demonstration of a sail deployed by a CubeSat (Johnson et al., 2011).

The Planetary Society [3] devoted itself to the public-founded LightSail project, in 2005 (Jordaan, 2016). The LightSail-1 was a CubeSat-based satellite bus, launched in May 2015; however, the orbit was too low to fully demonstrate solar sailing (Ridenoure et al., 2015). LightSail-2 demonstrated the first controlled solar sailing in Earth's orbit using a CubeSat: it was launched in 2019 and deorbited in late 2022 (Mansell et al., 2023).

The Near Earth Asteroid (NEA) Scout, a CubeSat developed by NASA, was launched in November 2022, to study a NEA (Johnson et al., 2022), but it was declared lost after the project team was not able to communicate with the spacecraft.

NASA's Advanced Composite Solar Sail System (ACS3), a 12U CubeSat whose aim is to validate sail technologies for future larger-scale solar sails, was launched in April 2024. Its target injection orbit was a circular Sun-Synchronous Orbit (SSO), at 1000 km altitude, with a local time of the descending node window of 10:30-11:30 AM (Dono et al., 2024).

[3] https://www.planetary.org/ (Accessed: 2 May 2024)

Mission	Sail area [m^2]	Mass [kg]	Area-to-mass ratio [m^2/kg]	Characteristic acceleration [mm/s^2]
Ikaros (Sawada et al., 2011)	196	310	0.63226	0.005740903
NanoSail-D2 (Alhorn et al., 2011)	10	4	2.5	0.0227
LightSail-1 (Ridenoure et al., 2015)	32	5	6.4	0.058112
LightSail-2 (Spencer et al., 2021)	32	4.93	6.49087	0.05893712
NEA Scout (Johnson et al., 2022)	86	14	6.14286	0.055777143
ACS3 (Wilkie et al., 2021)	80	16	5	0.0454

Table 2.2: Overview of the flown solar sailing missions in terms of sail area, mass, and characteristic acceleration

2.3 Collisions in Space

The problem of an ever-increasing number of objects in space has caused a growing concern on the risk of collision between two (or more) space objects. If at least one of the objects involved is an operational spacecraft, with a capability of maneuvering, the need for performing a Collision Avoidance Maneuver (CAM) may arise. Expecting hundreds of satellites to be launched into orbit every year, it is also expected that the number of CAMs will increase significantly in the near future (Merz et al., 2017). In this section, first a widely used metric is introduced in Subsection 2.3.1: the Probability of Collision (PoC). Then, an overview of collision avoidance operations is provided in Subsection 2.3.2.

2.3.1 Probability of Collision

The PoC is a crucial metric in collision avoidance operations, since the threshold for a warning to be issued is set on its value: nowadays, a maneuver is triggered if the probability exceeds 10^{-4} (Flohrer et al., 2015). An event is considered escalated as soon as the mission control team is informed, something which typically happens if a threshold of 10^{-4} is exceeded three days before the event (Merz et al., 2017).

Li et al. (2022) summarized several bodies of work to produce a comprehensive study on the PoC computation, and this subsection is thus mainly based on their research. Tracking the state of an object in space, just like every measurement, is subject to uncertainty. Errors are described using a three-dimensional Probability Density Function (PDF). Collision probability is computed through the trivariate integration of the PDF of the uncertainty in the state of the two Resident Space Objects (RSOs) involved in the encounter. The integration domain is a control volume defined by the size of the two RSOs and their relative trajectory. The essence of most methods for computing the PoC is to perform the integration.

In general, collision probability can be divided into two categories: instantaneous and cumulative probability. The instantaneous probability is the collision probability at a single instant: the integration is performed over the volume of the two combined objects in the physical three-dimensional space, and the integral function is the joint PDF at the Time of Closest Approach (TCA), whose origin is

centered on one of the RSOs. The cumulative collision probability is instead the overall collision probability in time, obtained by integrating the instantaneous PoC in a period of interest.

2.3.2 Operational Collision Avoidance

Collision avoidance is a reality in mission operations today, for every spacecraft orbiting around Earth, with flight control teams trying, as far as possible, to combine orbit maintenance and collision avoidance maneuvers. For many years, collision avoidance had to rely on the information provided by TLEs, which give the orbital elements of a satellite at a certain epoch, along with an identifier of the satellite itself, but have limited accuracy, mainly due to the simplified dynamics employed (Gonzalo et al., 2021). Flohrer et al. (2008) derived uncertainties for several orbital classes based on TLE data. The process has evolved significantly since the mid-2010s, when Conjunction Summary Messages (CSMs) and Conjunction Data Messages (CDMs) became available to ESA (Flohrer et al., 2015). These messages contain, among other parameters, the covariance matrices of the objects involved in the potential encounter (NASA, 2021), and are issued by the Joint Space Operations Center to satellite operators. Today, each event is analyzed in an automated way, due to the large number of messages received (Merz et al., 2021).

Deciding whether a CAM should be executed is a crucial step, since executing a maneuver while it is not needed causes loss of services, effort, and valuable resources, whereas not executing a maneuver while it is needed is also obviously dangerous. Mission coordinators make such decisions based on the CDM and some of the key characteristics of the mission itself, executing a trade-off between "interruption of service and resource usage" versus "risk of collision" (Dural et al., 2021). If a maneuver takes place, the maneuver epoch is constrained by the TCA, by the last pass of the spacecraft above the ground station (for the uplink of the maneuver command), as well as by the spacecraft routine and maintenance operations (Dural et al., 2021).

Dural et al. (2021) presented the usual time frame for the decision-making process: CDMs are generally issued 72 hours (three days) before the TCA, with subsequent messages broadcast every six to eight hours. As the decision and planning of the maneuver can be a lengthy process, not much time is left for the execution of the maneuver itself, especially for short-notice collision warnings. Operators' reaction times to perform a maneuver can range from one to twelve hours, according to Spencer et al. (2024). It is also true that the notifications can be received several days in advance by satellite operators, as the screening volumes, for most missions, extend seven days into the future; only a few conjunctions receive the first CDM within one day to the TCA (Merz et al., 2017). In any case, a fast reaction is necessary: in Low Earth Orbit (LEO), decisions regarding maneuvers are usually made one day before conjunction (Aida, 2016), although earlier analyses are possible.

2.4 Collision Avoidance Maneuver Design for a Sail

Envisioning the usage of solar sails in Earth orbit requires dealing with collision avoidance maneuvers. Various strategies have been developed, by researchers, to design CAMs for conventional propulsion methods. Starting from the design of analytical optimal impulsive maneuvers (Bombardelli and Hernando-Ayuso, 2015), optimization of low-thrust CAMs has been performed, through indirect methods (Salemme et al., 2020; Palermo et al., 2021; De Vittori et al., 2022, 2023), successive convexification (Armellin, 2021; Pavanello et al., 2024), and heuristic algorithms (Kim et al., 2012; Morselli et al., 2014; Seong and Kim, 2015, 2016).

Up to date, however, the literature lacks studies whose aim is to design collision avoidance maneuvers for solar sails in an operational orbit around Earth. CAMs were only designed for sails in the deorbiting phase, by Gonzalo et al. (2018) and Colombo et al. (2018). This section is thus based on these works, unless stated otherwise.

From a conceptual point of view, there are two possibilities to reduce the collision probability, both limited by the control capabilities of the sail:

1. to change the sail orientation just before the closest approach to reduce the effective impact area;
2. to continuously control the sail orientation over time to reduce the collision probability or increase the miss distance.

The second option is the safest one, and has thus been investigated.

As impulsive CAMs, for spacecraft which employ conventional propulsion, tend to align the thrust with the velocity direction, simple structures are simulated, following an "on/off" control law, orienting the sail perpendicular ("on") or parallel ("off") to the atmospheric drag. Under this model, the area-to-mass ratio represents the control authority, namely the capability of modifying the nominal trajectory, and is used as the main parameter in the sensitivity analysis.

The maneuvering sail is assumed to be in the deorbiting phase, with the sail oriented perpendicular to the drag force. Then, for each tested maneuver time, the sail state is propagated backward from the TCA until the maneuver start epoch. Finally, the sail state is propagated forward, without drag and SRP, from the maneuver start epoch to the TCA, and the new miss distance is evaluated. CDMs shared by ESA are employed to model the uncertainties.

The miss distance can be increased greatly with a long enough maneuver time, depending on the area-to-mass ratio. For area-to-mass ratios of 0.5 and 2 $\frac{m^2}{kg}$, and a two-day warning, the PoC can be brought below a threshold of 10^{-6} in 9.6 and 2.4 hours, respectively. For a seven-hour warning, the sail with the smallest control authority is not able to bring the collision probability below the acceptable value of 10^{-4}. For this sail, the decision about performing the CAM would have to be taken with a previous CDM.

The outcome of the works is that, depending on the control authority of the sail and the geometry of the conjunction, there is a "dead zone", for which it is not possible to effectively reduce the risk of collision. Any decision about a CAM has to be taken before this "dead zone" is reached, limiting the operator's capability to wait for an updated, more accurate CDM to determine if the CAM is actually needed or not.

3
Research Objective

Based on the discussion developed in the previous chapter, a gap in the literature is identified in this chapter, so that the research objective and questions, upon which the work developed for this project is grounded, are laid out.

As space debris is causing growing and immediate concern among space agencies, and envisioning near-term Earth-bound applications for solar sails, it is necessary to investigate the collision avoidance capabilities of such propulsion methods. Collision avoidance is indeed a reality for every mission around Earth.

Up to date, research on collision avoidance methods has neglected solar sails: only the case of a deorbiting sail is considered, designing simple control laws to enhance or mitigate the effect of drag (the main perturbation in atmospheric deorbiting). Depending on the control authority (namely, the area-to-mass ratio) and the geometry of the encounter, there is a range of times for which it is not possible anymore to effectively reduce the risk of collision. For a two-day warning, the sails with area-to-mass ratios from 0.5 to 2 $\frac{m^2}{kg}$ can bring the PoC below the threshold in less than ten hours. On the other hand, for a seven-hour warning, the sail with an area-to-mass ratio of 0.5 $\frac{m^2}{kg}$ is unable to bring the PoC below the threshold.

Literature is lacking studies whose aim is to characterize collision avoidance maneuvers, for a plethora of scenarios, executed by a solar sail in an operational orbit around Earth. Specifically, maneuvers that require the minimum time, before the closest approach, should be targeted, to identify the "dead zone", after which the PoC cannot be reduced below a set threshold, for the different simulated scenarios. The required time shall then be compared with the current time frame of collision avoidance operations. Results are expected to depend on the parameters of the sail (affecting its control authority and its orbit at the closest approach), on the parameters of the debris (i.e., characteristics that allow a classification of the object), and on the conjunction parameters (which define the collision geometry).

Therefore, the research objective and the research questions stemming from the literature gap are introduced. This thesis project aspires to answer these questions.

Research Objective

Investigate the performance of a spacecraft, orbiting around Earth, which solely relies on solar sails to generate thrust, in the context of minimum-time collision avoidance maneuvers with respect to space debris, for different simulation scenarios.

Research Question 1

What is the minimum time required, before the closest approach, to maneuver and bring the probability of collision below a set threshold, for all simulated scenarios?

1.a What is the influence of the sail, debris, and conjunction parameters on the results?

1.b How do results fit within the current typical time frame of operational collision avoidance?

Research Question 2

What is the optimal control profile of the solution, in terms of the relative orientation between the acceleration provided by the solar sail and the direction of the sunlight throughout the maneuver, for all simulated scenarios?

2.a What is the influence of the sail, debris, and conjunction parameters on the results?

2.b Is the optimal control profile comparable to one of the locally optimal steering laws, to maximize the rate of change of a specific orbital element?

4
Methodology

The following chapter explains the algorithms implemented to answer the research questions presented in Chapter 3, along with the design choices and simplifying assumptions. The chapter structure comprises three main sections. First, in Section 4.1, the dynamical model is presented. Then, in Section 4.2, the building blocks which define a collision in space and its risk evaluation are introduced, from designing the conjunction to computing the PoC and retrieving the uncertainties. Subsequently, Section 4.3 outlines the steps taken to solve the optimization problem.

4.1 Dynamical Model

This section outlines the dynamical model. First, the employed reference frames, to conveniently express the sail and debris state, are presented in Subsection 4.1.1. Then, the choices behind the definition of the equations of motion are given in Subsection 4.1.2. Finally, the numerical integration setup is presented in Subsection 4.1.3. Table 4.1 summarizes the main choices for the definition of the dynamical environment and numerical integration setup.

4.1.1 Reference Frames

In this work, the following reference frames are employed. All reference frames are assumed to be right-handed.

1. **Earth-centered inertial reference frame**: The Earth-Centered Inertial (ECI) reference frame (subscript I) is a frame $I(\hat{\mathbf{x}}_I, \hat{\mathbf{y}}_I, \hat{\mathbf{z}}_I)$ centered at the Earth's Center of Mass (CoM), with $\hat{\mathbf{x}}_I$ pointing toward the first point of Aries Υ(the mean vernal equinox at January 1$^{\text{st}}$, 2000), $\hat{\mathbf{z}}_I$ pointing perpendicular to the mean equatorial plane at January 1$^{\text{st}}$, 2000 (toward the Northern hemisphere), and $\hat{\mathbf{y}}_I$ completing the right-handed reference frame.

2. **Radial-transverse-normal reference frame**: The Radial-Transverse-Normal (RTN) reference frames of the sailcraft (subscript O) $O(\hat{\mathbf{x}}_O, \hat{\mathbf{y}}_O, \hat{\mathbf{z}}_O)$ and of the debris (subscript Q) $Q(\hat{\mathbf{x}}_Q, \hat{\mathbf{y}}_Q, \hat{\mathbf{z}}_Q)$ are object-centered reference frames, with origin in the CoM of the respective object. For $K \in O, Q$, $\hat{\mathbf{x}}_K$ is parallel to the radial position vector, $\hat{\mathbf{z}}_K$ is in the direction of the orbital angular momentum vector (perpendicular to the orbital plane), and $\hat{\mathbf{y}}_K$ completes the right-handed reference frame. Basis vectors are obtained geometrically through the relations:

$$\begin{cases} \hat{\mathbf{x}}_K = \frac{\mathbf{r}_{I,k}}{||\mathbf{r}_{I,k}||} \\ \hat{\mathbf{z}}_K = \frac{\mathbf{r}_{I,k} \times \mathbf{v}_{I,k}}{||\mathbf{r}_{I,k} \times \mathbf{v}_{I,k}||} \\ \hat{\mathbf{y}}_K = \hat{\mathbf{z}}_K \times \hat{\mathbf{x}}_K \end{cases} \qquad \forall (K,k) \in \{(O, S/C), (Q, D)\} \tag{4.1}$$

where $\mathbf{r}_{I,k}$ and $\mathbf{v}_{I,k}$ are the inertial position and velocity vectors of the object, respectively. The cross product $\mathbf{r}_{I,k} \times \mathbf{v}_{I,k}$ defines the angular momentum vector of the object, $\mathbf{h}_{I,k}$. Subscripts S/C and D refer to the sailcraft and debris, respectively.

3. **Sunlight reference frame**: The sunlight reference frame (subscript S) is a sailcraft-centered frame $S(\hat{\mathbf{x}}_S, \hat{\mathbf{y}}_S, \hat{\mathbf{z}}_S)$ and is useful when dealing with the SRP acceleration. Its origin lies in the sailcraft's CoM. $\hat{\mathbf{x}}_S$ points in the Sun-to-sailcraft direction (coincident with the direction of sunlight), $\hat{\mathbf{y}}_S$ is expressed as $\hat{\mathbf{z}}_I \times \hat{\mathbf{x}}_S$, and $\hat{\mathbf{z}}_S$ completes a right-handed frame.

4. **Encounter reference frame**: The encounter reference frame (subscript M) is a sailcraft-centered frame $M(\hat{\mathbf{x}}_M, \hat{\mathbf{y}}_M, \hat{\mathbf{z}}_M)$ and is useful to describe conjunctions. Its origin lies in the sailcraft's CoM. $\hat{\mathbf{y}}_M$ points in the direction of the relative velocity, $\hat{\mathbf{z}}_M$ is parallel to the cross product between the relative position and relative velocity, and $\hat{\mathbf{x}}_M$ completes a right-handed frame.

$$\begin{cases} \hat{\mathbf{y}}_M = \frac{\mathbf{v}_{I,S/C} - \mathbf{v}_{I,D}}{||\mathbf{v}_{I,S/C} - \mathbf{v}_{I,D}||} \\ \hat{\mathbf{z}}_M = \frac{(\mathbf{r}_{I,S/C} - \mathbf{r}_{I,D}) \times (\mathbf{v}_{I,S/C} - \mathbf{v}_{I,D})}{||(\mathbf{r}_{I,S/C} - \mathbf{r}_{I,D}) \times (\mathbf{v}_{I,S/C} - \mathbf{v}_{I,D})||} \\ \hat{\mathbf{x}}_M = \hat{\mathbf{y}}_M \times \hat{\mathbf{z}}_M \end{cases} \tag{4.2}$$

For a generic reference frame $K(\hat{\mathbf{x}}_K, \hat{\mathbf{y}}_K, \hat{\mathbf{z}}_K)$, the expressions of the rotation matrix to the inertial frame, and vice versa, are:

$$R_{K \to I} = [\hat{\mathbf{x}}_K, \hat{\mathbf{y}}_K, \hat{\mathbf{z}}_K] \tag{4.3a}$$

$$R_{I \to K} = R_{K \to I}^T \tag{4.3b}$$

where the basis vectors are assumed to be column vectors.

4.1.2 Equations of Motion

The contributions of the orbital perturbations are generally negligible on the CAM design, due to the very small changes in the nominal trajectory introduced by the maneuver (Patera and Peterson, 2003). Therefore, most collision avoidance studies model Keplerian motion for the maneuvering satellite. In the context of studying CAM strategies in LEO, both for high and low-thrust engines, several pieces of literature tried to assess the effect of perturbations (Bombardelli et al., 2014; Hernando-Ayuso and Bombardelli, 2021; Armellin, 2021; De Vittori et al., 2022). The conclusion is unanimous: CAMs can be designed without considering orbital perturbations. However, for some specific conjunction geometries, the errors due to Earth's oblateness are not negligible. It is therefore decided to consider the J2 acceleration in the equations of motion for the sailcraft: as the first work to focus on collision avoidance for solar sails, the main source of perturbation is included. Moreover, the J2 effect is relevant for an SSO, the envisioned orbit for ACS3 (Dono et al., 2024).

Although CAM studies neglected the effect of atmospheric accelerations, such a perturbation could be predominant and non-negligible for solar sails, characterized by high area-to-mass ratios (Carzana et al., 2022a). One of the main concerns associated with employing a solar sail in LEO is indeed the minimum operating altitude at which the sailcraft can function, without the atmospheric drag becoming excessive (Mengali and Quarta, 2005). To stay conservative, the minimum operating altitude for the sailcraft under analysis is set to 1000 km, such that atmospheric effects can be ignored (United States Air Force, 1976). The atmosphere is thus not modeled.

For planetocentric applications of solar sailing, the radiation pressure coming from the planet plays a role (Klinkrad and Fritsche, 1999). Carzana et al. (2022b) stressed the importance of considering planetary radiation pressure in modeling solar sail trajectories around Earth, as it could get as high as 25% of the SRP at altitudes below 1000 km. However, its effect decreases with altitude and falls below 1% of the SRP at higher altitudes (approximately 20000 km). In the first iteration of this study, where only main perturbations are modeled, planetary radiation pressure is thus left out.

In the inertial frame, the equations of motion for the sail around Earth are:

$$\begin{cases} \dot{\mathbf{r}}_{I,S/C} = \mathbf{v}_{I,S/C} \\ \ddot{\mathbf{r}}_{I,S/C} = \mathbf{a}_{I,S/C,\mu_\oplus} + \mathbf{a}_{I,S/C,J2} + \mathbf{a}_{I,S/C,SRP}(\mathbf{u}(t)) \end{cases} \tag{4.4}$$

where $\mathbf{a}_{I,S/C}$ is the inertial acceleration vector of the sail, $\mathbf{u}$ is the control vector, t is the time variable, and the subscripts $\mu_\oplus$, $J2$, and SRP refer to the acceleration given by the Earth's central gravity, Earth's oblateness, and solar radiation pressure, respectively. The SRP acceleration depends on the control vector, defining the orientation of the sail with respect to the sunlight.

Ephemerides of the Sun are retrieved through the Spacecraft, Planet, Instrument, C-matrix, Events (SPICE) interface in the MATrix LABoratory (MATLAB) environment, offered by NASA's Navigation and Ancillary Information Facility (NAIF) [1]. Considering the expected short duration of CAMs, the position of the Sun is assumed to remain constant, equal to its value at the TCA. If results show a longer duration for the maneuvers, the assumption on the Sun position will be reconsidered.

The time variable is expressed in Universal Time Coordinated (UTC), as the seconds passed after January 1st, 2000, in line with the convention employed by SPICE.

Earth's Central Gravity

The acceleration from Earth's central gravity is (Wakker, 2015):

$$\mathbf{a}_{I,S/C,\mu_\oplus} = -\frac{\mu_\oplus}{r^3_{I,S/C}}\mathbf{r}_{I,S/C} \tag{4.5}$$

where $\mu_\oplus$ is the gravitational parameter of the Earth, the central body (see Page vi for the constant values), and $r_{I,S/C}$ is the norm of the planetocentric position vector $\mathbf{r}_{I,S/C}$.

Earth's Oblateness

The expression for the J2 acceleration, given by Earth's non-sphericity, is (Wakker, 2015):

$$\mathbf{a}_{I,S/C,J2} = -\frac{3}{2}\frac{\tilde{R}^2_\oplus}{r^5_{I,S/C}} J2\mu_\oplus[(r_{I,S/C,x}\hat{\mathbf{x}}_I + r_{I,S/C,y}\hat{\mathbf{y}}_I)(1 - 5\frac{r^2_{I,S/C,z}}{r^2_{I,S/C}}) + r_{I,S/C,z}(3 - 5\frac{r^2_{I,S/C,z}}{r^2_{I,S/C}})\hat{\mathbf{z}}_I] \tag{4.6}$$

where $\tilde{R}_\oplus$ is the mean equatorial radius of the Earth, $J2$ is the Earth's J2 gravitational field constant (see Page vi for the constant values), and, for a vector in a generic reference frame K, the subscripts x, y, z refer to the Cartesian coordinates of the vector along the basis vectors of the given frame $\hat{\mathbf{x}}_K$, $\hat{\mathbf{y}}_K$, $\hat{\mathbf{z}}_K$, respectively.

Solar Radiation Pressure

Kelly and Bevilacqua (2019) listed the main assumption underlying the ideal SRP model, employed in the project:

1. The square is a flat, rigid surface;
2. The solar sail is perfectly reflective;

[1] https://naif.jpl.nasa.gov/naif/ (Accessed: 15 May 2024)

3. The local solar radiation pressure is constant;
4. The SRP effect on the spacecraft bus is negligible;
5. The SRP acceleration is directed along the spacecraft's CoM;
6. The area-to-mass ratio of the system is constant.

The force generated by an ideal, perfectly reflective solar sail is orientated normally to the surface of the membrane of the sail. The normal direction, in the sunlight frame, is defined by two attitude angles:

$$\hat{\mathbf{n}}_S = cos(\alpha)\hat{\mathbf{x}}_S + sin(\alpha)sin(\delta)\hat{\mathbf{y}}_S + sin(\alpha)cos(\delta)\hat{\mathbf{z}}_S \tag{4.7}$$

where α is the cone angle, between the direction of sunlight and the sail normal direction, and δ is the clock angle, measured from $\hat{\mathbf{z}}_S$ to the projection of the sail normal onto the $(\hat{\mathbf{y}}_S, \hat{\mathbf{z}}_S)$ plane. The sail normal never has a component pointing toward the Sun's hemisphere, i.e., $\alpha \in [0, \frac{\pi}{2}]$ and $\delta \in [0, 2\pi]$. From the formulation of McInnes and Brown (1990), the ideal SRP acceleration in the ECI frame is:

$$\mathbf{a}_{I,S/C,SRP} = \nu a_c (\frac{\gamma_E}{\gamma_{S/C}})^2 cos^2(\alpha)\hat{\mathbf{n}}_I \tag{4.8}$$

where $\nu \in [0, 1]$ is the shadow factor (the fraction of sunlight reaching the sail), γ_E is the distance between the Earth and the Sun (1 au), $\gamma_{S/C}$ is the distance between the spacecraft and the Sun, $\hat{\mathbf{n}}_I$ is the unit vector normal to the sail in the inertial frame, and a_c is the characteristic acceleration.

As explained in Subsection 2.2.1, the characteristic acceleration a_c is defined as the acceleration produced at the Earth-Sun distance (of 1 au), when the sail is perpendicular to the sunlight direction (Wright, 1993):

$$a_c = 2\frac{W_E \eta}{\tilde{c}}\frac{A}{m} \tag{4.9}$$

where W_E is the mean solar flux (at all wavelengths) at 1 au, $\tilde{c}$ is the speed of light, η is a parameter describing the overall sail efficiency in terms of reflecting photons (usual values are between 0.85 and 0.9), m is the mass of the sailcraft, and A is the sail area. One can refer to Page vi for the constant values. Equation 4.9 also features a factor of 2 to account for the sail reflectivity, because reflected photons impart a reaction of equal magnitude to incident photons (McInnes, 1999).

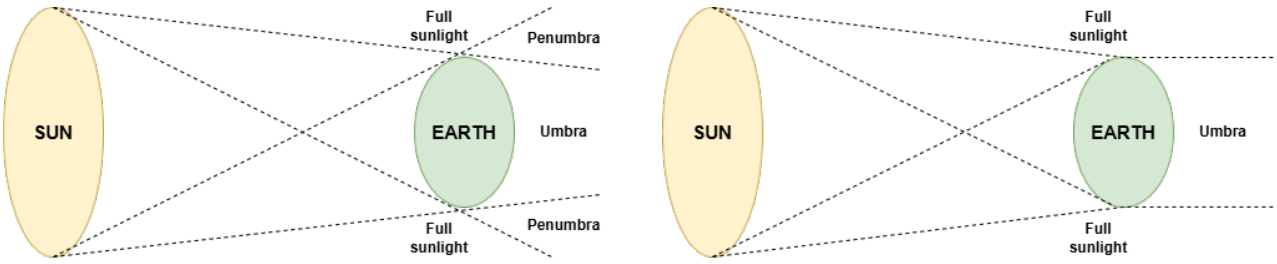

(a) Conical model **(b)** Cylindrical model

Figure 4.1: Shadow regions (not to scale) for the two eclipse models: sunlight, penumbra (if applicable), and umbra regions are shown (modified from Neta and Vallado (1998))

Equation 4.8 shows a dependence on the shadow factor ν: eclipses are indeed to be considered for Earth-centered applications, since the sail is unable to produce thrust when in shadow. The illuminating body is the Sun, of radius $\tilde{R}_\odot$ (see Page vi for the constant values), occulted by the Earth. Figure 4.1 shows the two main eclipse models: the conical model (in Fig. 4.1a), presented by Kelly

and Bevilacqua (2019) and the cylindrical model (in Fig. 4.1b), presented by Curtis (2020). The former is chosen for its more conservative approach: as a matter of fact, in the conical model (Fig. 4.1a), the area of the shadowed region is broader than in the cylindrical one (Fig. 4.1b). Penumbra is assumed as equal to umbra ($\nu = 0$), for conservativeness.

4.1.3 Numerical Integration

Cartesian position and velocity are selected for the state vector representation, since they offer an immediate physical understanding of the problem. This excludes all propagators (employing different state representations) except for the Cowell and Encke propagators. Cowell is chosen, as it is proved to be the most accurate, whereas Encke performs well in case of unperturbed motion (Pollock, 1994).

An analysis (whose details are given in the Appendix A) is performed among the integrators available in the MATLAB *ode* suite: the choice is to employ *ode89* (Verner, 2010) with relative and absolute tolerances of 10^{-12} and 10^{-8}, respectively. Tolerances are very tight as a high accuracy is required for collision avoidance studies, where the miss distances can be very small, and, indeed, *ode89* is employed to solve problems that require extreme accuracy (Shampine and Reichelt, 1997).

Parameter	Choice
Dynamical model	Earth's central gravity + Earth's J2 + SRP
Reference frame	ECI
Time frame	UTC
Ephemerides	SPICE
Atmospheric model	None
SRP acceleration model	Ideal
Eclipse model	Conical
Propagator	Cowell
Integrator	*ode89* ($tol_{rel} = 10^{-12}$, $tol_{abs} = 10^{-8}$)

Table 4.1: Overview of the main choices made for the dynamical environment and numerical integration setup

4.2 Collision Scenario Definition

In this section, the collision is characterized. First, the desired conjunction scenarios are defined in Subsection 4.2.1. Subsequently, the assumptions behind the PoC computation and the selected method are outlined in Subsection 4.2.2. Finally, the assumptions and the implementation of the uncertainty retrieval algorithm are given in Subsection 4.2.3.

4.2.1 Design Parameters

The purpose of this study is to assess the performance of solar sails in avoiding collisions: since collisions can happen in a plethora of different ways, key design parameters are identified in this subsection, to build the desired closest approach scenarios. First, the nominal TCA is defined. Then, three categories of parameters are identified: those characterizing the sail and its orbit around Earth, those characterizing the debris object, and those that define the conjunction (namely, the collision geometry). For an overview of all the design parameters and their values, see Table 4.6.

Time of the Closest Approach

Kelly and Bevilacqua (2021) highlighted that a spacecraft in the GEO region is subject to eclipsing events twice per year, when the Earth-Sun geometry lies about the vernal equinox line (i.e., during the vernal and autumnal equinoxes). At equinoxes, the time spent in shadow reaches its maximum value, also in LEO (Sumanth, 2019).

Therefore, the vernal and autumn equinoxes represent the "worst-case scenario" in terms of the percentage of the orbit spent in sunlight. For this reason, the simulations will be centered at the vernal equinox: specifically, the TCA is set to March 20th 2023, at 21:58:25.000 UTC [2].

Sail Parameters

The sail parameters are those that influence the control authority of the sail and its orbit at the TCA. As the first iteration of this study, the sailcraft is placed in a circular orbit (whose eccentricity is zero). The following variables are changed:

- **Area-to-mass ratio**: Three values are tried, namely 5 $\frac{m^2}{kg}$ (from ACS3, see Table 2.2), 4 $\frac{m^2}{kg}$, and 3 $\frac{m^2}{kg}$, where the latter two represent conservative scenarios. The characteristic acceleration is 0.0454 $\frac{mm}{s^2}$ (from ACS3, see Table 2.2), 0.0363 $\frac{mm}{s^2}$, and 0.0272 $\frac{mm}{s^2}$, respectively.
- **Altitude**: Altitudes in LEO (1000 km and 1800 km) and GEO (35786 km) are simulated, as these are the protected orbital regions by the Inter-Agency Space Debris Coordination Committee (IADC) (2021). SSOs are included in the study: since the target injection orbit for ACS3 (Dono et al., 2024) had an altitude of 1000 km, only SSOs at 1000 km, in the LEO region, are simulated.
- **Inclination**: As the whole spherical shell is protected in LEO, while only equatorial orbits are protected in GEO (IADC, 2021), orbits with an inclination of 0, 45, and 90 degrees are simulated in LEO, whereas only equatorial orbits (with a zero-degree inclination) are simulated in GEO. For SSOs, the inclination is fixed at 99.5 degrees, since the inclination is linked to the altitude for an SSO, to satisfy the Sun-synchronicity condition at 1000 km (Wakker, 2015).
- **Right ascension of the ascending node**: To study different orbit orientations with respect to the sunlight, several values of Right Ascension of the Ascending Node (RAAN) are included: 0, 45, and 90 degrees. Note that for equatorial orbits the RAAN is not defined and set at 0 degrees. A parameter to define the orientation of an SSO with respect to the Sun is the Local Time of the Ascending Node (LTAN), for which three values are selected, namely 6 ("dawn-dusk" orbit), 9, and 12 ("noon-midnight" orbit) AM. The LTAN in turn defines the RAAN of the orbit: at the vernal equinox, an LTAN of 6, 9, and 12 AM corresponds to a RAAN of 270, 315, and 360 degrees, respectively.
- **True anomaly at TCA**: Finally, the true anomaly of the sailcraft at the TCA is changed. This is done to place the sailcraft in four different illumination conditions, which are deemed the most significant to evaluate the sail performance:
    1. **full sunlight**: the projection of the sail position on the ecliptic plane lies along the Earth-Sun line, in the sunlight region;
    2. **sunlight/eclipse transition**: the sail lies at the beginning of the eclipse region;
    3. **full eclipse**: the projection of the sail position on the ecliptic plane lies along the Earth-Sun line, in the shadow region;

[2] https://www.astropixels.com/ephemeris/soleq2001.html (Accessed: 28 May 2024)

4. **eclipse/sunlight transition**: the sail lies at the end of the eclipse region.

If the orbit is such that the spacecraft is never in eclipse, four equally spaced values of true anomaly are used: 0, 90, 180, and 270 degrees.

Jointly changing the inclination and the RAAN is fundamental, in order to simulate the effect of different directions of the sunlight with respect to the orbital plane, which is known to drive solar-sail performance (Gamez Losada et al., 2024). For a generic sailcraft orbit, an aspect angle β is defined as the angle between the sunlight direction and the angular momentum vector, perpendicular to the orbital plane:

$$cos(\beta) = |\frac{\mathbf{h}_{I,S/C}}{||\mathbf{h}_{I,S/C}||} \cdot (R_{S\rightarrow I}\hat{\mathbf{x}}_S)| \tag{4.10}$$

The aspect angle is defined between 0 and 90 degrees (hence the reason for the absolute value operator in Eq. 4.10), so that orbits whose angular momentum vectors point in opposite directions, but whose orbital planes are reached by sunlight at the same angle, are treated similarly. Numerical values for the aspect angle are provided in Tables 4.2 and 4.3. Such values are computed for the position of the Sun at the equinox: it is important to use the aspect angle to generalize the results to different Earth-Sun configurations (namely, other times of the year).

	i = 0 deg	i = 45 deg	i = 90 deg
RAAN: 0 deg	90	90	90
RAAN: 45 deg	90	60	45
RAAN: 90 deg	90	45	0

Table 4.2: Aspect angle values, in degrees, for different combinations of inclination and right ascension of the ascending node, associated with the Sun's position at the vernal equinox

	i = 99.5 deg
LTAN: 6 AM	10
LTAN: 9 AM	45
LTAN: 12 AM	90

Table 4.3: Aspect angle values, in degrees, for the Sun-synchronous inclination (at an altitude of 1000 km), for different values of local time of the ascending node

Having defined the Keplerian elements of the sailcraft, its orbit at the TCA is fully defined: the nominal state vector of the sail, in terms of position and velocity, can be retrieved.

Debris Parameters

Debris parameters are the orbital eccentricity and the size, which allow a characterization of the objects, synthetically created for the simulations.

Klinkrad (2006) analyzed the catalog population, showing that the vast majority of the trackable objects reside on near-circular orbits (with an eccentricity below 0.01), and, in general, more than 80% of the objects have an eccentricity below 0.1. Larger eccentricities (close to 0.7) are mostly typical of objects in medium Earth orbit have larger eccentricities (close to 0.7) (ESA's Space Debris Office, 2024). For a study that focuses on spacecraft orbiting in LEO and GEO, it is thus safe to assume debris objects in circular orbits (with zero eccentricity).

As the mass of the object does not influence the PoC computation (and, thus, does not influence the collision avoidance maneuver design), the analyzed variable is the radial size of the object. As a matter of fact, in the definition of the orbital classes in the Assessment of Risk Event Statistics (ARES) tool, employed by ESA, the size of the objects plays a role, since smaller objects are subject to greater uncertainties (ESA's Space Debris Office, 2021)

The minimum detectable radii, by radar and optical measurement devices, are computed with the same procedure employed by ARES (ESA's Space Debris Office, 2021), and are given in Table 4.4. It is decided to test one value for the "small" catalog objects, as objects start being classified as risk-relevant from above 1 mm (Klinkrad, 2006), and two values for the "large" catalog objects: 0.125, 1, and 10 m in LEO, and 0.35, 1, and 10 m in GEO.

Altitude [km]	1000	1800	35786
Minimum radius [m]	0.04	0.12	0.35

Table 4.4: Minimum detectable radii for the three selected altitudes

Conjunction Parameters

The variables treated as conjunction parameters are those which directly influence the collision geometry, as the factors which allow the retrieval of the debris position and velocity vectors at the TCA, starting from the nominal state of the sail at the TCA.

1. **Debris position vector retrieval**

   The debris position vector is found, as shown in Fig. 4.2, by the sum between the sail position vector and the designed miss vector, defined in the inertial frame as:

   $$\mathbf{r}_{I,miss}(TCA) = \mathbf{r}_{I,D}(TCA) - \mathbf{r}_{I,S/C}(TCA) \tag{4.11}$$

   The miss vector can be characterized in terms of magnitude and direction. Three values of miss distance are used (1, 10, 100 meters), and the separation is directed along one of the three basis vectors of the RTN frame of the sailcraft $O(\hat{\mathbf{x}}_O, \hat{\mathbf{y}}_O, \hat{\mathbf{z}}_O)$.

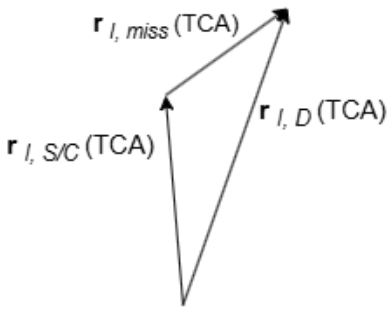

Figure 4.2: Debris position vector retrieval

2. **Debris velocity vector retrieval**

   Since both objects are on circular orbits, the collision happens in the plane perpendicular to the position vectors of the sailcraft and the debris at the TCA (Klinkrad, 2006). Only one rotation

angle ξ (the encounter angle), about the sail position vector, needs to be defined, as the angle between the sail and debris velocity directions at the TCA (see Fig. 4.3):

$$cos(\xi) = \frac{\mathbf{v}_{I,S/C}(TCA) \cdot \mathbf{v}_{I,D}(TCA)}{||\mathbf{v}_{I,S/C}(TCA)||\,||\mathbf{v}_{I,D}(TCA)||} \tag{4.12}$$

Seven values for the encounter angle are used: all the angles between 45 and 315 degrees, equally spaced by 45 degrees between each other. The fully collinear case ($\xi = 0$ deg) is not included. Only short-term encounters are modeled in the work, since they are the most common type of encounters, while long-term encounters are usually observed in satellite formation flying, spacecraft rendezvous, or docking (Chan, 2004). The short-term assumption of large relative velocities, of several kilometers per second (Li et al., 2022), would be invalidated by near-zero relative velocities in perfectly coplanar, circular orbits.

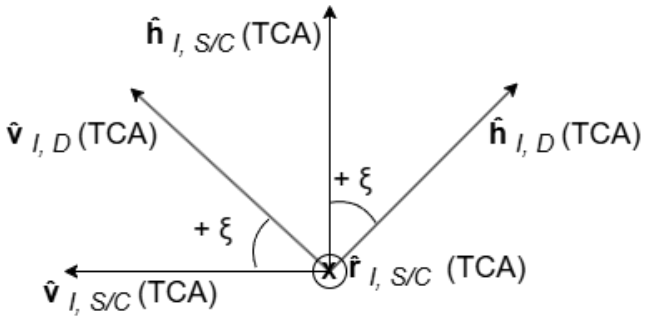

Figure 4.3: Debris velocity direction retrieval (the cross "x" indicates an inward vector)

The final step is the computation of the debris velocity magnitude. For circular debris orbits, this is straightforward, as the velocity magnitude equals the circular velocity (Wakker, 2015):

$$v_{I,D}(TCA) = \sqrt{\frac{\mu_{\oplus}}{r_{I,D}(TCA)}} \tag{4.13}$$

where $r_{I,D}$ and $v_{I,D}$ are the norms of the debris inertial position ($\mathbf{r}_{I,D}$) and velocity ($\mathbf{v}_{I,D}$) vectors, respectively.

An additional quantity can be included among those under analysis: the azimuth angle $\tilde{A}$. It is a parameter often employed to study collisions and, based on Klinkrad (2006), defined as:

$$\cos(\tilde{A}) = -\frac{\Delta\mathbf{v}(TCA) \cdot \mathbf{v}_{I,S/C}(TCA)}{||\Delta\mathbf{v}(TCA)||\,||\mathbf{v}_{I,S/C}(TCA)||} \tag{4.14}$$

where $\Delta\mathbf{v} = \mathbf{v}_{I,D} - \mathbf{v}_{I,S/C}$. The azimuth angle describes the angle between the relative velocity direction and the sailcraft velocity direction: Table 4.5 summarizes the relation between encounter and azimuth angles.

Encounter angle [deg]	45	90	135	180	225	270	315
Azimuth angle [deg]	67.5	45	22.5	0	22.5	45	67.5

Table 4.5: Relation between encounter and azimuth angles

Parameter	Values in LEO	Values in GEO	Values in SSO
TCA	Vernal equinox	Vernal equinox	Vernal equinox
Area-to-mass ratio (sail) [$\frac{m^2}{kg}$]	3, 4, 5	3, 4, 5	3, 4, 5
Eccentricity (sail) [-]	0	0	0
Altitude (sail) [km]	1000, 1800	35786	1000
Inclination (sail) [deg]	0, 45, 90	0	99.5
RAAN (sail) [deg] **LTAN (sail)** [h]	0, 45, 90	0	6 AM, 9 AM, 12 AM
True anomaly at TCA (sail)	1) Full sunlight 2) Sunlight/eclipse 3) Full eclipse 4) Eclipse/sunlight or [0, 90, 180, 270] deg	1) Full sunlight 2) Sunlight/eclipse 3) Full eclipse 4) Eclipse/sunlight or [0, 90, 180, 270] deg	1) Full sunlight 2) Sunlight/eclipse 3) Full eclipse 4) Eclipse/sunlight or [0, 90, 180, 270] deg
Eccentricity (debris) [-]	0	0	0
Size (debris) [m]	0.125, 1, 10	0.35, 1, 10	0.125, 1, 10
Miss distance [m]	1, 10, 100	1, 10, 100	1, 10, 100
Miss direction	$\hat{\mathbf{x}}_O, \hat{\mathbf{y}}_O, \hat{\mathbf{z}}_O$	$\hat{\mathbf{x}}_O, \hat{\mathbf{y}}_O, \hat{\mathbf{z}}_O$	$\hat{\mathbf{x}}_O, \hat{\mathbf{y}}_O, \hat{\mathbf{z}}_O$
Encounter angle [deg]	45, 90, 135, 180, 225, 270, 315	45, 90, 135, 180, 225, 270, 315	45, 90, 135, 180, 225, 270, 315
Azimuth angle [deg]	0, 22.5, 45, 67.5	0, 22.5, 45, 67.5	0, 22.5, 45, 67.5

Table 4.6: Overview of the design parameters and their values in LEO, GEO, and SSO

4.2.2 Probability Computation

There are several ways to compute the collision probability, and most methods differ according to the way the integration of the PDF of the errors is carried out (as explained in Subsection 2.3.1). In this subsection, the assumptions underlying the PoC computation are presented, leading to the choice of a suitable method, among existing ones.

Cumulative collision probability methods are the only considered ones, as most applications require the overall collision probability for two RSOs during a period of interest (Li et al., 2022). Moreover, as explained in the previous subsection, only short-term encounters are dealt with. In short-term encounters, the relative velocity is constant during the encounter, the relative motion is fast enough for the relative trajectory to be considered a straight line, and the swept volume is an infinitely long cylinder (Li et al., 2022). This allows the three-dimensional integration to be reduced to a two-dimensional integration, by integrating along the relative velocity direction: the domain is the encounter plane, orthogonal to the relative velocity.

Alfano and Oltrogge (2018) collected additional assumptions, upon which collision probability methods are grounded. First, the positional errors are assumed to be zero-mean, Gaussian, and uncorrelated. Second, the objects are modeled as spheres: thus, both for the sail and the debris, the radius of the circumscribing sphere will be considered. This is a conservative approach, as the whole area will be projected on the encounter plane, without considering the attitude of the two objects. The sail is assumed to be a square sail, which is the most common configuration (as explained in Subsection 2.2.2).

Among existing methods, it is chosen to employ Foster's method (Foster, 1992), which maps the object location in the encounter plane through polar coordinates. The main reason behind the choice of the

Foster method is its availability to the public via the Collision Avoidance Risk Assessment (CARA) tool, assembled by NASA [3]. As a matter of fact, NASA aims at enhancing space safety as a shared responsibility, by means of making publicly available the source code and documentation for key conjunction risk assessment algorithms. The Foster method has already been used to assess on-orbit risk for NASA missions, and its accuracy has been proved by Alfano (2007).

In Foster's method, the conjunction is studied in the encounter reference frame $M(\hat{\mathbf{x}}_M, \hat{\mathbf{y}}_M, \hat{\mathbf{z}}_M)$. The integration domain is represented by the encounter plane $(\hat{\mathbf{x}}_M, \hat{\mathbf{z}}_M)$, perpendicular to the relative velocity. The algorithm takes as input, for both objects, the state at the TCA, the covariance at the TCA, and the size.

4.2.3 Uncertainty Retrieval

As mentioned in the previous subsection, covariance information of the two objects is required in the collision probability computation: satellite operators receive CDMs, which contain the covariance matrices for the objects involved in the encounter (see Subsection 2.3.2). This subsection starts by listing four main sets of assumptions, made to model the uncertainties. Then, the procedures followed by ARES are briefly presented. Finally, the uncertainty retrieval algorithm implemented for this work is introduced.

The first set of assumptions is derived from the fact that short-term encounters are considered. Therefore, no uncertainty on the velocity is considered, and the position uncertainty is assumed constant during the encounter, equal to the value at the TCA (Li et al., 2022).

The second set of assumptions comes from the probability computation: the position errors are assumed uncorrelated, and the objects are modeled as spheres (Alfano and Oltrogge, 2018). Therefore, uncertainties are treated separately, and the total covariance is the sum of the covariances of the two RSOs.

Additionally, the sailcraft is assumed to have an on-board Global Positioning System (GPS) receiver, as is the case for the ACS3 mission (Dono et al., 2024): if real-time on-board autonomous orbit determination is performed, tracking errors would be mitigated (Capuano et al., 2017). For this reason, the uncertainty of the sailcraft position is neglected: the same approach was taken by Alfriend et al. (1999). Thus, only the uncertainty concerning the debris position needs to be modeled. The total covariance is:

$$C = C_{S/C} + C_D \xrightarrow[C_{S/C} << C_D]{} C \approx C_D \tag{4.15}$$

where $C_{S/C}$ and C_D are the position covariance matrices of the sailcraft and debris object, respectively.

A fourth assumption regards the shape of the covariance matrix, which is modeled as diagonal and aligned with the basis vectors of RTN frame of the debris $Q(\hat{\mathbf{x}}_Q, \hat{\mathbf{y}}_Q, \hat{\mathbf{z}}_Q)$ (Alfriend et al., 1999; Pavanello et al., 2024). The covariance is thus expressed as:

$$C = \begin{bmatrix} \sigma^2_{\hat{\mathbf{x}}_Q} & 0 & 0 \\ 0 & \sigma^2_{\hat{\mathbf{y}}_Q} & 0 \\ 0 & 0 & \sigma^2_{\hat{\mathbf{z}}_Q} \end{bmatrix} \tag{4.16}$$

[3] https://github.com/nasa/CARA_Analysis_Tools/blob/master/DistributedMatlab/ProbabilityOfCollision/Pc2D_Foster.m (Accessed: 10 June 2024)

where σ is the position standard deviation, and the subscripts $\hat{\mathbf{x}}_Q$, $\hat{\mathbf{y}}_Q$, $\hat{\mathbf{z}}_Q$ refer to the uncertainties along the basis vectors of the RTN frame of the debris $\hat{\mathbf{x}}_Q$,$\hat{\mathbf{y}}_Q$,$\hat{\mathbf{z}}_Q$, respectively.

In ARES, CDMs are used to derive the uncertainties at the TCA. The overall CDM population is divided by orbital class (based on the size, perigee altitude, inclination, and eccentricity of the object), and regression is performed to obtain (ESA's Space Debris Office, 2021):

$$\begin{cases} \sigma_{\hat{\mathbf{x}}_Q} = \tau_{1,\hat{\mathbf{x}}_Q} \cdot 10^{\tau_{2,\hat{\mathbf{x}}_Q} \cdot \zeta} \\ \sigma_{\hat{\mathbf{y}}_Q} = \tau_{1,\hat{\mathbf{y}}_Q} \cdot (\tau_{3,\hat{\mathbf{y}}_Q} + \zeta)^{\tau_{2,\hat{\mathbf{y}}_Q}} \\ \sigma_{\hat{\mathbf{z}}_Q} = \tau_{1,\hat{\mathbf{z}}_Q} \cdot 10^{\tau_{2,\hat{\mathbf{z}}_Q} \cdot \zeta} \end{cases} \tag{4.17}$$

where τ denotes a generic regression coefficient and ζ is the time interval before the closest approach.

The full CDM database is not publicly accessible, and thus a full regression cannot be performed. Some pieces of research made use of CDMs provided by ESA, but only under non-disclosure agreements (Gonzalo et al., 2018). A solution does exist: in 2019, ESA shared a batch of 162,634 CDMs, collected between 2015 and 2019, corresponding to 13,154 unique events, for a collision avoidance challenge [4]. The dataset has been used in literature to model realistic conjunctions: examples can be found in the works by Armellin (2021) and De Vittori et al. (2022, 2023). Armellin filtered the CDM dataset (so that the PoC or miss distance values were within some threshold values) to identify significant test cases, and made the "filtered" dataset publicly available [5]; however, all data points are used in this work, as all CDMs contribute, in ARES, to the fitting process for the covariance generation (ESA's Space Debris Office, 2021).

Shared information is not enough to cover all the orbital classes: for some classes, there are no items at all, whereas, for some others, the number of items is not large enough to be statistically significant (usually, at least 100 elements are required). Data points are clustered in three specific orbital regions:

1. near-circular orbits ($e < 0.1$), for inclinations above 60 degrees and perigee altitudes below 800 km;
2. near-circular orbits ($e < 0.1$), for inclinations above 60 degrees and perigee altitudes between 800 km and 25000 km;
3. eccentric orbits ($e > 0.1$), for inclinations below 30 degrees and perigee altitudes below 800 km

The solution to the data unavailability comes from ARES. Before the advent of CDMs, if CSMs did not provide a reliable source of data, TLEs were used to fill the gaps, operating by analogy: for those classes where both TLE and CSM information was available, it was possible to obtain a mapping factor between them and apply that factor to classes where there were only TLEs but no CSMs (Braun et al., 2019; ESA's Space Debris Office, 2021). Indeed, even if no CDMs are available, it is advisable to translate TLE information to CDM information (Sánchez-Ortiz et al., 2015).

A covariance-mapping algorithm is therefore implemented to retrieve the uncertainties: Fig. 4.4 presents it. The idea is to compute a mapping factor between CDMs and TLEs for a reference orbital class, and apply the mapping to all other classes, where CDMs are unavailable. As this work deals with circular orbits, there are two available classes in the employed dataset. The class for eccentricity below 0.1, perigee altitude between 800 and 25000 km, and inclination above 60 degrees is used as the reference class, while the orbital class with the same characteristics, but perigee altitude below

[4] https://kelvins.esa.int/collision-avoidance-challenge/ (Accessed: 17 June 2024)
[5] https://github.com/arma1978/conjunction (Accessed: 24 June 2024)

800 km, is used for verification purposes (see Appendix D.2). The choice is based on the fact that this work focuses on altitudes higher than 800 km (see Table 4.6).

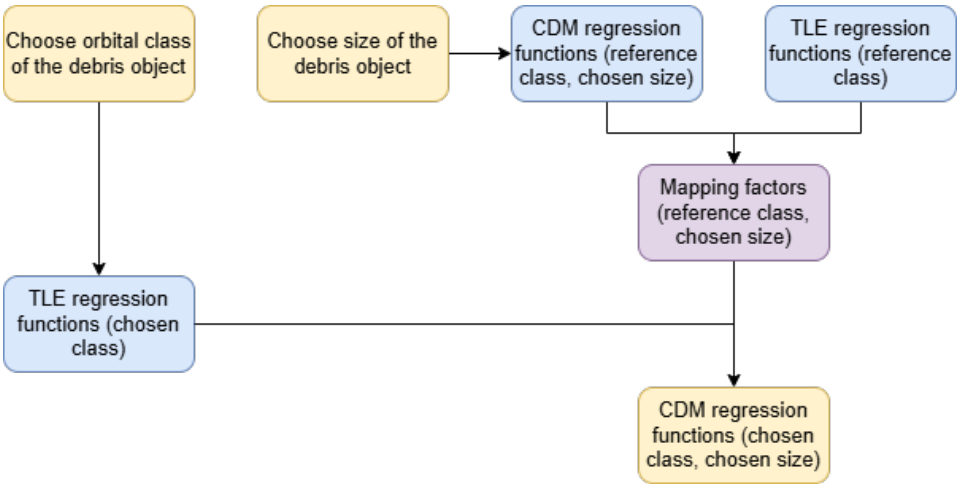

Figure 4.4: Flow of the covariance-mapping algorithm

The inputs of the mapping algorithm are the orbital class and the size of the debris object. Ranges for the parameters (see Table 4.7) are chosen based on Flohrer et al. (2008), for the perigee altitude, eccentricity, and inclination, and on ARES (ESA's Space Debris Office, 2021), for the debris size. The outputs are time-dependent regression functions, along the three directions of the RTN frame of the debris, to compute the position uncertainties at the desired time before the closest approach. The time horizon goes from zero to seven days before the closest approach: the reason is that the employed CDM dataset spans such an interval, and that usually also orbit determination operations cover weekly periods (Merz et al., 2017).

Parameter	Symbol	Ranges
Size [m^2]	s	$s \leq 1$ $s \geq 1$
Perigee altitude [km]	$\tilde{h}_p$	$\tilde{h}_p \leq 800$ $800 < \tilde{h}_p \leq 25000$ $\tilde{h}_p > 25000$
Eccentricity [-]	e	$e \leq 0.1$ $e > 0.1$
Inclination [deg]	i	$i \leq 30$ $30 < i \leq 60$ $i > 60$

Table 4.7: Overview of the ranges of the parameters in the uncertainty retrieval algorithm

First, for the chosen orbital class of the debris object, TLE uncertainties are generated: the initial diagonal covariance matrix, in the RTN frame of the debris, is built from the uncertainties computed by Flohrer et al. (2008), as was done in ARES (ESA's Space Debris Office, 2021), assuming the computed values to apply to different time epochs without changes. If data is unavailable for the orbital class of interest (this happens, for instance, for high-inclination orbits in GEO), information is taken from the orbital class with the same eccentricity and altitude, and the closest value of inclination (ESA's Space Debris Office, 2021).

The TLE-based covariance needs to be propagated in time, until the TCA (Schiff, 2006):

$$C(t_f) = \Phi(t_f, t_0) \cdot C(t_0) \cdot \Phi(t_f, t_0)^T \quad \text{with} \quad t_f = TCA \tag{4.18}$$

where $\Phi(t_f, t_0)$ is the State Transition Matrix (STM), and the subscripts 0 and f refer to the initial and final conditions, respectively. The STM can indeed link a perturbation in the state at an initial epoch to the change at a final epoch (Rugh, 1996). In Eq. 4.18, the STM evolution in time is required. Hence, the STM is integrated, starting from $\Phi(t_0, t_0) = \tilde{I}$, where $\tilde{I}$ is the identity matrix. The following relation is exploited (Rugh, 1996):

$$\frac{\partial \Phi(t, t_0)}{\partial t} = G_Q(t)\Phi(t, t_0) \tag{4.19}$$

where G is the dynamics matrix, expressed in the RTN frame of the debris Q, since the matrices in Eq. 4.18 are expressed in such a frame. It links the change in the derivative of the state to the state itself. To model the uncertainties affecting the sail state, computing the dynamics matrix would require the uncertainties of drag and SRP coefficients, as pointed out by Gonzalo et al. (2019). However, since only the debris position uncertainty needs to be dealt with, the dynamical model can be reduced to Earth's point mass gravity and J2 effect. As a first approximation, indeed, SRP does not play a role, assuming the debris objects to have a small area-to-mass ratio: default, average values are in the ballpark of 0.007 $\frac{m^2}{kg}$ (Song-hua and Jing-shi, 2023). Considering only Earth's central gravity and J2 perturbation, the dynamics matrix G is thus analytically available (see Appendix B).

A Monte Carlo campaign [6] is carried out, propagating the covariance for different values of time before the closest approach (t_0) through Eq. 4.18. For all samples, uncertainties are extracted from the final covariance (at the TCA). Once a TLE-based uncertainty dataset is built for the chosen orbital class, a linear regression is carried out, to obtain the coefficients in Eqs. 4.17, yielding the uncertainties as a function of the time to the closest approach. However, Eqs. 4.17 show a non-linear relation between the uncertainty and the time. To perform the regression, logarithmic transformations are employed, obtaining:

$$\begin{cases} log_{10}(\sigma_{\hat{\mathbf{x}}_Q}) = log_{10}(\tau_{1,\hat{\mathbf{x}}_Q}) + \tau_{2,\hat{\mathbf{x}}_Q} \cdot \zeta \\ log_{10}(\sigma_{\hat{\mathbf{y}}_Q}) = log_{10}(\tau_{1,\hat{\mathbf{y}}_Q}) + \tau_{2,\hat{\mathbf{y}}_Q} \cdot log_{10}(\tau_{3,\hat{\mathbf{y}}_Q} + \zeta) \\ log_{10}(\sigma_{\hat{\mathbf{z}}_Q}) = log_{10}(\tau_{1,\hat{\mathbf{z}}_Q}) + \tau_{2,\hat{\mathbf{z}}_Q} \cdot \zeta \end{cases} \tag{4.20}$$

Once the relation is linear, coefficients are retrieved by means of the linear regression tools in MATLAB. For the uncertainty along $\hat{\mathbf{y}}_Q$, an extra step is taken, due to the presence of the coefficient $\tau_{3,\hat{\mathbf{y}}_Q}$: the process is performed iteratively, changing the value of $\tau_{3,\hat{\mathbf{y}}_Q}$ until the best fitting is found. This yields an expression for $\sigma_{\hat{\mathbf{x}}_Q}, \sigma_{\hat{\mathbf{y}}_Q}, \sigma_{\hat{\mathbf{z}}_Q}$ as a function of the time interval before the closest approach.

For the reference orbital class, regression functions from the TLEs are obtained through the same procedure explained in the previous paragraphs: after the Monte Carlo campaign and the uncertainty propagation, the coefficients in Eqs. 4.20 are obtained by linear regression. For the CDM data, instead, the linear regression to obtain the coefficients in Eqs. 4.20 is performed without the need to propagate the uncertainties: CDMs already provide the covariance at the TCA. For the CDM regression algorithm, data is taken, from the reference orbital class, for the chosen debris size. A distinction can indeed be made between "small" and "large" objects. This distinction does not apply to TLEs, as neither the uncertainty nor the STM depends on the size of the object.

[6] 1000 items are sampled through a Sobol distribution

Therefore, the mapping factors are computed: these are the ratios between the regression functions obtained from the CDMs and the TLEs, for the reference orbital class and chosen debris size, for the uncertainties along the three directions ($\hat{\mathbf{x}}_Q, \hat{\mathbf{y}}_Q, \hat{\mathbf{z}}_Q$). The mapping can be applied to the chosen orbital class and size of the object, to retrieve time-dependent regression functions, whose input is the time interval before the TCA, as:

$$q^{(\psi)}_{CDM,\,class\,2,\,dim}(\zeta) = \underbrace{\frac{q^{(\psi)}_{CDM,\,class\,1,\,dim}(\zeta)}{q^{(\psi)}_{TLE,\,class\,1}(\zeta)}}_{\text{Mapping factor for direction } \psi} \cdot q^{(\psi)}_{TLE,\,class\,2}(\zeta) \qquad \forall \psi \in \{\hat{\mathbf{x}}_Q, \hat{\mathbf{y}}_Q, \hat{\mathbf{z}}_Q\} \tag{4.21}$$

where the mapped regression function, from the CDM data, q_{CDM}, for the chosen orbital class ($class\,2$) and debris size (dim), in direction ψ, is obtained from the corresponding function, from the TLE data, q_{TLE}, scaled by the mapping factor derived for the reference orbital class ($class\,1$) and the same debris size (dim), in direction ψ.

4.3 Optimization Setup

Once the collision scenario is defined, the Optimal Control Problem (OCP) is formulated and solved. Subsection 4.3.1 explains the choice of a fixed-time-horizon optimization, leading, in Subsection 4.3.2, to the definition of the OCP to be solved. Subsection 4.3.3 presents the selected solver and optimization settings. Finally, two optimization cases are outlined in Subsection 4.3.4: the "ideal" and the "real" cases, whose difference is explained later in this section.

4.3.1 Fixed-Time-Horizon Optimization

The objective of the optimization is to find the minimum maneuver time Δt for which the sailcraft can perform a CAM, bringing the PoC below the threshold. The initial time is free, whereas the final time (TCA) is fixed (see Table 4.6). Maneuvers are designed to end at the TCA as the minimum required warning time, before the TCA, is sought (see Chapter 3). The cost function J would be:

$$J = t_f - t_0 = TCA - t_0 \tag{4.22}$$

However, solving the OCP with free initial time adds complexity to the problem, because:

1. the initial state can only be found by back-propagating the sail state at the TCA;
2. the covariance at the TCA needs to be retrieved based on the chosen maneuver start epoch;
3. a constraint needs to be set on the PoC value at the TCA.

Moreover, solving an OCP with free initial or final time is challenging in terms of numerical convergence (Bojkov and Luus, 1996). To reduce complexity, the OCP is therefore formulated as a fixed-time-horizon optimization problem, and the optimal maneuver time will be found through iterations, following the approach by Longuski et al. (2014). The expression "major iterations" will be used, in the remainder of the section, to refer to the iterations to identify the optimal maneuver time, varying the maneuver start epoch t_{MAN}.

4.3.2 Optimal Control Problem

Solving the optimal control problem consists of finding a state history $\boldsymbol{\rho}(t)$ and a control history $\mathbf{u}(t)$, with the time t being the independent variable, to minimize a cost function J, while constraints are satisfied (Longuski et al., 2014). In this subsection, after defining the objective function, the variables, and the constraints, the structure of the optimal control problem is provided, resulting in Problems 1 and 2.

Objective Function

As mentioned in the previous Subsection, the objective of the optimization is not the maneuver time, which is iteratively changed between subsequent optimizations ("major iterations"). Most CAM studies focused on minimizing fuel consumption, while respecting a constraint on collision probability (Salemme et al., 2020; De Vittori et al., 2023; Pavanello et al., 2024), but this is not the primary concern for solar sailing applications due to the absence of propellant. Alternatives do exist, with objective functions which are decoupled from fuel consumption (Morselli et al., 2014; Gonzalo et al., 2018; Colombo et al., 2018; Armellin, 2021). There are two main options:

- **Maximum separation**: the objective is to maximize the distance between the sail and the debris object at the TCA. The formulation of the cost function J is straightforward:

$$J = \frac{1}{\Delta\mathbf{r}^T(TCA) \cdot \Delta\mathbf{r}(TCA)} \tag{4.23}$$

  where $\Delta\mathbf{r} = \mathbf{r}_{I,S/C} - \mathbf{r}_{I,D}$. The distance is placed in the denominator since optimization algorithms are typically designed to operate by minimizing the cost function.

- **Minimum collision probability**: the objective is to minimize the collision probability at the TCA. To do so, the Squared Mahalanobis Distance (SMD) is introduced. Based on Pavanello et al. (2024), the SMD is defined as:

$$d = \Delta\mathbf{r}^T_{(\hat{\mathbf{x}}_M,\hat{\mathbf{z}}_M)}(TCA)C^{-1}_{(\hat{\mathbf{x}}_M,\hat{\mathbf{z}}_M)}(TCA)\Delta\mathbf{r}_{(\hat{\mathbf{x}}_M,\hat{\mathbf{z}}_M)}(TCA) \tag{4.24}$$

  where the subscript $(\hat{\mathbf{x}}_M, \hat{\mathbf{z}}_M)$ refers to the projection on the encounter plane (see Subsection 4.2.2). The SMD is particularly useful, as it can be analytically linked to the collision probability through an approximated expression (Alfriend et al., 1999):

$$PoC \approx \frac{(\tilde{R}_{circ,S/C} + \tilde{R}_{circ,D})^2}{2\sqrt{det(C_{(\hat{\mathbf{x}}_M,\hat{\mathbf{z}}_M)}(TCA))}} e^{-\frac{d}{2}} \tag{4.25}$$

  where $\tilde{R}_{circ,S/C}$ and $\tilde{R}_{circ,D}$ represent the radii of the circumscribing spheres of the sailcraft and the debris object, respectively. Thus, the objective function can be formulated as the maximization of the SMD, since it is inversely proportional to the PoC (see Eq. 4.25), as:

$$J = \frac{1}{\Delta\mathbf{r}^T_{(\hat{\mathbf{x}}_M,\hat{\mathbf{z}}_M)}(TCA)C^{-1}_{(\hat{\mathbf{x}}_M,\hat{\mathbf{z}}_M)}(TCA)\Delta\mathbf{r}_{(\hat{\mathbf{x}}_M,\hat{\mathbf{z}}_M)}(TCA)} \tag{4.26}$$

  Equation 4.26 reflects the fact that the probability can be reduced if the distance is increased along a direction whose associated uncertainty is smaller.

Time, State, and Control Variables

In the optimization problem, the independent variable is the time t, expressed in UTC. The OCP is posed through a one-phase approach, with fixed initial and final times. The time horizon is:

$$t \in [t_{0,iter}, t_f] = [t_{0,iter}, TCA] \tag{4.27}$$

where the subscript $iter$ refers to a generic "major iteration". The initial time varies as "major iterations" proceed, while the final time (TCA) is fixed at the vernal equinox (see Table 4.6).

The state history consists of the state vector (in Cartesian position and velocity) of the sailcraft, in the ECI reference frame:

$$\boldsymbol{\rho}(t) \in \mathbb{R}^6 \quad \text{with} \quad \boldsymbol{\rho}(t) = [r_{I,S/C,x}(t), r_{I,S/C,y}(t), r_{I,S/C,z}(t), v_{I,S/C,x}(t), v_{I,S/C,y}(t), v_{I,S/C,z}(t)]^T \tag{4.28}$$

In the literature, the control profile of the sail is often expressed in terms of control angles (Song and Gong, 2019a; Carzana et al., 2022a). However, the interpolation of two angular functions could lead to numerical difficulties, associated with the fact that the angles need to be "wrapped" between boundary values (such as $[0, 2\pi]$). Following the approach by Heiligers et al. (2014), the control history is represented by the Cartesian components of the normal vector to the solar sail (equivalent to the unit solar sail acceleration vector), expressed in the sunlight frame S:

$$\mathbf{u}(t) \equiv \mathbf{n}_S(t) \in \mathbb{R}^3 \quad \text{with} \quad \mathbf{n}_S(t) = [n_{S,x}(t), n_{S,y}(t), n_{S,z}(t)]^T \tag{4.29}$$

Constraints

Constraints on the state are expressed as

$$\dot{\boldsymbol{\rho}}(t) = \mathbf{f}(t, \boldsymbol{\rho}(t), R_{S\to I} \cdot \mathbf{u}(t)) \tag{4.30a}$$

$$\boldsymbol{\rho}(t_0) = \boldsymbol{\rho}_0 \tag{4.30b}$$

$$\boldsymbol{\rho}_{\min} \leq \boldsymbol{\rho}(t) \leq \boldsymbol{\rho}_{\max} \tag{4.30c}$$

Equation 4.30a enforces the dynamical constraint, with the dynamics function given in Eqs. 4.4. Since the dynamics are expressed in the ECI reference frame, the control vector is rotated from the sunlight to the inertial frame through the matrix $R_{S\to I}$. Equation 4.30b constrains the initial state of the sail, which can be obtained by back-propagation, starting from the nominal state of the sail at the TCA. Equation 4.30c sets the bounds on the state: it is sufficient to choose arbitrarily small and large values for the lower and upper bounds, respectively. The bounds are defined as multiples of the norms of the initial position and velocity: specifically, factors of -10 and 10 are employed for the lower and upper bounds, respectively. This choice is justified by the fact that neither position nor velocity is expected to increase or decrease by an order of magnitude during the short CAM.

Constraints on the control are given as

$$[0, -1, -1]^T \leq \mathbf{u}(t) \leq [1, 1, 1]^T \tag{4.31a}$$

$$||\mathbf{u}(t)|| = 1 \tag{4.31b}$$

Equation 4.31a imposes the bounds: the first component, in the sunlight frame, is kept between 0 and 1, as the acceleration vector cannot be directed toward the Sun (McInnes, 1999). Equation 4.31b

enforces a path constraint, to ensure that the norm of the control vector is unity throughout the trajectory.

Structure of the Optimal Control Problem

The definition of two objective functions (Eqs. 4.23 and 4.26) leads to two optimal control problems, subject to the same constraints (Eqs. 4.30-4.31). The OCP for the maximum separation is reported in Problem 1 and the OCP for the minimum collision probability is reported in Problem 2.

Optimal Control Problem 1

$$\begin{aligned}
&\underset{\mathbf{u}(t)}{\textbf{minimize}} && J = \frac{1}{\Delta\mathbf{r}^T(TCA)\cdot\Delta\mathbf{r}(TCA)} && \text{(Maximum separation)}\\
&\text{subject to} && \dot{\boldsymbol{\rho}}(t) = \mathbf{f}(t,\boldsymbol{\rho}(t), R_{S\to I}\cdot\mathbf{u}(t)) && \text{(State dynamics)}\\
& && \boldsymbol{\rho}(t_0) = \boldsymbol{\rho}_0 && \text{(State initial condition)}\\
& && \boldsymbol{\rho}_{\min} \le \boldsymbol{\rho}(t) \le \boldsymbol{\rho}_{\max} && \text{(State bounds)}\\
& && [0,-1,-1]^T \le \mathbf{u}(t) \le [1,1,1]^T && \text{(Control bounds)}\\
& && ||\mathbf{u}(t)|| = 1 && \text{(Control path constraints)}
\end{aligned}$$

Optimal Control Problem 2

$$\begin{aligned}
&\underset{\mathbf{u}(t)}{\textbf{minimize}} && J = \frac{1}{\Delta\mathbf{r}^T_{(\hat{\mathbf{x}}_M,\hat{\mathbf{z}}_M)}(TCA)C^{-1}_{(\hat{\mathbf{x}}_M,\hat{\mathbf{z}}_M)}(TCA)\Delta\mathbf{r}_{(\hat{\mathbf{x}}_M,\hat{\mathbf{z}}_M)}(TCA)} && \text{(Minimum PoC)}\\
&\text{subject to} && \dot{\boldsymbol{\rho}}(t) = \mathbf{f}(t,\boldsymbol{\rho}(t), R_{S\to I}\cdot\mathbf{u}(t)) && \text{(State dynamics)}\\
& && \boldsymbol{\rho}(t_0) = \boldsymbol{\rho}_0 && \text{(State initial condition)}\\
& && \boldsymbol{\rho}_{\min} \le \boldsymbol{\rho}(t) \le \boldsymbol{\rho}_{\max} && \text{(State bounds)}\\
& && [0,-1,-1]^T \le \mathbf{u}(t) \le [1,1,1]^T && \text{(Control bounds)}\\
& && ||\mathbf{u}(t)|| = 1 && \text{(Control path constraints)}
\end{aligned}$$

4.3.3 Optimal Control Solver

This subsection characterizes the selected optimal control solver, and presents the parameters to set it up, in order to solve the OCPs 1 and 2.

Solver Selection

Direct optimization methods are robust, flexible, and easy to initialize, variables have a clear physical meaning, and complex control or state constraints are easily handled (Morante et al., 2021). They are therefore chosen for solving the Problems 1 and 2. An additional reason lies in the fact that CAMs are usually very short: short CAM duration implies few orbital revolutions, at most. Therefore, there is little danger that the solver becomes ill-conditioned, as is often the case for many-revolution problems

(Topputo and Zhang, 2014).

Among existing tools, the second version of the General Purpose OPtimal control Software (GPOPS-II) is selected. It is a general purpose solver, gradient-based, widely used for solving low-thrust, and solar sailing, OCPs (Morante et al., 2021). GPOPS-II uses a pseudospectral method: the collocation method is a Gaussian quadrature implicit integration method with collocation applied at Legendre-Gauss-Radau (LGR) points (Patterson and Rao, 2014). It is widely recognized as a state-of-the-art optimization software: indeed, it is usually used as a verification tool for novel algorithms (Mall, 2018), including solar sailing trajectory optimization (Song and Gong, 2019a, 2019b).

The key feature of direct collocation methods is the discretization of the state and control at a set of appropriately chosen points in the time interval of interest; the continuous-time OCP is then transcribed to a finite-dimensional Non-Linear Programming (NLP) problem (Topputo and Zhang, 2014), which can be solved by the Interior Point Optimizer (IPOPT) (Wächter and Biegler, 2006), compatible with GPOPS-II. Once the NLP problem is solved, it is untranscribed to a discrete approximation of the OCP, and the error in the discrete approximation for the current mesh is estimated. The solution error is estimated using a relative difference between the state estimate and the integral of the dynamics at a modified set of LGR points. The solution is outputted if the error is below the user-set tolerance; otherwise, the mesh is refined and the problem is solved again, until convergence (Patterson and Rao, 2014).

One of the greatest advantages of GPOPS-II lies in its mesh refinement algorithm, as it employs hybrid methods (the *hp-methods* and *ph-methods*), either increasing the number of collocation points in a mesh interval or refining the mesh (Patterson and Rao, 2014). This allows taking advantage of the exponential convergence of a global Gaussian quadrature method in regions where the solution is smooth, and introducing mesh points only near potential discontinuities (Babuška, 1988). Moreover, the sparsity of the problem structure is exploited by GPOPS-II in searching for the optimal solution (Patterson and Rao, 2012). However, as Mall warned (2018), GPOPS-II can be parallelized only to a certain extent, and, for several OCPs, there is the risk of obtaining jittery control solutions, unrealistic to implement in real-world applications.

For a more accurate explanation of the GPOPS-II algorithm, one can refer to Patterson and Rao (2014), whereas, in the user manual by Patterson and Rao (2016), a complete guide to using the MATLAB interface is given, along with several examples of solved OCPs.

Problem scaling

Topputo and Zhang (2014) pointed out that, to ensure convergence of direct collocation methods, the NLP problem should be properly scaled, so that the variables are close to unity; then, based on the scaling parameters, also the constraints and the objective are scaled by GPOPS-II (Patterson and Rao, 2014).

GPOPS-II offers some predefined automatic scaling method, starting from the variable bounds, the initial guess, the solution on the current mesh, or a hybrid between the aforementioned options (Paterson and Rao, 2016). However, if automatic scaling was used, the optimizer failed to find an optimal solution to the Problems 1 and 2.

Custom scaling quantities are therefore employed, based on the low-thrust transfer optimization presented by Longuski et al. (2014). The position and velocity are scaled by the norm of the initial position and velocity from the initial guess, respectively. As the CAM is expected to make the spacecraft only slightly deviate from its nominal orbit, there is a guarantee that the position

and velocity values will not deviate much from unity. Scaling parameters for the time and the acceleration are obtained by dimensional analysis, whereas no scaling is applied to the controls, since the components of the vector normal to the sail are already bounded between -1 and +1 (see Eq. 4.31a).

Settings of the Optimal Control Solver

The settings of the optimizer are given in Table 4.8: values for such parameters are found by trial and error (evaluating the solution in terms of computational speed as well as of smoothness of the state and control profiles), and by comparison with solved optimization problems, provided as sample material by Patterson and Rao (2016). One can refer to the GPOPS-II user manual (Patterson and Rao, 2016) for a detailed explanation of all settings. The choices for the settings are justified by numerically integrating the optimal control solution and verifying that the difference between the resulting state history and the state from GPOPS-II falls below a set threshold (see Appendix D.3). IPOPT is the chosen NLP solver, since it is already available and ready for use once the GPOPS-II license is purchased.

To reduce the computational time due to a large number of scenarios to be simulated, the algorithm is written to be run in parallel, using the MATLAB Parallel Computing Toolbox.

GPOPS-II setting	Choice
Mesh method	'hp-LiuRao-Legendre'
Mesh tolerance	10^{-4}
Mesh maximum iterations	10
Mesh maximum collocation points	15
Mesh minimum collocation points	6
Mesh collocation points per interval	6
Number of mesh intervals	20
IPOPT linear solver	'ma57'
IPOPT tolerance	10^{-4}
IPOPT maximum iterations	2000
Derivative supplier	Forward differences
Derivative level	'second'
Derivative dependencies	'sparseNaN'
Method	'Differentiation'

Table 4.8: Overview of the GPOPS-II settings to solve the optimal control problem

4.3.4 "Ideal" and "Real" Optimization Case

Two optimization cases are defined: the "ideal" and "real" cases. They differ in terms of probability requirement for the maneuver, covariance retrieval epoch, optimal control problem to be solved, guess generation algorithm for the first "major iteration", and scheme employed to perform the "major iterations". Table 4.9 summarizes the key differences between the two optimization cases. In this subsection, for both cases, firstly the choices regarding the target PoC of the maneuver and the covariance retrieval epoch are explained, and then the OCP to be solved is selected. Subsequently, the algorithms to generate the initial guess and perform the "major iterations" are outlined. Finally, the whole algorithmic flow is presented.

Probability Requirement and Covariance Retrieval Epoch

Since the target PoC for the maneuver and the covariance retrieval epoch are key factors in defining a collision avoidance maneuver, these parameters are varied in the two optimization cases. The target PoC for the maneuver corresponds to the final value of collision probability, at the TCA, after the CAM is executed. The covariance retrieval epoch is varied to simulate different scenarios when CDMs are issued. As explained in Subsection 2.3.2, in real-life applications, there is always a time gap between the reception of a CDM and the actual execution of a maneuver. CDMs are often issued several days before the TCA, allowing the possibility of an earlier maneuver decision. Additionally, satellite operators require some reaction and decision time before commanding a maneuver.

In the "ideal" optimization case, the target of the maneuver, in terms of PoC, is set at 10^{-4}, which is the usual value employed by satellite operators to assess the risk posed by a conjunction (Flohrer et al., 2015; Braun et al., 2016; Merz et al., 2021; Spencer et al., 2024). Gonzalo et al. (2018) investigated the effect of the lead time, which is the interval between the maneuver start epoch and the TCA. To do so, they assumed the covariance matrix, for the debris object, is obtained exactly at the maneuver start epoch. The same approach is employed in the "ideal" case: this case is referred to as "ideal" since the decision time, between CDM reception and maneuver command, is brought to zero.

In the "real" case, the target, in terms of PoC, is set at 10^{-6}, since most CAMs target this value to rule out the collision risk (Flohrer et al., 2015): it is known that satellite operators often wish to bring the collision probability below the threshold value (10^{-4}) by one or more orders of magnitudes (Spencer et al., 2024). This case is referred to as "real" due to its more realistic modeling of covariance retrieval. To simulate the interval between CDM reception and maneuver execution, a buffer time is introduced. Its value is set at 24 hours: since one day is regarded as the upper threshold to decide whether to maneuver or not (Aida, 2016), it is assumed that no uncertainty can be retrieved later than one day before the TCA. The "real" case is created to address the following question: which is the upper bound for the minimum maneuver time, from the "ideal" optimization case, if more realistic position uncertainties and probability requirements are accounted for?

Both algorithms require the optimization to be performed if the value of the collision probability three days before the TCA exceeds the threshold of 10^{-4} (for the reason of this choice, see Subsection 2.3.1).

Optimization Purpose

In Subsection 4.3.2, two feasible options for the objective function were provided, leading to the definition of OCPs 1 and 2. Running the algorithm on a number of test cases highlighted that the optimization whose objective is to find the maximum separation is much faster than that whose objective is the minimum collision probability. Solving OCP 1 (minimizing Eq. 4.23) can be up to twenty times faster than solving OCP 2 (minimizing Eq. 4.26). It is thus important to select the best approach, in terms of the objective function, for each optimization case, considering limited resources concerning computational power and time.

In the "ideal" case, the objective is the minimum PoC: the minimum required time will be such that the minimum collision probability, for the specific maneuver time, cannot be brought below the threshold. To save computational time, however, the optimization is carried out by initially optimizing for maximum separation (solving OCP 1). Afterwards, the PoC value at the TCA is checked:

- If the PoC for the maximum separation is below the threshold, it is guaranteed that also the PoC for the minimum-collision-probability optimization will fall below the threshold, by definition

of minimum value of a function (Stewart, 2008).

- If the PoC for the maximum separation is above the threshold, there is no theoretical guarantee that also the PoC for the minimum-collision-probability optimization will be above the threshold. The optimization needs to be performed again, by solving OCP 2, searching for the minimum PoC.

This completes one "major iteration" in the "ideal" case.

In the "real" case, at every "major iteration", the optimization is only carried out for maximum distance (solving OCP 1), for simplicity. Since the "real" optimization case aims to determine an upper bound for the maneuver time, a slightly shorter actual maneuver time is not considered problematic.

Guess Generation

As GPOPS-II makes use of a direct collocation method, an initial guess of the solution needs to be provided (Patterson and Rao, 2016). The initial guess should reflect a control law that can bring the probability of collision below a certain threshold.

As an initial guess, one could think of maximizing the rate of change of a Keplerian element in a given time interval. Expressions for the so-called locally optimal steering laws, to maximize the rate of change of each of the orbital elements, are available in the literature (McInnes, 1999; Macdonald and McInnes, 2005a, 2005b), and are provided in Appendix C. Since circular orbits are considered, the argument of perigee is neglected, and only the control laws to maximize the rate of change of the Semi-Major Axis (SMA), eccentricity, inclination, and RAAN are investigated.

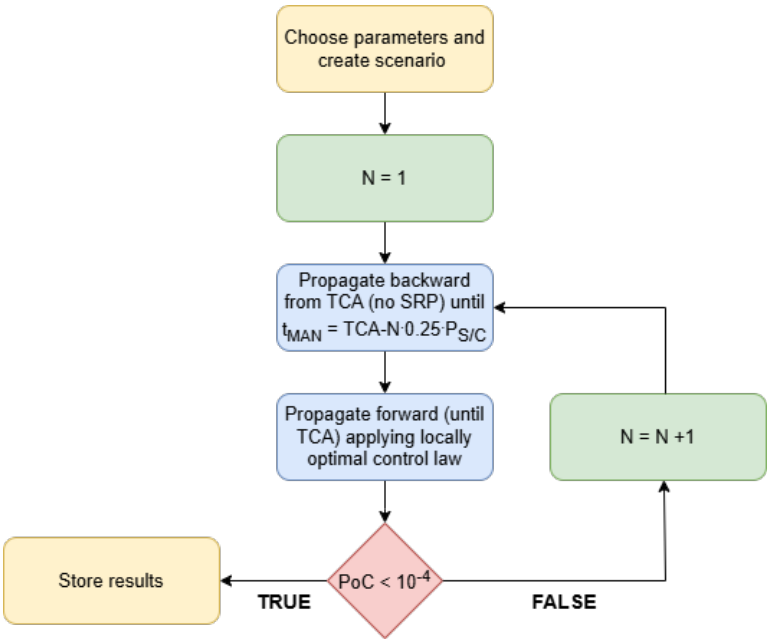

Figure 4.5: Flow of the initial guess generation algorithm, for a given locally optimal control law

The most suitable control law, to decrease the PoC, is sought. To do so, for a given control law and parameter combinations, the algorithm presented in Fig. 4.5 is employed. First, the closest approach is built, for the set of sail, debris, and conjunction parameters under analysis. Then, the sailcraft is propagated backward by a quarter of its orbital period ($P_{S/C}$), starting from the nominal state at

the TCA. A quarter of the orbital period is chosen by comparison with the duration of optimized low-thrust CAMs (Gonzalo et al., 2018; Colombo et al., 2018; Palermo et al., 2021; Armellin, 2021; De Vittori et al., 2022). In the backward propagation, the sail is oriented so that no SRP acceleration is produced. This is followed by a forward propagation, starting from the newly obtained state, until the TCA, with the sailcraft following the locally optimal control law. The PoC is recomputed for the final state at the TCA, applying the uncertainty retrieval algorithm (as explained in Subsection 4.2.3), assuming the covariance is retrieved at the maneuver start epoch. If the PoC falls below the threshold, the algorithm stops; otherwise, the algorithm increases the propagation time, by a quarter of the orbital period, until convergence.

Once results are generated for all the control laws under analysis, the locally optimal steering law that yields the shortest maneuver time is selected. If the maneuver times coincide, as the time is discretized (it is likely for more control laws to require the same number of steps to satisfy the condition), the control law which brings the probability to the lowest value is chosen. In case of the same probability value, the preferred control law will be the one that augments the miss distance the most. The selected control law is regarded as the "best" locally optimal steering law.

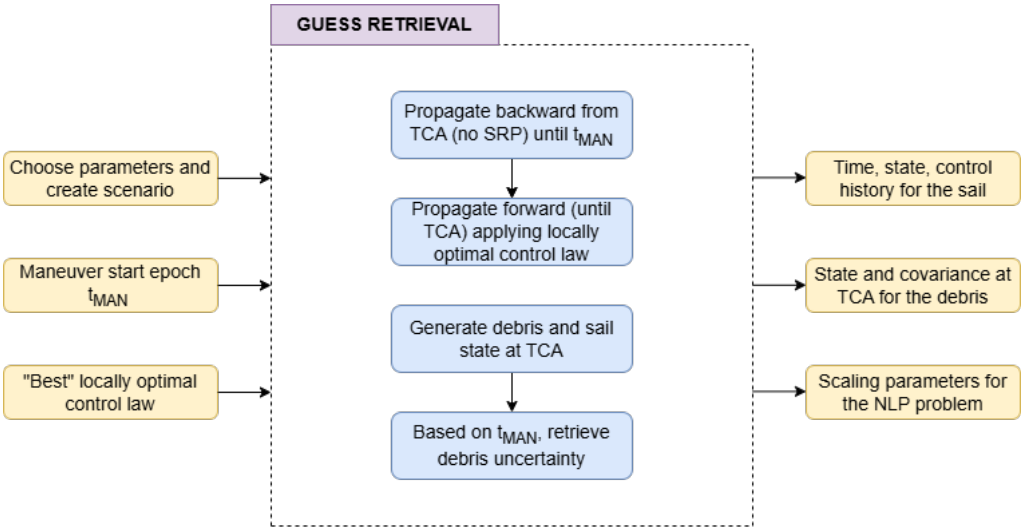

Figure 4.6: Inputs, processes, and outputs of the guess retrieval algorithm

For both optimization cases, at every "major iteration", the inputs and outputs of the guess generation algorithm are presented in Fig. 4.6. Guesses need to be generated for every "major iteration", since the result from the previous "major iteration" cannot be used as an initial guess, as the time horizon changes throughout "major iterations". For a given maneuver start epoch, the "best" locally optimal steering law is employed to generate the initial guess, in terms of time, state, and control history. From the initial position and velocity of the guess, the scaling parameters are fed to the optimizer. Moreover, based on the given maneuver start epoch, the debris position covariance matrix is generated (see Subsection 4.2.3). For the "ideal" case, the guess for the maneuver time, for the first "major iteration", is found by means of the algorithm in Fig. 4.5. For the "real" case, instead, the maneuver time, for the first "major iteration", is initialized through the solution of the "ideal" optimization, which is carried out in advance.

Time-Iterating Scheme

As explained in Subsection 4.3.1, subsequent fixed-time-horizon optimizations are performed, to iteratively find the optimal maneuver time.

In the "ideal" optimization case, the chosen scheme to carry out the "major iterations" is the bisection method, due to its proven efficiency. The scheme stops when two subsequent values of maneuver time differ by less than one minute. The longer the maneuver time of the first "major iteration", the more bisections are needed to reach the desired accuracy: the maximum number of "major iterations" is thus a function of the initial guess for the maneuver time, $N_{max} = g(\Delta t_{guess})$.

A generic "major iteration" of the bisection method can be summarized as follows:

- The input maneuver start epochs are t_1 and t_2, with $t_1 < t_2$ (for the first "major iteration", t_1 is the initial epoch of the guess and t_2 is represented by the closest approach epoch);
- The optimization is performed with $t_3 = \frac{t_1+t_2}{2}$ ($t_1 < t_3 < t_2$);
- The PoC is computed after optimizing for t_3, and the next "major iteration" is setup:
  - If the PoC is below the threshold, the maneuver time is decreased, and the lower bound of the maneuver start epoch is increased: the inputs for the next "major iteration" are t_3 and t_2 (with $t_3 < t_2$);
  - If the PoC is above the threshold, the maneuver time is increased, and the upper bound of the maneuver start epoch is decreased: the inputs for the next "major iteration" are t_1 and t_3 (with $t_1 < t_3$).

Decreasing the maneuver time means increasing the lower bound of the maneuver start epoch, moving it forward, toward the TCA (by definition, the maneuver start epoch precedes the TCA).

In the "real" case, "major iterations" proceed augmenting the maneuver time by 50%, for simplicity, and the limit for the maneuver start epoch is set at 24 hours before the TCA (Aida, 2016).

Algorithmic Flow

The algorithmic flows for the "ideal" and "real" optimization cases, are presented in Figs. 4.7 and 4.8, respectively. Table 4.9 summarizes the key differences between the two cases.

Parameter	"Ideal" case	"Real" case
Target PoC	10^{-4}	10^{-6}
Covariance retrieval epoch (simulated CDM issue)	t_{MAN}	t_{MAN} - 24 hours
Objective	Minimum PoC	Maximum separation
Initial guess for first "major iteration"	"Best" locally optimal steering law	Optimal solution of the "ideal" case
Time-iterating scheme	Bisection method	Maneuver time is augmented by 50%

Table 4.9: Overview of the differences between the "ideal" and "real" optimization cases

In the "ideal" optimization (Fig. 4.7), for a generic set of sail, debris, and conjunction parameters, the "best" locally optimal control law and the initial guess for the maneuver time from the algorithm in Fig. 4.5 (Δt_{guess}) are retrieved. The debris covariance matrix is obtained through the algorithm explained in Subsection 4.2.3, at the maneuver start epoch. Then, the optimization is carried out, first solving OCP 1, and, if the PoC value is above the threshold, also solving OCP 2. Once the optimal

solution is outputted, the PoC is recomputed, and, based on its value, the maneuver time is either decreased or increased, through bisection. This completes one "major iteration" of the optimization process. For every new "major iteration", the initial guess is computed (see Fig. 4.6), applying the "best" locally optimal steering law for the updated maneuver start epoch. Once "major iterations" stop, when the desired one-minute accuracy is reached, results are outputted.

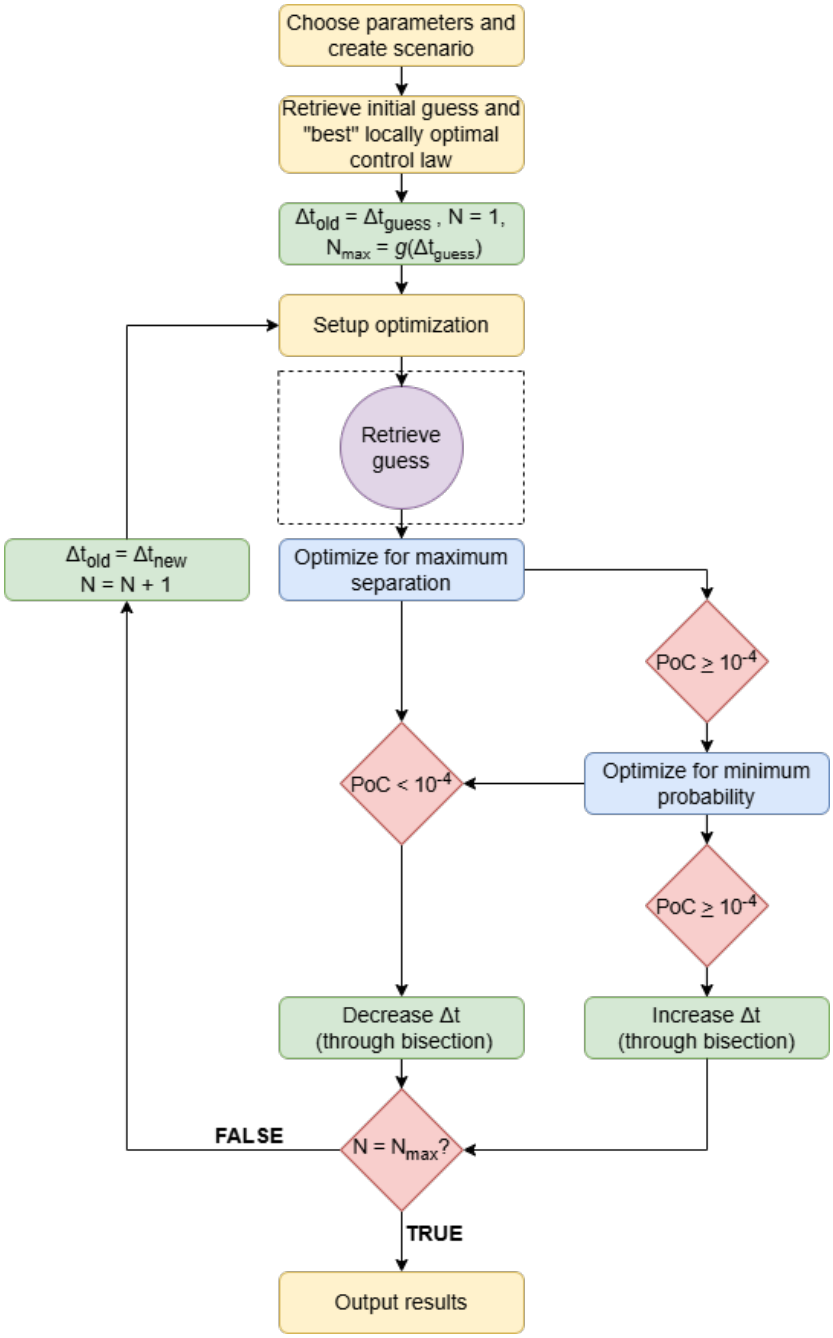

Figure 4.7: Flow of the "ideal" optimization algorithm

In the "real" optimization (Fig. 4.8), for a generic set of sail, debris, and conjunction parameters, the "best" locally optimal control law is retrieved, along with the optimal solution for the "ideal" case: the guess for the maneuver time, to be fed to the optimizer for the first "major iteration", comes indeed from the "ideal" optimization case (Δt_{opt}). The debris covariance matrix is obtained through the

algorithm explained in Subsection 4.2.3, one day before the maneuver start epoch. The optimization is carried out, solving OCP 1. Once the optimal solution is outputted, the PoC is computed, and, based on its value, either the algorithm is stopped (if the probability complies with the requirement) or the maneuver time is increased by 50%, until convergence. For every new "major iteration", the initial guess is computed (see Fig. 4.6), by applying the "best" locally optimal steering law for the updated maneuver start epoch.

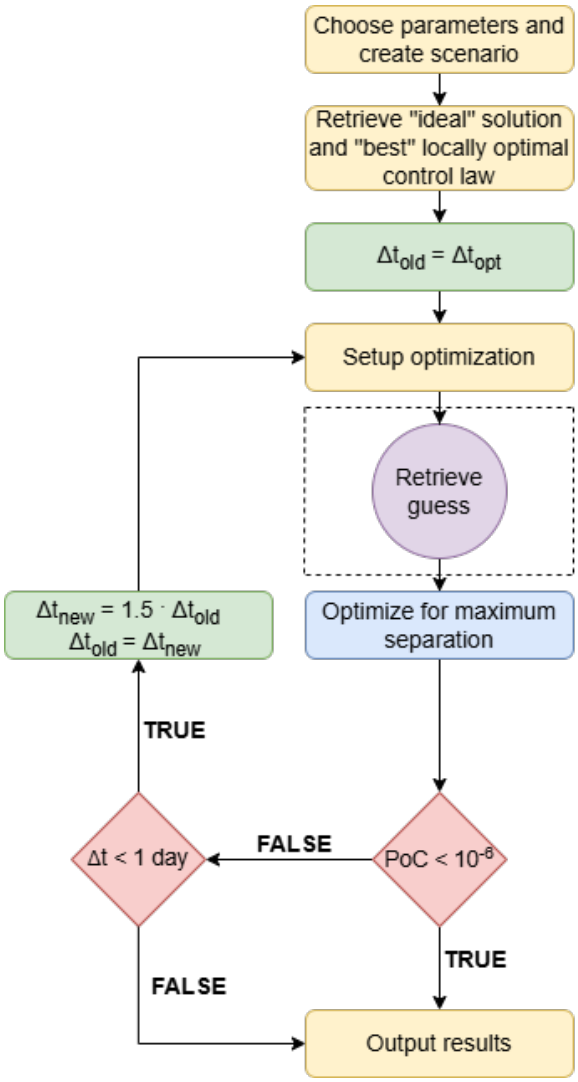

Figure 4.8: Flow of the "real" optimization algorithm

5
Research Paper

Characterizing Minimum-Time Collision Avoidance Maneuvers for Solar Sails in Earth Orbit

Giuseppe Ambrosio *
Delft University of Technology, Kluyverweg 1, 2629 HS Delft, the Netherlands

Given the potential of solar sails for applications around Earth, this paper investigates their performance in executing collision avoidance maneuvers. An extensive set of conjunctions (e.g., varying orbital regimes, sail control authorities, and collision geometries) is built. An "ideal" and a "real" case are examined, with the latter accounting for greater uncertainties (modeled via a covariance-mapping algorithm) and stricter collision probability requirements. The optimal control problem is derived and solved through direct collocation, seeking time optimality while constraining the probability. For all scenarios, maneuvers are completed within the one-day threshold, proving solar sails fit the current operational framework. Key findings are: 1) Better debris state knowledge (and later warnings) reduce maneuver time; 2) Higher altitudes increase the maneuver time, while greater sail control authority decreases it; 3) Eclipses influence results; 4) The Earth-Sun configuration only weakly affects the maneuver time; and 5) In-plane control is always non-zero. The locally optimal steering laws to change the semi-major axis and eccentricity best approximate the optimized maneuvers: especially for longer maneuver times, these straightforward laws comply with collision probability requirements.

I. Introduction

The problem of space waste originated with space exploration, and evolved with it; it was not until more recently, however, that space was recognized as a finite resource, to be treated as such [1]. The threats posed by the presence of space debris orbiting Earth are multiple. On the one hand, there is a concrete danger of collision between Resident Space Objects (RSOs); on the other hand, unique applications and functionalities could be lost (e.g., internet, weather, and communication services) [2]. Therefore, addressing the problem is fundamental, for preventing what was theorized in Reference [3]: a process of mutual collisions between the objects currently in orbit, known as the "Kessler's syndrome", that could lead to the creation of a debris belt surrounding the planet, hampering access to space.

Nowadays, the debris population is composed of approximately one million objects greater than 1 cm, and of more than one hundred million objects whose size is below 1 cm [4]. As the number of objects in space increases, the risk posed by potential collisions between space objects grows. The Probability of Collision (PoC) is a very useful metric, as

*Graduate Master's Student, Department of Astrodynamics and Space Missions, Faculty of Aerospace Engineering, gambrosio@tudelft.nl

the threshold to issue a collision warning is set on its value: if at least one of the objects is an operational spacecraft, the need for performing a Collision Avoidance Maneuver (CAM) may arise [5].

Collision avoidance is a reality in mission operations, for all satellites orbiting Earth. It has evolved significantly since Conjunction Data Messages (CDMs) became available [5], to notify satellite operators of dangerous conjunctions. CDMs are usually issued three days before the Time of Closest Approach (TCA), with subsequent messages broadcast every six to eight hours [6]. Although the operators' reaction times can range from one to twelve hours [7], a fast reaction is necessary: in Low Earth Orbit (LEO), maneuver decision is usually taken one day before the conjunction [8].

The number of received CDMs is very large, and is expected to increases as the number of RSOs grows [9]. The European Space Agency (ESA) aims at developing technologies to monitor and safely manage its space-related traffic, toward more automated collision avoidance operations [10]. Reducing in-orbit collisions and guaranteeing safe and successful disposal of space objects, which include investigating removal strategies, are among the main pillars of ESA's "Zero Debris Approach" [4].

Solar sails, characterized by a large area-to-mass ratio and reliance on Solar Radiation Pressure (SRP) rather than traditional propellants [11], are flight-proven [12–17], and are particularly interesting for their propellantless nature. Solar sails can be used in active debris removal missions, to deorbit satellites indefinitely, with multiple pieces of debris targeted within a single mission [18]. This is the purpose of the Space Waste Elimination around Earth by Photon Propulsion (SWEEP) project, developed within Delft University of Technology: employing solar sailing technologies to "clean up space and preserve the near-Earth environment" *.

Envisioning the usage of solar sails in Earth orbit requires dealing with collision avoidance strategies. Various strategies have been developed to design and optimize CAMs for conventional propulsion methods [19–27]. However, the literature lacks studies whose aim is to characterize the collision avoidance performance of solar sails around Earth. CAMs were only designed for sails (as a means of passive debris removal) in the deorbiting phase [28, 29], through simple "on/off" structures, to direct the sail either perpendicular or parallel to the atmospheric drag. Depending on the control authority of the sail and the geometry of the conjunction, a "dead zone" is found: after a certain time, it is not possible to effectively reduce the risk of collision.

Therefore, this paper aims at characterizing, for the first time, the performance of solar sails in executing CAMs, for a plethora of scenarios. Maneuvers for the minimum required time, before the TCA, are targeted, to identify the "dead zone", after which the PoC cannot be reduced below the threshold, and compare the required time with the current operational framework. The paper is structured as follows. First, the dynamical model is given in Section II. Then, the algorithms developed to define the collision scenario and optimize the CAM are outlined in Sections III and IV, respectively. Results are presented and discussed in Section V. Finally, conclusions are drawn in Section VI.

*https://www.tudelft.nl/lr/sweep (Accessed: 26 April 2024)

II. Dynamical Model

In this section, the dynamical model is outlined. Subsection II.A introduces the employed reference frames, followed by Subsection II.B, which details the choices underlying the definition of the equations of motion.

II.A. Reference Frames

In this work, the following reference frames are employed. All reference frames are assumed to be right-handed.

1) The Earth-Centered Inertial (ECI) reference frame (subscript I) is a frame $I(\hat{\mathbf{x}}_I, \hat{\mathbf{y}}_I, \hat{\mathbf{z}}_I)$ centered at the Earth's Center of Mass (CoM), with $\hat{\mathbf{x}}_I$ pointing toward the first point of Aries Υ(the mean vernal equinox at January 1$^{\text{st}}$, 2000), $\hat{\mathbf{z}}_I$ pointing perpendicular to the mean equatorial plane at January 1$^{\text{st}}$, 2000 (toward the Northern hemisphere), and $\hat{\mathbf{y}}_I$ completing the right-handed reference frame.
2) The Radial-Transverse-Normal (RTN) reference frames of the sailcraft (subscript O) $O(\hat{\mathbf{x}}_O, \hat{\mathbf{y}}_O, \hat{\mathbf{z}}_O)$ and of the debris (subscript Q) $Q(\hat{\mathbf{x}}_Q, \hat{\mathbf{y}}_Q, \hat{\mathbf{z}}_Q)$ are object-centered reference frames, with origin in the CoM of the respective object. For $K \in O, Q$, $\hat{\mathbf{x}}_K$ is parallel to the radial position vector, $\hat{\mathbf{z}}_K$ is in the direction of the orbital angular momentum vector (perpendicular to the orbital plane), and $\hat{\mathbf{y}}_K$ completes the right-handed reference frame. Basis vectors are obtained geometrically through the relations:

$$\begin{cases} \hat{\mathbf{x}}_K = \frac{\mathbf{r}_{I,k}}{||\mathbf{r}_{I,k}||} \\ \hat{\mathbf{z}}_K = \frac{\mathbf{r}_{I,k} \times \mathbf{v}_{I,k}}{||\mathbf{r}_{I,k} \times \mathbf{v}_{I,k}||} \\ \hat{\mathbf{y}}_K = \hat{\mathbf{z}}_K \times \hat{\mathbf{x}}_K \end{cases} \qquad \forall (K,k) \in \{(O, S/C), (Q, D)\} \tag{1}$$

where $\mathbf{r}_{I,k}$ and $\mathbf{v}_{I,k}$ are the inertial position and velocity vectors of the object, respectively. The cross product $\mathbf{r}_{I,k} \times \mathbf{v}_{I,k}$ defines the angular momentum vector of the object, $\mathbf{h}_{I,k}$. Subscripts S/C and D refer to the sailcraft and debris, respectively.
3) The sunlight reference frame (subscript S) is a sailcraft-centered frame $S(\hat{\mathbf{x}}_S, \hat{\mathbf{y}}_S, \hat{\mathbf{z}}_S)$ and is useful when dealing with SRP acceleration. Its origin lies in the sailcraft's CoM. $\hat{\mathbf{x}}_S$ points in the Sun-to-sailcraft direction (coincident with the direction of sunlight), $\hat{\mathbf{y}}_S$ is expressed as $\hat{\mathbf{z}}_I \times \hat{\mathbf{x}}_S$, and $\hat{\mathbf{z}}_S$ completes a right-handed reference frame.
4) The encounter reference frame (subscript M) is a sailcraft-centered frame $M(\hat{\mathbf{x}}_M, \hat{\mathbf{y}}_M, \hat{\mathbf{z}}_M)$, useful to describe conjunctions, with its origin in the sailcraft's CoM. $\hat{\mathbf{y}}_M$ points in the direction of the relative velocity between the sailcraft and the debris, $\hat{\mathbf{z}}_M$ is parallel to the cross product between the relative position and relative velocity, and $\hat{\mathbf{x}}_M$ completes a right-handed reference frame.

$$\begin{cases} \hat{\mathbf{y}}_M = \frac{\mathbf{v}_{I,S/C} - \mathbf{v}_{I,D}}{||\mathbf{v}_{I,S/C} - \mathbf{v}_{I,D}||} \\ \hat{\mathbf{z}}_M = \frac{(\mathbf{r}_{I,S/C} - \mathbf{r}_{I,D}) \times (\mathbf{v}_{I,S/C} - \mathbf{v}_{I,D})}{||(\mathbf{r}_{I,S/C} - \mathbf{r}_{I,D}) \times (\mathbf{v}_{I,S/C} - \mathbf{v}_{I,D})||} \\ \hat{\mathbf{x}}_M = \hat{\mathbf{y}}_M \times \hat{\mathbf{z}}_M \end{cases} \tag{2}$$

For a generic reference frame $K(\hat{\mathbf{x}}_K, \hat{\mathbf{y}}_K, \hat{\mathbf{z}}_K)$, assuming column basis vectors, the rotation matrices, to the inertial frame and vice versa, are:

$$R_{K \to I} = [\hat{\mathbf{x}}_K, \hat{\mathbf{y}}_K, \hat{\mathbf{z}}_K] \tag{3a}$$

$$R_{I \to K} = R_{K \to I}^T \tag{3b}$$

II.B. Equations of Motion

The dynamical model considers Earth's central gravity, Earth's J2 perturbation, and SRP acceleration. In the ECI frame, the equations describing the motion of the sail around the Earth are:

$$\begin{cases} \dot{\mathbf{r}}_{I,S/C} = \mathbf{v}_{I,S/C} \\ \ddot{\mathbf{r}}_{I,S/C} = \mathbf{a}_{I,S/C,\mu_\oplus} + \mathbf{a}_{I,S/C,J2} + \mathbf{a}_{I,S/C,SRP}(\mathbf{u}(t)) \end{cases} \tag{4}$$

where $\mathbf{a}_{I,S/C}$ is the inertial acceleration vector of the sail, $\mathbf{u}$ is the control vector, t is the time variable, and the subscripts $\mu_\oplus$, $J2$, and SRP refer to the acceleration given by the Earth's central gravity, Earth's oblateness, and solar radiation pressure, respectively. The SRP acceleration depends on the control vector, defining the orientation of the sail with respect to the sunlight.

Most collision avoidance studies model Keplerian motion for the maneuvering satellite, due to the very small changes in the nominal trajectory introduced by the CAM [30]. Studies identified that, for some specific conjunction geometries, results can be affected by Earth's oblateness [19, 22, 23]. It is therefore decided to consider the J2 acceleration in the equations of motion. Moreover, the J2 effect is relevant for a Sun-Synchronous Orbit (SSO), the envisioned target orbit for the Advanced Composite Solar Sail System (ACS3), the latest solar sailing mission, launched in 2024 [17].

Although CAM studies neglected the effect of atmospheric accelerations, such a perturbation could be predominant for solar sails, characterized by high area-to-mass ratios [31]: in LEO, there is indeed a minimum operating altitude, below which the atmospheric drag becomes excessive. To stay conservative, the minimum operating altitude for the sailcraft under analysis is set to 1000 km, such that atmospheric effects can be ignored [32].

Ephemerides are retrieved from the National Aeronautics and Space Administration (NASA)'s Spacecraft, Planet, Instrument, C-matrix, Events (SPICE) interface [†]. Considering the short duration of CAMs, the position of the Sun is assumed to remain constant at its value at the TCA.

[†] https://naif.jpl.nasa.gov/naif/ (Accessed: 15 May 2024)

Propagation of the state vector (defined by the position and velocity in Cartesian coordinates) is performed employing the *ode89* function [33] in MATrix LABoratory (MATLAB), with relative and absolute tolerances of 10^{-12} and 10^{-8}, respectively, to achieve high accuracy [34].

1. Earth's Central Gravity and Oblateness

The expressions for the acceleration given by Earth's central gravity and oblateness are given in Reference [35]:

$$\mathbf{a}_{I,S/C,\mu_\oplus} = -\frac{\mu_\oplus}{r_{I,S/C}^3}\mathbf{r}_{I,S/C} \tag{5}$$

$$\mathbf{a}_{I,S/C,J2} = -\frac{3}{2}\frac{\tilde{R}_\oplus^2}{r_{I,S/C}^5}J2\mu_\oplus[(r_{I,S/C,x}\hat{\mathbf{x}}_I + r_{I,S/C,y}\hat{\mathbf{y}}_I)(1-5\frac{r_{I,S/C,z}^2}{r_{I,S/C}^2}) + r_{I,S/C,z}(3-5\frac{r_{I,S/C,z}^2}{r_{I,S/C}^2})\hat{\mathbf{z}}_I] \tag{6}$$

where $\mu_\oplus = 3.986004418 \cdot 10^{14}\ \frac{\mathrm{m}^3}{\mathrm{s}^2}$ [35] is the gravitational parameter of the Earth, $r_{I,S/C}$ is the norm of the planetocentric position vector $\mathbf{r}_{I,S/C}$, $\tilde{R}_\oplus = 6378.14$ km [35] is the mean equatorial radius of the Earth, $J2 = 1.082626925639 \cdot 10^{-3}$ is the Earth's J2 gravitational field constant [36], and, for a vector in a generic reference frame K, the subscripts x, y, z refer to the Cartesian coordinates of the vector along the basis vectors of the given frame $\hat{\mathbf{x}}_K, \hat{\mathbf{y}}_K, \hat{\mathbf{z}}_K$, respectively.

2. Solar Radiation Pressure

The ideal SRP model is employed. The solar sail is assumed to be a perfectly reflective, flat, rigid surface, with a constant area-to-mass ratio; moreover, the SRP value is considered to be constant, and the SRP acceleration is assumed to act along the spacecraft's CoM, with negligible effects on the spacecraft bus [37].

For an ideal, perfectly reflective solar sail, the acceleration is orientated normally to the surface of the sail, and is given in Reference [11] as:

$$\mathbf{a}_{I,S/C,SRP} = \nu a_c (\frac{\gamma_E}{\gamma_{S/C}})^2 cos^2(\alpha)\hat{\mathbf{n}}_I \tag{7}$$

where $\nu \in [0, 1]$ is the shadow factor, γ_E is the distance between the Earth and the Sun, $\gamma_{S/C}$ is the distance between the spacecraft and the Sun, α is the cone angle (measured between the direction of sunlight and the sail normal direction), $\hat{\mathbf{n}}_I$ is the unit vector normal to the sail membrane in the inertial frame, and a_c is the characteristic acceleration. The characteristic acceleration is defined as the acceleration produced at the Earth-Sun distance (1 au), when the sail is perpendicular to the direction of sunlight [11]. It depends on the area-to-mass ratio.

Eclipsing events are modeled through a conical shadow model [37], using $\tilde{R}_\odot = 6.95508 \cdot 10^5$ km [35] as the mean solar radius, with "penumbra" considered equal to "umbra" as in References [31, 37].

III. Collision Scenario Definition

In this section, the collision is characterized. First, the desired conjunction scenarios are defined in Subsection III.A. Next, in Subsection III.B, the assumptions behind the PoC computation and the selected method are outlined. Then, the assumptions and the implementation of the uncertainty retrieval algorithm are given in Subsection III.C.

III.A. Design Parameters

The purpose of this study is to assess the performance of solar sails in avoiding collisions: since collisions can happen in a plethora of different ways, key design parameters are identified to build the desired conjunction scenarios, at the closest approach. The nominal TCA is defined first. Then, three categories of parameters are identified: those characterizing the sail and its orbit around Earth, those characterizing the debris object, and those defining the conjunction (in terms of collision geometry). For an overview of all the design parameters and their values, see Table 4.

1. Time of the Closest Approach

Since the vernal and autumn equinoxes represent the "worst-case scenario" for eclipsing events [37, 38], simulations are centered at the vernal equinox: specifically, the TCA is set to March 20$^{\text{th}}$ 2023 [‡].

2. Sail Parameters

The sail parameters are those that influence the control authority of the sail and its orbit at the TCA. As the first iteration of this study, the sailcraft is placed in a circular orbit (whose eccentricity is zero). The following variables are changed:

- **Area-to-mass ratio**: three values are tried, namely 5 $\frac{\text{m}^2}{\text{kg}}$ (from ACS3 [39]), 4 $\frac{\text{m}^2}{\text{kg}}$, and 3 $\frac{\text{m}^2}{\text{kg}}$, where the latter two represent more conservative scenarios.
- **Altitude**: Altitudes in LEO, at 1000 km and 1800 km, and in Geostationary Orbit (GEO), at 35786 km, are simulated, as these are the protected orbital regions [40]. SSOs at 1000 km, in LEO, are included, given the target injection orbit for ACS3 was an SSO with an altitude of 1000 km [17].
- **Inclination**: As the whole spherical shell is protected in LEO, while only equatorial orbits are protected in GEO [40], orbits with an inclination of 0, 45, and 90 degrees are simulated in LEO, whereas only equatorial orbits (with zero inclination) are simulated in GEO. For SSOs, the inclination is fixed at 99.5 degrees, to satisfy the Sun-synchronicity condition at 1000 km [35].
- **Right ascension of the ascending node**: To study different orbit orientations, a Right Ascension of the Ascending Node (RAAN) of 0, 45, and 90 degrees is tested. Note that for equatorial orbits the RAAN is not defined and set at 0 degrees. For SSOs, three values of the Local Time of the Ascending Node (LTAN) are selected: 6 ("dawn-dusk" orbit), 9, and 12 ("noon-midnight" orbit) AM. The LTAN in turn defines the RAAN of the orbit: at the vernal

[‡] https://www.astropixels.com/ephemeris/soleq2001.html (Accessed: 14 June 2024)

equinox, an LTAN of 6, 9, and 12 AM corresponds to a RAAN of 270, 315, and 360 degrees, respectively.

- **True anomaly at TCA**: The true anomaly of the sailcraft at the TCA is changed to place the sailcraft in four different illumination conditions, which are deemed the most significant to evaluate the sail performance: full sunlight, sunlight/eclipse transition, full eclipse, eclipse/sunlight transition. If the spacecraft is not subject to eclipses, four equally spaced values of true anomaly are used: 0, 90, 180, and 270 degrees.

Jointly changing the inclination and the RAAN is fundamental to simulate the effect of different directions of the sunlight with respect to the orbital plane, known to drive solar-sail performance [41]. For a generic sailcraft orbit, an aspect angle β is defined as the angle between the sunlight direction and the angular momentum vector, perpendicular to the orbital plane:

$$cos(\beta) = |\frac{\mathbf{h}_{I,S/C}}{||\mathbf{h}_{I,S/C}||} \cdot (R_{S\rightarrow I}\,\hat{\mathbf{x}}_S)| \tag{8}$$

The aspect angle is defined between 0 and 90 degrees (hence the absolute value operator in Eq. 8) so that orbits whose orbital planes are reached by the sunlight at the same angle are treated similarly. Numerical values are provided in Tables 1 and 2, for the position of the Sun at the vernal equinox. It is important to use the aspect angle to generalize the results to different Earth-Sun configurations (namely, other times of the year).

Table 1 Aspect angle, in degrees, for different combinations of inclination and RAAN

	i = 0 deg	i = 45 deg	i = 90 deg
$RAAN$: 0 deg	90	90	90
$RAAN$: 45 deg	90	60	45
$RAAN$: 90 deg	90	45	0

Table 2 Aspect angle, in degrees, for different values of LTAN

	i = 99.5 deg
$LTAN$: 6 AM	10
$LTAN$: 9 AM	45
$LTAN$: 12 AM	90

3. Debris Parameters

Debris parameters are the orbital eccentricity and the size, which allow a characterization of the objects, synthetically created for the simulations.

Most trackable objects have near-circular orbits, and more than 80% of the objects have an eccentricity below 0.1 [42]. Therefore, it is safe to assume debris objects in circular orbits (with zero eccentricity).

As the debris mass does not influence the PoC computation, the only relevant variable is the radial size of the object: in the definition of the orbital classes in the Assessment of Risk Event Statistics (ARES) tool, employed by ESA, the debris size plays a role, since smaller objects are subject to greater uncertainties [43]. Due to the change of the detection threshold based on the altitude, the smallest tested radial size is fixed at 0.125 m in LEO, and at 0.35 m in GEO [43]. Other simulated sizes are 1 and 10 m.

4. Conjunction Parameters

The variables treated as conjunction parameters are those which directly influence the collision geometry, as the factors which allow the retrieval of the debris position and velocity vectors at the TCA, starting from the nominal state of the sail at the TCA.

1) **Debris position vector retrieval**

The debris position vector is found, as shown in Fig. 1a, by the sum between the sail position vector and the designed miss vector, defined in the inertial frame as:

$$\mathbf{r}_{I,miss}(TCA) = \mathbf{r}_{I,D}(TCA) - \mathbf{r}_{I,S/C}(TCA) \tag{9}$$

The miss vector can be characterized in terms of magnitude and direction. Three values of miss distance are used (1, 10, 100 meters), and the miss direction is one of the three basis vectors of the RTN frame of the sailcraft $O(\hat{\mathbf{x}}_O, \hat{\mathbf{y}}_O, \hat{\mathbf{z}}_O)$.

2) **Debris velocity vector retrieval**

Since both objects are on circular orbits, the collision happens in a plane perpendicular to the position vectors of the sailcraft and the debris at the TCA [42]. One rotation angle ξ (the encounter angle), about the sail position vector, needs to be defined, as the angle between the sail and debris velocity directions, at the TCA (see Fig. 1b):

$$cos(\xi) = \frac{\mathbf{v}_{I,S/C}(TCA) \cdot \mathbf{v}_{I,D}(TCA)}{||\mathbf{v}_{I,S/C}(TCA)(TCA)||\,||\mathbf{v}_{I,D}(TCA)||} \tag{10}$$

Seven values of encounter angle are used: all the angles between 45 and 315 degrees, with 45 degrees increments. The fully collinear case ($\xi = 0$ deg) is excluded, assuming short-term encounters, which are the most common ones. The short-term assumption of large relative velocities (of several kilometers per second) [44] would be invalidated by near-zero relative velocities in perfectly coplanar, circular orbits.

For circular debris orbits, the velocity magnitude equals [35]:

$$v_{I,D}(TCA) = \sqrt{\frac{\mu_{\oplus}}{r_{I,D}(TCA)}} \tag{11}$$

where $r_{I,D}$ and $v_{I,D}$ are the norms of the debris inertial position ($\mathbf{r}_{I,D}$) and velocity ($\mathbf{v}_{I,D}$) vectors, respectively. An additional quantity can be included among those under analysis: the azimuth angle $\tilde{A}$. It is a parameter often employed to study collisions and, based on Reference [42], defined as:

$$\cos(\tilde{A}) = -\frac{\Delta\mathbf{v}(TCA) \cdot \mathbf{v}_{I,S/C}(TCA)}{||\Delta\mathbf{v}(TCA)||\,||\mathbf{v}_{I,S/C}(TCA)||} \tag{12}$$

where $\Delta\mathbf{v} = \mathbf{v}_{I,D} - \mathbf{v}_{I,S/C}$. The azimuth angle describes the angle between the relative velocity direction and the sailcraft velocity direction: Table 3 summarizes the relation between encounter and azimuth angles.

Table 3 Relation between encounter and azimuth angles

Encounter angle [deg]	45	90	135	180	225	270	315
Azimuth angle [deg]	67.5	45	22.5	0	22.5	45	67.5

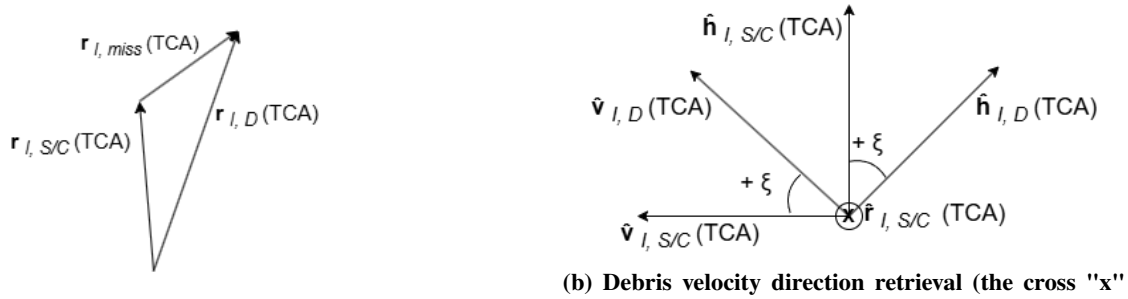

(a) Debris position vector retrieval

(b) Debris velocity direction retrieval (the cross "x" indicates an inward vector)

Fig. 1 Retrieval of the debris position vector and the debris velocity direction

Table 4 Overview of the design parameters and their values in LEO, GEO, and SSO

Parameter	Values in LEO	Values in GEO	Values in SSO
TCA	Vernal equinox	Vernal equinox	Vernal equinox
Area-to-mass ratio (sail) [$\frac{\text{m}^2}{\text{kg}}$]	3, 4, 5	3, 4, 5	3, 4, 5
Eccentricity (sail) [-]	0	0	0
Altitude (sail) [km]	1000, 1800	35786	1000
Inclination (sail) [deg]	0, 45, 90	0	99.5
RAAN (sail) [deg] or LTAN (sail) [h]	0, 45, 90	0	6 AM, 9 AM, 12 AM
True anomaly at TCA (sail)	1 - Full sunlight, 2 - Sunlight/eclipse, 3 - Full eclipse, 4 - Eclipse/sunlight, or [0, 90, 180, 270] deg	1 - Full sunlight, 2 - Sunlight/eclipse, 3 - Full eclipse, 4 - Eclipse/sunlight, or [0, 90, 180, 270] deg	1 - Full sunlight, 2 - Sunlight/eclipse, 3 - Full eclipse, 4 - Eclipse/sunlight, or [0, 90, 180, 270] deg
Eccentricity (debris) [-]	0	0	0
Size (debris) [m]	0.125, 1, 10	0.35, 1, 10	0.125, 1, 10
Miss distance [m]	1, 10, 100	1, 10, 100	1, 10, 100
Miss direction	$\hat{\mathbf{x}}_O, \hat{\mathbf{y}}_O, \hat{\mathbf{z}}_O$	$\hat{\mathbf{x}}_O, \hat{\mathbf{y}}_O, \hat{\mathbf{z}}_O$	$\hat{\mathbf{x}}_O, \hat{\mathbf{y}}_O, \hat{\mathbf{z}}_O$
Encounter angle [deg]	45, 90, 135, 180, 225, 270, 315	45, 90, 135, 180, 225, 270, 315	45, 90, 135, 180, 225, 270, 315
Azimuth angle [deg]	0, 22.5, 45, 67.5	0, 22.5, 45, 67.5	0, 22.5, 45, 67.5

III.B. Probability Computation

The PoC computation arises from the fact that there are inevitable errors in orbit determination: errors can be described using a three-dimensional Probability Density Function (PDF). Collision probability is computed through the trivariate integration of the PDF of the uncertainty in the state of the two RSOs in a control volume. In this subsection, the assumptions underlying the PoC computation are outlined and a suitable method is chosen, among existing ones.

Cumulative probability methods are considered, as most applications require the PoC for two RSOs during a period of interest [44]. As explained in the previous subsection, short-term encounters are dealt with, thus the relative trajectory is a straight line and the swept volume is an infinitely long cylinder [44]: this reduces the problem to a two-dimensional integration, along the relative velocity direction. Moreover, PoC computation methods rely on the positional errors being zero-mean, Gaussian, and uncorrelated, and model the objects as spheres [45]. For both objects, the radius of the circumscribing sphere will be considered: hence, a square sail is assumed, which is the most commonly employed configuration [46].

Foster's method, which maps the object location in the encounter plane through polar coordinates [47], is chosen, since it is publicly available via the Collision Avoidance Risk Assessment (CARA) tool, by NASA [§]. In Foster's method, the conjunction is studied in the encounter reference frame $M(\hat{\mathbf{x}}_M, \hat{\mathbf{y}}_M, \hat{\mathbf{z}}_M)$. The integration domain is represented by the encounter plane $(\hat{\mathbf{x}}_M, \hat{\mathbf{z}}_M)$, perpendicular to the relative velocity. The algorithm takes as input, for both objects, the state at the TCA, the covariance at the TCA, and the radial size.

III.C. Uncertainty Retrieval

As mentioned in the previous subsection, the covariance of the two objects is required in the PoC computation. This subsection thus lists four main sets of assumptions, made to model the uncertainties. Then, the procedures followed by ARES are briefly presented. Finally, the uncertainty retrieval algorithm implemented for this work is introduced.

The first set of assumptions characterizes short-term encounters: no uncertainty on the velocity is considered, and the position uncertainty is assumed constant during the encounter, equal to the value at the TCA [44]. A second set of assumptions comes from the PoC computation: position errors are uncorrelated, and the size of the objects is obtained by modeling them as spheres [45]. For uncorrelated errors, the total covariance is the sum of the covariance of the two RSOs. Additionally, the sailcraft is assumed to have an on-board Global Positioning System (GPS) receiver, as is the case for the ACS3 mission [39]. The uncertainty of the sailcraft position can thus be neglected [48], and only the uncertainty concerning the debris position needs to be modeled. A fourth assumption regards the shape of the covariance matrix, which is modeled as diagonal in the RTN frame of the debris $Q(\hat{\mathbf{x}}_Q, \hat{\mathbf{y}}_Q, \hat{\mathbf{z}}_Q)$ [24, 48].

In ARES, the overall CDM population is divided per orbital class (based on the size, perigee altitude, inclination,

[§] https://github.com/nasa/CARA_Analysis_Tools (Accessed: 10 June 2024)

and eccentricity of the object), and regression is performed to obtain [43]:

$$\begin{cases} \sigma_{\hat{\mathbf{x}}_Q} = \tau_{1,\hat{\mathbf{x}}_Q} \cdot 10^{\tau_{2,\hat{\mathbf{x}}_Q} \cdot \zeta} \\ \sigma_{\hat{\mathbf{y}}_Q} = \tau_{1,\hat{\mathbf{y}}_Q} \cdot (\tau_{3,\hat{\mathbf{y}}_Q} + \zeta)^{\tau_{2,\hat{\mathbf{y}}_Q}} \\ \sigma_{\hat{\mathbf{z}}_Q} = \tau_{1,\hat{\mathbf{z}}_Q} \cdot 10^{\tau_{2,\hat{\mathbf{z}}_Q} \cdot \zeta} \end{cases} \tag{13}$$

where σ is the position standard deviation, τ denotes a generic regression coefficient, ζ is the time interval before the TCA, and the subscripts $\hat{\mathbf{x}}_Q$, $\hat{\mathbf{y}}_Q$, $\hat{\mathbf{z}}_Q$ refer to the uncertainties along the basis vectors $\hat{\mathbf{x}}_Q$,$\hat{\mathbf{y}}_Q$,$\hat{\mathbf{z}}_Q$, respectively.

CDMs are not publicly accessible. Therefore, a full regression cannot be performed. In 2019, ESA shared a batch of 162,634 CDMs, collected between 2015 and 2019, corresponding to 13,154 unique events, for a challenge [¶]. These CDMs have been used in the literature to model realistic conjunctions [22, 23]. Nevertheless, shared information only covers a few orbital classes: for most classes, there are no items at all, whereas, for some others, the number of items is not large enough to be statistically significant (at least 100 elements are required). The solution to the data unavailability comes from ARES. Before the advent of CDMs, if Conjunction Summary Messages (CSMs) did not provide a reliable source of data, Two-Line Elements (TLEs) were used to fill the gaps, operating by analogy: for those classes where both TLE and CSM information was available, it was possible to obtain a mapping factor between them and apply that factor to classes where there were only TLEs but no CSMs [43].

A mapping algorithm is therefore implemented in this work to retrieve the uncertainties (Algorithm 1). The starting point is to identify a reference orbital class among those available in the CDM dataset: near-circular polar orbits with an altitude between 800 and 25000 km are selected. A mapping factor is computed for the reference orbital class, between TLE and CDM data, and is then applied to all other orbital classes. The inputs of Algorithm 1 are the orbital class and the size of the debris object, and the time before the closest approach. Ranges for the parameters (see Table 5) are chosen based on Reference [49], for the perigee altitude, eccentricity, and inclination, and on Reference [43], for the debris size. The time horizon to retrieve uncertainties goes from zero to seven days before the TCA: the reason is that the employed CDM dataset spans such an interval, and that usually orbit determination covers weekly periods [50].

Algorithm 1 Debris position uncertainty retrieval

Require: Orbital class of the debris object, size of the debris object, time interval ζ before the closest approach
1: **Compute:** TLE regression functions for the chosen orbital class (based on Eqs. 13)
2: **Retrieve:** TLE regression functions for the reference orbital class (based on Eqs. 13)
3: **Retrieve:** CDM regression functions for the reference orbital class and chosen debris size (based on Eqs. 13)
4: **Compute:** Mapping factors for the reference orbital class and chosen debris size
5: **Apply**: Mapping factors to the chosen orbital class and chosen debris size through Eqs. 14
6: **Compute:** Uncertainties for the given time interval ζ before the closest approach
Ensure: Debris position covariance matrix for the given time interval before the closest approach

[¶] https://kelvins.esa.int/collision-avoidance-challenge/ (Accessed: 24 June 2024)

Table 5 Overview of the ranges of the parameters in the uncertainty retrieval algorithm

Parameter	Symbol	Ranges
Size [m^2]	s	$s \leq 1$
		$s > 1$
Perigee altitude [km]	$\tilde{h}_p$	$\tilde{h}_p \leq 800$
		$800 < \tilde{h}_p \leq 25000$
		$\tilde{h}_p > 25000$
Eccentricity [-]	e	$e \leq 0.1$
		$e > 0.1$
Inclination [deg]	i	$i \leq 30$
		$30 < i \leq 60$
		$i > 60$

First, based on the orbital class, TLE uncertainties are generated. For the orbital class of interest, the initial diagonal covariance matrix, in the RTN frame of the debris, is built from the TLE uncertainties provided in Reference [49], following the approach in Reference [43]. The TLE-based covariance is propagated in time through the state transition matrix [51]. A Monte Carlo campaign (sampling 1000 items with a Sobol distribution) is carried out, propagating the uncertainty for different values of the time before the closest approach. For all the Monte Carlo samples, uncertainties are extracted from the final covariance matrix (at the TCA). Once a TLE-based uncertainty dataset is built for the chosen class, a linear regression is carried out: since Eqs. 13 show a non-linear relation between the uncertainty and the time, logarithmic transformations are applied before performing the regression. Coefficients are retrieved via the linear regression tools available in MATLAB. The regression from the TLE data, for the reference orbital class, is performed in the same way. For the CDM data, instead, a linear regression to obtain the coefficients in Eqs. 13 is done without the need to propagate the uncertainties: CDMs already provide the covariance at the TCA. For the CDM information, a distinction is made between "small" and "large" objects, based on the chosen debris size in Algorithm 1.

The mapping factors are computed as the ratios between the regression functions (along $\hat{\mathbf{x}}_Q$,$\hat{\mathbf{y}}_Q$,$\hat{\mathbf{z}}_Q$) from the CDM and the TLE data, for the reference orbital class and chosen debris size. They are applied to retrieve time-dependent regression functions, whose input is the time interval before the TCA, to compute the uncertainties and build the covariance matrix at the TCA for the chosen orbital class and debris size. The mapping works as follows:

$$q^{(\psi)}_{CDM,\,class\,2,\,dim}(\zeta) = \underbrace{\frac{q^{(\psi)}_{CDM,\,class\,1,\,dim}(\zeta)}{q^{(\psi)}_{TLE,\,class\,1}(\zeta)}}_{\text{Mapping factor for direction } \boldsymbol{\psi}} \cdot q^{(\psi)}_{TLE,\,class\,2}(\zeta) \qquad \forall \boldsymbol{\psi} \in \{\hat{\mathbf{x}}_Q, \hat{\mathbf{y}}_Q, \hat{\mathbf{z}}_Q\} \tag{14}$$

where the mapped regression function, from the CDM data, q_{CDM}, for the chosen orbital class ($class\,2$) and debris size (dim), in direction $\boldsymbol{\psi}$, is obtained from the corresponding function, from the TLE data, q_{TLE}, scaled by the mapping factor derived for the reference orbital class ($class\,1$) and the same debris size (dim), in direction $\boldsymbol{\psi}$.

IV. Optimization Setup

Once the simulation scenario is defined, the Optimal Control Problem (OCP) is formulated and solved. Subsection IV.A explains the choice of a fixed-time-horizon optimization, which leads, in Subsection IV.B, to the definition of the OCP to be solved. Subsection IV.C presents the selected optimizer and optimization settings. Finally, two optimization cases are outlined in Subsection IV.D: the "ideal" and the "real" cases.

IV.A. Fixed-Time-Horizon Optimization

The goal of the optimization is to find the minimum maneuver time Δt for which the sailcraft can perform a CAM, bringing the PoC below a threshold, thus the problem would have a free initial time. Maneuvers are designed to end at the (fixed) TCA as the minimum required warning time, before the TCA, is sought. However, solving the OCP with free initial time adds complexity to the problem and presents challenges to the numerical convergence [52]. Therefore, the OCP is formulated as a fixed-time-horizon optimization problem, and the optimal maneuver time will be found through iterations, following the approach in Reference [53]. The expression "major iterations" is used to refer to the iterations to identify the optimal maneuver time, varying the maneuver start epoch t_{MAN}.

IV.B. Optimal Control Problem

Solving the OCP consists of finding a state history $\boldsymbol{\rho}(t)$ and a control history $\mathbf{u}(t)$, with the time t being the independent variable, to minimize a cost function J, while constraints are satisfied [53]. In this subsection, after defining the objective function and the optimization variables and constraints, the structure of the OCP is provided in Problems 25 and 26.

As mentioned in the previous subsection, the objective of a single "major iteration" is not the maneuver time. Two objective functions can be formulated, based on References [23, 27–29]:

- **Maximum separation**: the objective is to maximize the distance between the sail and the debris object at the TCA. The formulation of the cost function J, to be minimized, is straightforward:

$$J = \frac{1}{\Delta\mathbf{r}^T(TCA) \cdot \Delta\mathbf{r}(TCA)} \tag{15}$$

  where $\Delta\mathbf{r} = \mathbf{r}_{I,S/C} - \mathbf{r}_{I,D}$.

- **Minimum collision probability**: the objective is to minimize the collision probability at the TCA. Hence, the Squared Mahalanobis Distance (SMD) is introduced, based on Reference [24]:

$$d = \Delta\mathbf{r}^T_{(\hat{\mathbf{x}}_M,\hat{\mathbf{z}}_M)}(TCA)C^{-1}_{(\hat{\mathbf{x}}_M,\hat{\mathbf{z}}_M)}(TCA)\Delta\mathbf{r}_{(\hat{\mathbf{x}}_M,\hat{\mathbf{z}}_M)}(TCA) \tag{16}$$

  where C is the position covariance matrix and the subscript $(\hat{\mathbf{x}}_M, \hat{\mathbf{z}}_M)$ refers to the projection on the encounter

plane (see Subsection III.B). The SMD is useful as it is analytically linked to the collision probability, being inversely proportional to it [48]. Thus, the cost function J, to be minimized, is formulated as the maximization of the SMD:

$$J = \frac{1}{\Delta \mathbf{r}^T_{(\hat{\mathbf{x}}_M, \hat{\mathbf{z}}_M)}(TCA) C^{-1}_{(\hat{\mathbf{x}}_M, \hat{\mathbf{z}}_M)}(TCA) \Delta \mathbf{r}_{(\hat{\mathbf{x}}_M, \hat{\mathbf{z}}_M)}(TCA)} \tag{17}$$

The OCP is posed as a one-phase problem, with fixed initial and final times. The time horizon is written as $t \in [t_{0,iter}, t_f]$, where t_0 is the initial time, which varies across "major iterations" (the subscript $iter$ refers to a generic "major iteration"), and t_f is the final time (TCA), fixed at the vernal equinox (see Table 4).

The state history consists of the state vector (in Cartesian position and velocity) of the sail, in the ECI frame:

$$\boldsymbol{\rho}(t) \in \mathbb{R}^6 \quad \text{with} \quad \boldsymbol{\rho}(t) = [r_{I,S/C,x}(t), r_{I,S/C,y}(t), r_{I,S/C,z}(t), v_{I,S/C,x}(t), v_{I,S/C,y}(t), v_{I,S/C,z}(t)]^T \tag{18}$$

Following the approach in Reference [54], the control history is represented by the Cartesian components of the normal vector to the solar sail (equivalent to the unit solar sail acceleration vector), expressed in the sunlight frame:

$$\mathbf{u}(t) \equiv \mathbf{n}_S(t) \in \mathbb{R}^3 \quad \text{with} \quad \mathbf{n}_S(t) = [n_{S,x}(t), n_{S,y}(t), n_{S,z}(t)]^T \tag{19}$$

Constraints on the state are expressed as:

$$\dot{\boldsymbol{\rho}}(t) = \mathbf{f}(t, \boldsymbol{\rho}(t), R_{S \to I} \cdot \mathbf{u}(t)) \tag{20}$$

$$\boldsymbol{\rho}(t_0) = \boldsymbol{\rho}_0 \tag{21}$$

$$\boldsymbol{\rho}_{\min} \leq \boldsymbol{\rho}(t) \leq \boldsymbol{\rho}_{\max} \tag{22}$$

Equation 20 enforces the dynamical constraint, with the dynamical function given in Eqs. 4. Since the dynamics are expressed in the ECI frame, the control vector is rotated from the sunlight to the inertial frame through the matrix $R_{S \to I}$. Equation 21 constrains the initial state of the sail, obtained by back-propagation, starting from the nominal state of the sail at the TCA. Equation 22 sets the lower and upper bounds on the state to arbitrarily small and large values, respectively. The bounds are defined as multiples of the norms of the initial position and velocity: specifically, factors of -10 and 10 are employed for the lower and upper bounds, respectively.

Constraints on the control are given as:

$$[0, -1, -1]^T \leq \mathbf{u}(t) \leq [1, 1, 1]^T \tag{23}$$

$$||\mathbf{u}(t)|| = 1 \tag{24}$$

Equation 23 imposes the bounds: the first component, in the sunlight frame, is kept between 0 and 1, as the thrust cannot point to the Sun [11]. Equation 24 enforces a path constraint, to ensure the control vector is unity throughout the trajectory.

The definition of two objective functions (Eqs. 15 and 17) leads to two separate optimal control problems, subject to the same constraints (Eqs. 20-24). For clarity, the OCP for the maximum separation is reported in Problem 25:

$$\begin{aligned}
&\underset{\mathbf{u}(t)}{\text{minimize}} && J = \frac{1}{\Delta\mathbf{r}^T(TCA)\cdot\Delta\mathbf{r}(TCA)} && \text{(Maximum separation)}\\
&\text{subject to} && \dot{\boldsymbol{\rho}}(t) = \mathbf{f}(t, \boldsymbol{\rho}(t), R_{S\to I}\cdot\mathbf{u}(t)) && \text{(State dynamics)}\\
& && \boldsymbol{\rho}(t_0) = \boldsymbol{\rho}_0 && \text{(State initial condition)}\\
& && \boldsymbol{\rho}_{\min} \le \boldsymbol{\rho}(t) \le \boldsymbol{\rho}_{\max} && \text{(State bounds)}\\
& && [0,-1,-1]^T \le \mathbf{u}(t) \le [1,1,1]^T && \text{(Control bounds)}\\
& && ||\mathbf{u}(t)|| = 1 && \text{(Control path constraints)}
\end{aligned} \tag{25}$$

The OCP for the minimum collision probability is reported in Problem 26:

$$\begin{aligned}
&\underset{\mathbf{u}(t)}{\text{minimize}} && J = \frac{1}{\Delta\mathbf{r}^T_{(\hat{\mathbf{x}}_M,\hat{\mathbf{z}}_M)}(TCA)C^{-1}_{(\hat{\mathbf{x}}_M,\hat{\mathbf{z}}_M)}(TCA)\Delta\mathbf{r}_{(\hat{\mathbf{x}}_M,\hat{\mathbf{z}}_M)}(TCA)} && \text{(Minimum PoC)}\\
&\text{subject to} && \dot{\boldsymbol{\rho}}(t) = \mathbf{f}(t, \boldsymbol{\rho}(t), R_{S\to I}\cdot\mathbf{u}(t)) && \text{(State dynamics)}\\
& && \boldsymbol{\rho}(t_0) = \boldsymbol{\rho}_0 && \text{(State initial condition)}\\
& && \boldsymbol{\rho}_{\min} \le \boldsymbol{\rho}(t) \le \boldsymbol{\rho}_{\max} && \text{(State bounds)}\\
& && [0,-1,-1]^T \le \mathbf{u}(t) \le [1,1,1]^T && \text{(Control bounds)}\\
& && ||\mathbf{u}(t)|| = 1 && \text{(Control path constraints)}
\end{aligned} \tag{26}$$

IV.C. Optimal Control Problem Solver

Direct optimization methods are robust, flexible, and easy to initialize, variables have a clear physical meaning, and complex constraints are easily handled [55]. Although they could become ill-conditioned for many-revolution problems [56], there is little danger that this will happen, given the short CAM duration. They are therefore chosen to solve the OCPs 25 and 26. Among existing tools, the second version of the General Purpose Optimal Control Software

(GPOPS-II) is selected. It is widely recognized as a state-of-the-art optimization software, employed for solving low-thrust (and solar sailing) OCPs [55]. It is often used as a verification tool for novel algorithms [57], including solar sailing trajectory optimization [58]. For an accurate explanation of the GPOPS-II algorithm, one can refer to Reference [59].

To ensure convergence, the Non-Linear Programming (NLP) problem should be properly scaled [56] so that the variables are close to unity. Custom scaling quantities are employed, based on Reference [53]. The position and velocity are scaled by the norm of the initial position and velocity from the initial guess, respectively. Scaling parameters for the time and the acceleration are obtained by dimensional analysis, while no scaling is applied to the controls, since the components of the vector normal to the sail are already bounded between -1 and +1 (see Eq. 23).

The optimizer settings are given in Table 6: values are found by trial and error (evaluating the solution in terms of computational speed as well as of smoothness of the state and control profiles), and by comparison with solved optimization problems [60]. One can refer to Reference [60] for a detailed explanation of all settings. The choices for the settings are justified by numerically integrating the optimal control solutions, verifying that the difference between the resulting state history and the state from GPOPS-II falls below a set threshold. The Interior Point Optimizer (IPOPT) is the chosen NLP solver, since it is already available once the GPOPS-II license is purchased.

Table 6 Overview of the GPOPS-II settings to solve the optimal control problem

GPOPS-II setting	Choice
Mesh method	'hp-LiuRao-Legendre'
Mesh tolerance	10^{-4}
Mesh maximum iterations	10
Mesh maximum collocation points	15
Mesh minimum collocation points	6
Mesh collocation points per interval	6
Number of mesh intervals	20
IPOPT linear solver	'ma57'
IPOPT tolerance	10^{-4}
IPOPT maximum iterations	2000
Derivative supplier	Forward differences
Derivative level	'second'
Derivative dependencies	'sparseNaN'
Method	'Differentiation'

IV.D. "Ideal" and "Real" Optimization Case

Two optimization cases are defined: the "ideal" and "real" cases. They differ in terms of probability requirement for the maneuver, covariance retrieval epoch, optimal control problem to be solved, guess generation algorithm for the first "major iteration", and scheme employed to perform the "major iterations". Table 7 summarizes the key differences

between the two optimization cases. In this subsection, for both cases, firstly the choices regarding the target PoC of the maneuver and the covariance retrieval epoch are explained, and then the OCP to be solved is selected. Subsequently, the algorithms to generate the initial guess and perform the "major iterations" are outlined. Finally, the whole algorithmic flow is presented.

1. Probability Requirement and Covariance Retrieval Epoch

Since the target PoC for the maneuver and the covariance retrieval epoch are key factors in defining a CAM, these parameters are varied in the two cases. The target PoC corresponds to the final value of collision probability, at the TCA, after the CAM is executed. The covariance retrieval epoch is varied to simulate different scenarios when CDMs are issued. As a matter of fact, in real-life applications, there is a time gap between the reception of a CDM and the actual execution of a maneuver. CDMs are often issued several days before the TCA, allowing earlier maneuver decisions. Additionally, satellite operators require some reaction and decision time before commanding a maneuver [7].

In the "ideal" optimization case, the target of the maneuver, in terms of PoC, is set at 10^{-4}, which is the usual value employed by satellite operators to assess the risk posed by a conjunction [5, 9]. In Reference [28], the effect of the lead time, which is the interval between the maneuver start epoch and the TCA, is investigated. To do so, the covariance matrix, for the debris object, is assumed to be obtained exactly at the maneuver start epoch. The same approach is employed in the "ideal" case: this case is referred to as "ideal" since the decision time, between CDM reception and maneuver command, is brought to zero.

In the "real" case, the target, in terms of PoC, is set at 10^{-6}, since most CAMs target this value to rule out the collision risk [5]: it is known that satellite operators often wish to bring the collision probability below the threshold value (10^{-4}) by one or more orders of magnitudes [7]. This case is referred to as "real" due to its more realistic modeling of covariance retrieval. To simulate the interval between CDM reception and maneuver execution, a buffer time is introduced. Its value is set at 24 hours, since one day is regarded as the upper threshold to decide whether to maneuver or not [8]. The "real" case is created to address the following question: which is the upper bound for the minimum maneuver time, from the "ideal" optimization case, if more realistic position uncertainties and probability requirements are accounted for?

Both algorithms require the optimization to be performed if the value of the collision probability exceeds the threshold of 10^{-4} three days before the TCA [50].

2. Optimization Purpose

In Subsection IV.B, two feasible options for the objective function were provided, leading to the definition of OCPs 25 and 26. Running the algorithm on a number of test cases highlighted that the optimization whose objective is to find the maximum separation is much faster than that whose objective is the minimum PoC: solving OCP 25 can be up

to twenty times faster than solving OCP 26. It is thus important to select the best approach, in terms of the objective function, for each optimization case, considering limited resources concerning computational power and time.

In the "ideal" case, the objective is the minimum PoC: the minimum required time will be such that the minimum collision probability, for the specific maneuver time, cannot be brought below the threshold. To save computational time, however, the optimization is carried out by initially optimizing for maximum separation (solving OCP 25). Afterwards, the PoC value at the TCA is checked:

- If the PoC for the maximum separation is below the threshold, it is guaranteed that also the PoC for the minimum-collision-probability optimization will fall below the threshold, by definition of minimum PoC.
- If the PoC for the maximum separation is above the threshold, there is no theoretical guarantee that also the PoC for the minimum-collision-probability optimization will be above the threshold. The optimization needs to be performed again, by solving OCP 26, searching for the minimum PoC.

This completes one "major iteration" of the optimization process for the "ideal" case.

In the "real" case, at every "major iteration", the optimization is only carried out for maximum distance (solving OCP 25), for simplicity. Since the "real" optimization case aims to determine an upper bound for the maneuver time, a slightly shorter actual maneuver time is not considered problematic.

3. Guess Generation

As GPOPS-II makes use of a direct collocation method, an initial guess of the solution needs to be provided [60]. The initial guess should reflect a control law that can bring the probability of collision below a certain threshold.

As an initial guess, one could think of maximizing the rate of change of a Keplerian element in a given time interval. Expressions for the so-called locally optimal steering laws, to maximize the rate of change of each of the orbital elements, are available in the literature [61, 62]. Since circular orbits are considered, the argument of perigee is neglected, and only the control laws to maximize the rate of change of the Semi-Major Axis (SMA), eccentricity, inclination, and RAAN are investigated.

The most suitable control law, to decrease the PoC, is sought. To do so, for a given control law and parameter combinations, Algorithm 2 is employed. Firstly, the closest approach is built, for the set of sail, debris, and conjunction parameters under analysis. Then, a forward-backward propagation is performed, following Algorithm 3. The sailcraft is propagated backward by a quarter of its orbital period ($P_{S/C}$), starting from the defined state at the TCA. A quarter of the orbital period is chosen by comparison with the duration of optimized low-thrust CAMs [21–23, 28, 29]. In the backward propagation, the sail is oriented so that no SRP acceleration is produced. This is followed by a forward propagation, starting from the newly obtained state, until the TCA, with the sailcraft following the locally optimal control law. The PoC is recomputed for the final state at the TCA, applying Algorithm 1 to retrieve uncertainties, assuming the covariance is obtained at the maneuver start epoch. If the PoC falls below the threshold, the algorithm

stops; otherwise, the algorithm increases the propagation time, by a quarter of the orbital period, until convergence.

Algorithm 2 Initial guess generation for a given steering law

Require: Design parameters to define conjunction, locally optimal steering law, TCA
Compute: Sail and debris states at TCA
$N = 1$
while PoC $\geq 10^{-4}$ **do**
    Generate: Trajectory for the given $t_{MAN} = \text{TCA} - N \cdot 0.25 \cdot P_{S/C}$ through Algorithm 3
    Compute: Debris position covariance matrix through Algorithm 1 for $\zeta = \text{TCA} - t_{MAN}$
    Evaluate: Collision probability at TCA
    if PoC $< 10^{-4}$ **then**
        Store results
        Break
    else
        $N \leftarrow N + 1$
    end if
end while
Ensure: Time, state, and control history such that PoC $< 10^{-4}$

Algorithm 3 Initial guess propagation for a given steering law

Require: Design parameters to define conjunction, locally optimal steering law, TCA, t_{MAN}
Compute: Sail state at TCA
Propagate: backward from TCA (without SRP) until t_{MAN}
Propagate: forward (until TCA) applying the locally optimal control law
Ensure: Time, state, and control history

Once results are generated for all the control laws under analysis, the locally optimal steering law that yields the shortest maneuver time is selected (in case of the same time being required by two or more control laws, the minimum value of PoC at the TCA is sought). The selected control law is regarded as the "best" locally optimal steering law.

For both optimization cases, at every "major iteration", a guess is generated: the result from the previous "major iteration" cannot be used as an initial guess, as the time horizon changes throughout "major iterations". For a given maneuver start epoch, the "best" locally optimal steering law is employed to generate the initial guess, in terms of time, state, and control history, through Algorithm 3. From the initial position and velocity, the scaling parameters are fed to the optimizer. Moreover, based on the given maneuver start epoch, the debris position covariance matrix is generated (through Algorithm 1). For the "ideal" case, the guess for the maneuver time, for the first "major iteration", is found through Algorithm 2. For the "real" case, instead, the maneuver time, for the first "major iteration", is initialized through the solution of the "ideal" optimization, which is carried out in advance.

4. Time-Iterating Scheme

As explained in Subsection IV.A, subsequent fixed-time-horizon optimizations are performed, to iteratively find the optimal maneuver time.

In the "ideal" optimization case, the chosen scheme to carry out the "major iterations" is the bisection method,

due to its proven efficiency. The scheme stops when two subsequent values of maneuver time differ by less than one minute. The longer the maneuver time of the first "major iteration", the more bisections are needed to reach the desired accuracy: the maximum number of "major iterations" is thus a function of the initial guess for the maneuver time, $N_{max} = g(\Delta t_{guess})$.

A generic "major iteration" of the bisection method can be summarized as follows:

- The input maneuver start epochs are t_1 and t_2, with $t_1 < t_2$ (for the first "major iteration", t_1 is the initial epoch of the guess and t_2 is represented by the closest approach epoch);
- The optimization is performed with $t_3 = \frac{t_1+t_2}{2}$ ($t_1 < t_3 < t_2$);
- The PoC is computed after optimizing for t_3, and the next "major iteration" is setup:
  - If the PoC is below the threshold, the maneuver time is decreased, and the lower bound of the maneuver start epoch is increased: the inputs for the next "major iteration" are t_3 and t_2 (with $t_3 < t_2$);
  - If the PoC is above the threshold, the maneuver time is increased, and the upper bound of the maneuver start epoch is decreased: the inputs for the next "major iteration" are t_1 and t_3 (with $t_1 < t_3$).

Decreasing the maneuver time means increasing the lower bound of the maneuver start epoch, moving it forward, toward the TCA (by definition, the maneuver start epoch precedes the TCA).

In the "real" case, "major iterations" proceed augmenting the maneuver time by 50%, for simplicity, and the upper limit for the maneuver start epoch is set one day before the TCA (the maneuver execution decision threshold [8]).

5. Algorithmic Flow

The execution flows, for the "ideal" and "real" optimization cases, are presented in Algorithms 4 and 5, respectively. Table 7 summarizes the key differences between the two optimization cases.

In the "ideal" optimization (Algorithm 4), for a generic set of design parameters, the "best" locally optimal control law and the initial guess for the maneuver time from Algorithm 2 (Δt_{guess}) are retrieved. The debris covariance is obtained through Algorithm 1, at the maneuver start epoch. Then, the optimization is carried out, first solving OCP 25, and, only if the PoC value is above the threshold, solving OCP 26. Once the optimal solution is outputted, the PoC is recomputed, and, based on its value, the maneuver time is either decreased or increased, through bisection. This completes one "major iteration" of the optimization process. For every new "major iteration", the initial guess is computed by applying the "best" locally optimal steering law for the updated maneuver start epoch (through Algorithm 3). Once "major iterations" stop, when the desired one-minute accuracy is reached, results are outputted.

In the "real" optimization (Algorithm 5), for a generic set of design parameters, the "best" locally optimal control law is retrieved, along with the optimal solution for the "ideal" case: the guess for the maneuver time, to be fed to the optimizer for the first "major iteration", comes indeed from the "ideal" optimization case (Δt_{opt}). The debris covariance is obtained through Algorithm 1, one day before the maneuver start epoch. The optimization is carried out, solving OCP

Algorithm 4 Optimization flow to find the minimum-time collision avoidance maneuver ("ideal" case)

Require: Design parameters to define conjunction, GPOPS-II settings, TCA, Δt_{guess} (from Algorithm 2), "best" locally optimal control law

Compute: Sail and debris states at TCA
$\Delta t_{old} = \Delta t_{guess}$
$N = 1$
$N_{max} = g(\Delta t_{guess})$
while $N < N_{max}$ **do**
    Set up: Optimization problem (from settings in Table 6)
    Generate: Initial guess through Algorithm 3 applying the "best" control law for t_{MAN} = TCA − Δt_{old}
    Optimize: Maximum separation (solving OCP 25 to minimize Eq. 15)
    Compute: Debris position covariance matrix through Algorithm 1 for ζ = TCA − t_{MAN}
    Evaluate: Collision probability at TCA
    if PoC < 10^{-4} **then**
        Perform: Bisection method iteration, decreasing maneuver time, to find Δt_{new}
    else
        Optimize: Minimum collision probability (solving OCP 26 to minimize Eq. 17)
        Compute: Debris position covariance matrix through Algorithm 1 for ζ = TCA − t_{MAN}
        Evaluate: Collision probability at TCA
        if PoC < 10^{-4} **then**
            Perform: Bisection method iteration, decreasing maneuver time, to find Δt_{new}
        else
            Perform: Bisection method iteration, increasing maneuver time, to find Δt_{new}
        end if
    end if
    $\Delta t_{old} \leftarrow \Delta t_{new}$
    $N \leftarrow N + 1$
end while

Ensure: Time, state, and control history of the optimal solution (for the minimum-time CAM)

25. Once the optimal solution is outputted, the PoC is computed, and, based on its value, either the algorithm is stopped (if the probability complies with the requirement) or the maneuver time is increased by 50%, until convergence. For every new "major iteration", the initial guess is computed by applying the "best" locally optimal steering law for the updated maneuver start epoch (through Algorithm 3).

Table 7 Overview of the differences between the "ideal" and "real" optimization cases

Parameter	"Ideal" case	"Real" case
Target PoC	10^{-4}	10^{-6}
Covariance retrieval epoch (simulated CDM issue)	t_{MAN}	t_{MAN} - 24 hours
Objective	Minimum PoC	Maximum separation
Initial guess for first "major iteration"	"Best" locally optimal steering law	Optimal solution of the "ideal" case
Time-iterating scheme	Bisection method	Maneuver time is augmented by 50%

Algorithm 5 Optimization flow to find the minimum-time collision avoidance maneuver ("real" case)

Require: Design parameters to define conjunction, GPOPS-II settings, TCA, Δt_{opt} (from Algorithm 4), "best" locally optimal control law

Compute: Sail and debris states at TCA
$\Delta t_{old} = \Delta t_{opt}$
while $\Delta t < 1$ day **do**
    Set up: Optimization problem (from settings in Table 6)
    Generate: Initial guess through Algorithm 3 applying the "best" control law for $t_{MAN} = \text{TCA} - \Delta t_{old}$
    Optimize: Maximum separation (solving OCP 25 to minimize Eq. 15)
    Compute: Debris position covariance matrix through Algorithm 1 for $\zeta = \text{TCA} - t_{MAN} - 24$ hours
    Evaluate: Collision probability at TCA
    if PoC $< 10^{-6}$ **then**
        Store results
        break
    else
        $\Delta t_{new} \leftarrow 1.5 \cdot \Delta t_{old}$
        $\Delta t_{old} \leftarrow \Delta t_{new}$
    end if
end while

Ensure: Time, state, and control history of the optimal solution (for the minimum-time CAM)

V. Results

This section presents the results: 71,526 scenarios were optimized, equally divided between the "ideal" and "real" cases. Firstly, the analysis of the maneuver time is carried out in Subsection V.A. Subsequently, the trends in the optimal control profile are investigated in Subsection V.B.

In analyzing both the maneuver time and the optimal control profile, characteristic quantities are presented for the "ideal" and the "real" cases. This is followed by a correlation analysis, to identify the influence of the design parameters (see Table 4) on the quantities under scrutiny. Based on the identified correlations, further analyses are carried out, showing data either through error bars (to provide the mean value and the standard deviation for a given quantity) or through tables. For tables that include a substantial amount of data, red and green colors are used to highlight values that stand out for being smaller and larger than the other observations, respectively.

V.A. Maneuver Time

The main objective of the research is to identify the minimum required time, before the closest approach, for a solar sail to execute a collision avoidance maneuver. The value of the maneuver time itself shall therefore be addressed in the first place: both for the "ideal" and "real" cases, results are plotted for the whole dataset, in the form of a histogram. Fig. 2 provides the maneuver time and the fraction of the sail period spent while maneuvering.

In the "ideal" case (Fig. 2a), the minimum required time usually lies between 10 and 40 minutes, and never exceeds one orbital period. The average time is 25 minutes, with a standard deviation of 16 minutes, whereas the maximum time is 104 minutes. The cluster toward a value of 0 minutes is given by conjunctions whose initial PoC is already very close

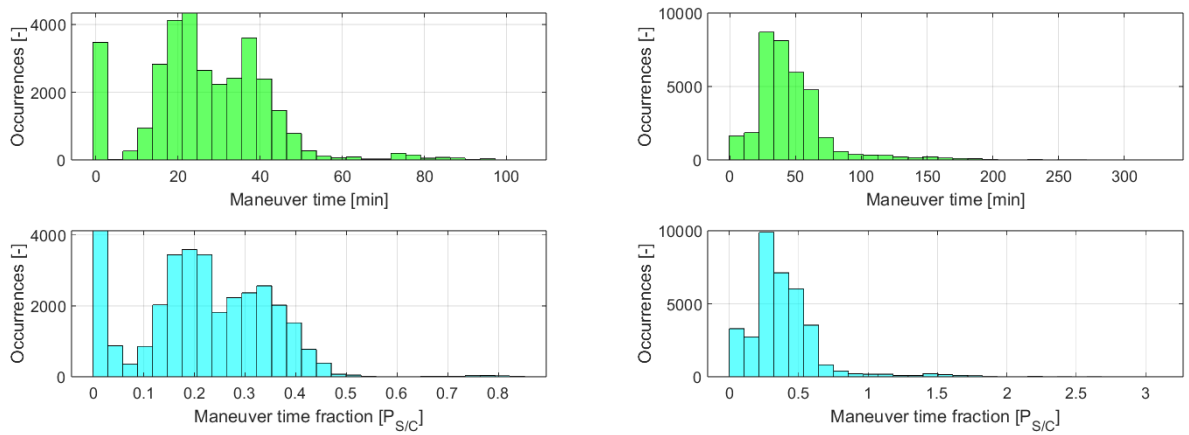

(a) "Ideal" case **(b) "Real" case**

Fig. 2 Maneuver time (top) and maneuver time as a fraction of the orbital period (bottom), for all optimized scenarios

to the threshold of 10^{-4}. On the other hand, in the "real" case (Fig. 2b), the maneuver time is intuitively longer, as the target PoC is lower and the maneuver is executed upon an earlier CDM (see Table 7): there is a worse knowledge of the debris state, resulting in greater uncertainty. The maneuver time is clustered between 30 and 60 minutes: the average value is 47 minutes, with a standard deviation of 29 minutes. The maximum time is 327 minutes (approximately 5.5 hours); however, almost all maneuvers (99.45% of the scenarios) last less than three hours and require no more than two orbital revolutions. It is therefore verified, for all scenarios, that the required time is well below the threshold of one day, regarded as the limit value to decide whether to execute a CAM, proving the feasibility of collision avoidance maneuvers for solar sails, considering the current operational framework.

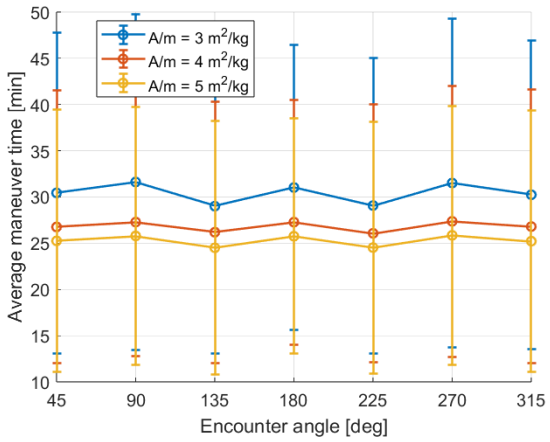

Fig. 3 Average maneuver time, as a function of the encounter angle

For all tried values of area-to-mass ratio ("A/m" in the graphs, for brevity), Fig. 3 highlights a symmetry: it shows the average maneuver time as a function of the encounter angle, between the sailcraft and debris velocities at the TCA (see Eq. 10). Conjunctions sharing the same azimuth angle (see Table 3) yield the same maneuver time. Equal azimuth angles imply equal angles between the relative velocity and the sailcraft (and debris) velocity. Therefore, the angle with respect to the encounter plane, perpendicular to the relative velocity, onto which the uncertainties are projected to compute the PoC, is also the same, explaining the symmetry.

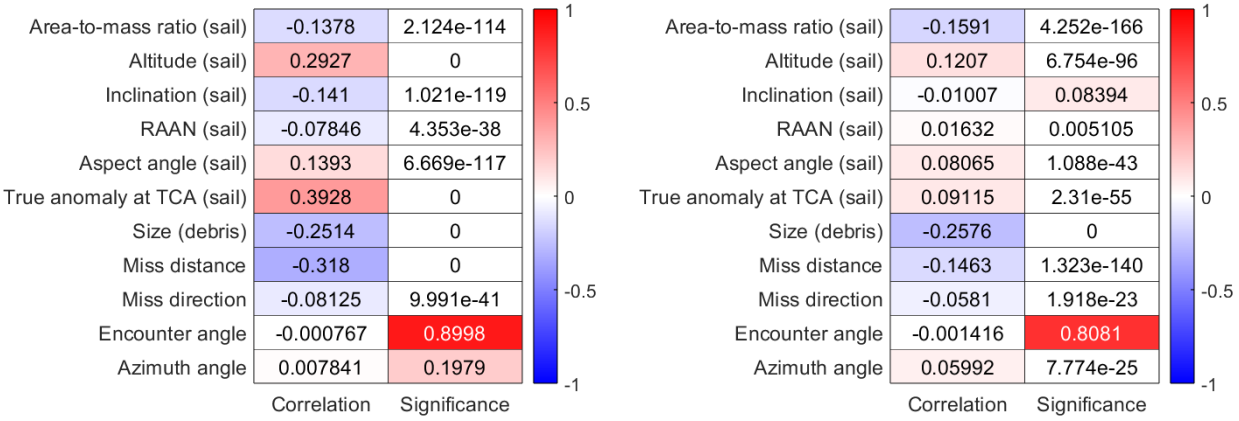

(a) β > 10 degrees - "Ideal" case

(b) β > 10 degrees - "Real" case

(c) $\beta \leq$ 10 degrees - "Ideal" case

(d) $\beta \leq$ 10 degrees - "Real" case

Fig. 4 Correlation and significance analysis to identify the influence of the design parameters on the maneuver time

A correlation and significance analysis is carried out, to identify the influence of the design parameters on the maneuver time, for both the "ideal" and "real" cases: the resulting matrices are shown in Fig. 4. Computations are performed separately for sail orbits with an aspect angle greater than 10 degrees (Figs. 4a, 4b), and with an aspect angle below 10 degrees (Figs. 4c, 4d). Parameters whose correlation coefficient has the greatest absolute value are sought (with positive values highlighting a positive correlation, and vice versa for negative values). Also, significance coefficients are presented, as only parameters with a significance coefficient (*p-value*) below 0.05 are considered statistically significant [63]. For $\beta > 10$ degrees, a positive correlation with the altitude is recognizable, hinting at longer maneuver times for the maneuvers in GEO. This is seen only in Figs. 4a and 4b, since only orbits in the equatorial GEO belt are simulated (see Table 4), with an aspect angle of 90 degrees (see Table 1). Plotting the average maneuver time as a function of the altitude (for the "ideal" case, since the trend is the same in both cases) shows that higher altitude implies longer maneuver time (Fig. 5a). Nevertheless, at higher altitudes, the sailcraft needs to steer for a much smaller fraction

of the orbit (Fig. 5b), and this could comply with stricter constraints on the orbital fraction allocated for the CAM.

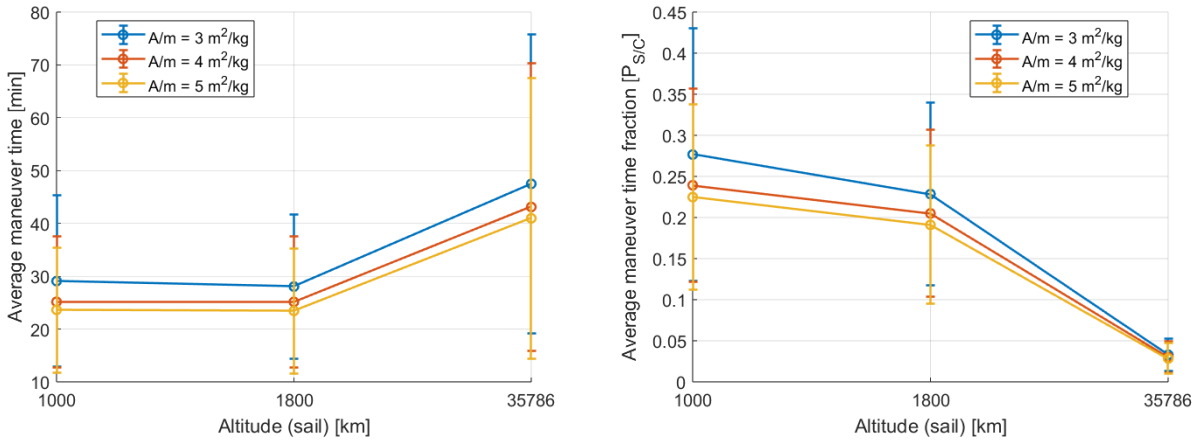

(a) Maneuver time **(b) Maneuver time fraction**

Fig. 5 Average maneuver time and average maneuver time as a fraction of the orbital period, as a function of the sail altitude

In Fig. 4, for all scenarios, factors with large correlation coefficients are the area-to-mass ratio, the debris size, and the miss distance. Intuitively, the correlation with the area-to-mass ratio is negative: a larger area-to-mass ratio results in a shorter maneuver time, as the sail has greater control authority. Regarding debris size and miss distance, their impact on maneuver time underscores the relationship between maneuver time and collision probability. Specifically, maneuver time increases for smaller miss distances, which correspond to greater PoC values (as the RSOs are closer), and for smaller debris objects. This is because smaller objects are tracked with a more substantial degree of uncertainty [43], leading to an increase in the PoC and, consequently, a longer maneuver time.

A large correlation coefficient between the maneuver time and the true anomaly of the sail at the TCA is observed in Fig. 4a, whereas no clear dependence is registered in Figs. 4b, 4c, and 4d. This can be explained by considering where the sailcraft is located, at the closest approach, in the various cases. For an aspect angle greater than 10 degrees, simulations reflect the occurrence of eclipses along the orbit (see Table 4): when in shadow, the sail is unable to maneuver for a certain amount of time, thus requiring longer maneuver times. Figure 6a depicts the average maneuver time as a function of the encounter location, in LEO, for the "ideal" case: especially for close encounters happening at the end of the eclipse region, the whole arc of the orbit in shadow is added to the "actual" maneuver time. The same happens when the sailcraft is in GEO, since such an orbital regime is subject to eclipses during equinoxes, as shown, for the "ideal" and "real" cases, in Figs. 6c and 6d, respectively. In the "real" case, only Fig. 6d, presenting the results in GEO, shows that close approaches taking place in eclipse result in longer maneuver times. The reason why Fig. 6b, corresponding to the LEO region, does not show such a trend can be found in the longer maneuver times required by the "real" case: if the maneuver lasts for a larger fraction of the orbit, up to a full revolution, eclipsing events affect all

four encounter locations. As a matter of fact, in the "ideal" case, maneuvers always last less than one orbit (Fig. 2a), whereas, in the "real" case, maneuvers can take as much as two revolutions (Fig. 2b). In GEO this is not an issue, as the orbital period is 24 hours, and no maneuver, in the "real" case, lasts this long (Fig. 2b). On the other hand, no eclipse occurs for the orbits whose aspect angle is below 10 degrees: indeed, no recognizable trends, between the maneuver time and the sail true anomaly at the TCA, are identified in Figs. 4c and 4d.

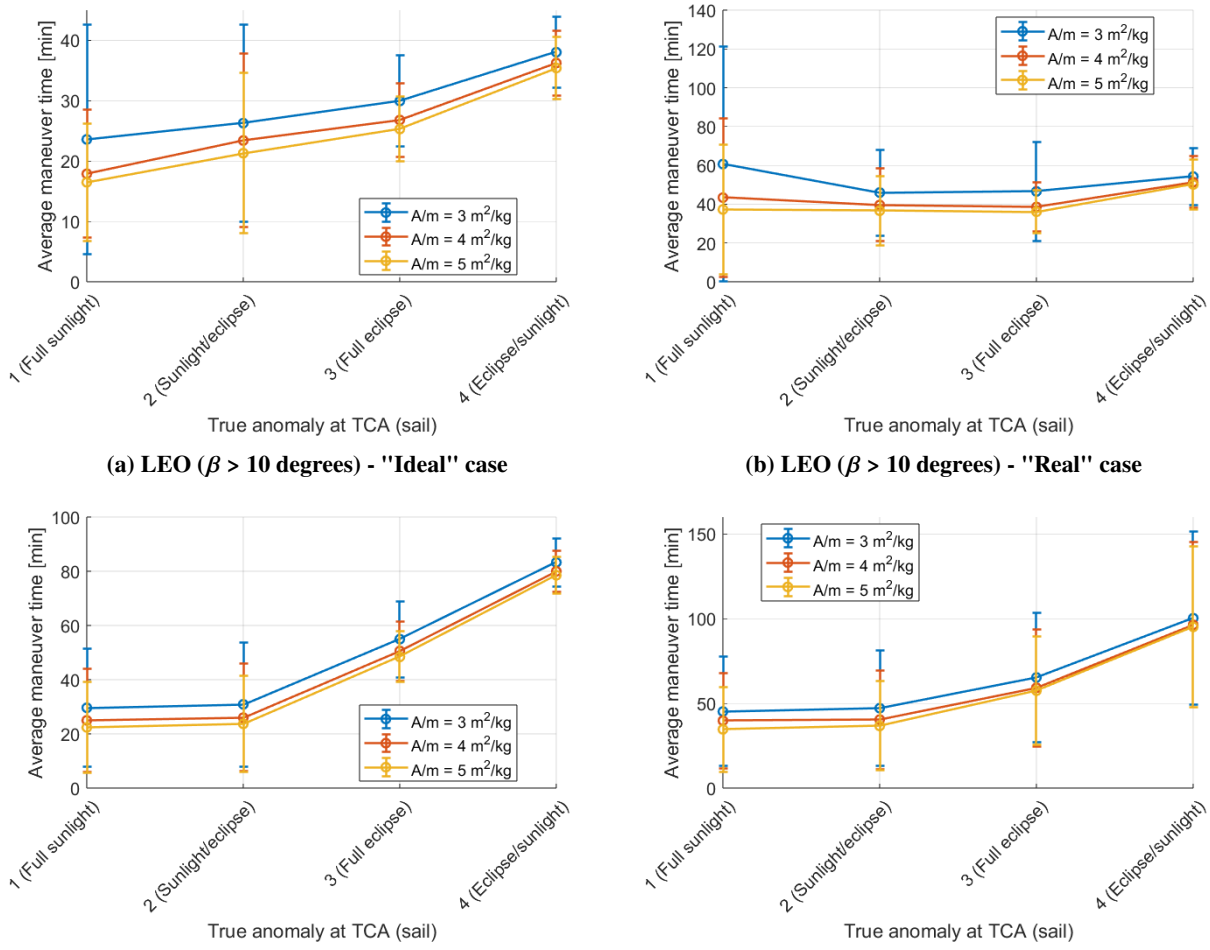

(a) LEO (β > 10 degrees) - "Ideal" case

(b) LEO (β > 10 degrees) - "Real" case

(c) GEO (β > 10 degrees) - "Ideal" case

(d) GEO (β > 10 degrees) - "Real" case

Fig. 6 Average maneuver time, as a function of the encounter location along the sail orbit

Figure 4d shows positive correlation coefficients for the sail inclination, RAAN, and aspect angle, in the "real" case, hinting at a correlation between maneuver time and sail orbit orientation, whereas no significant tendency is observed in the "ideal" case (Fig. 4c). Figure 7 presents the average maneuver time as a function of the inclination, for an altitude of 1000 km, in the "real" case: SSOs (retrograde orbits with an inclination of 99.5 degrees) require a longer maneuver time, on average. Table 8 offers another insight, presenting the average maneuver time as a function of the aspect angle, distinguishing between Sun-synchronous and non-Sun-synchronous orbits, at an altitude of 1000 km: variations are not

large, and only weak correlations can be identified, as larger aspect angles tend to yield a slightly longer maneuver time. Therefore, the maneuver time is independent of the Earth-Sun configuration (i.e., the time of the year).

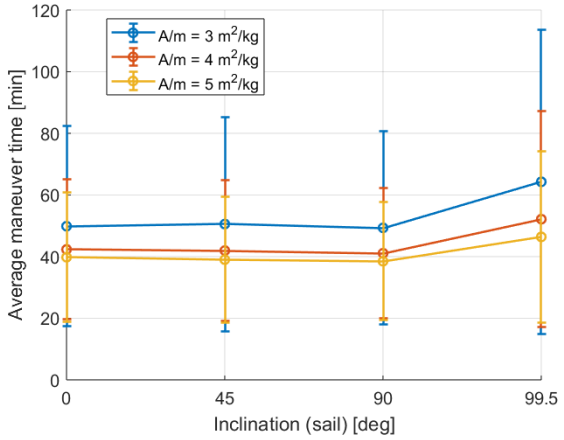

Fig. 7 Average maneuver time, as a function of the sail inclination, for an altitude of 1000 km, in the "real" case

Table 8 Average maneuver time, as a function of the sail orbital regime and aspect angle, for an altitude of 1000 km

Orbital regime (sail)	Aspect angle (sail)	Average maneuver time [min]	
		"Ideal" case	"Real" case
SSO	10	28.81	54.44
	45	28.35	53.80
	90	30.18	55.30
Not SSO	0	28.07	48.36
	45	27.92	48.78
	60	29.66	49.49
	90	29.97	49.02

Analyzing the interactions between parameters highlighted the cross-influence of the encounter location and the miss direction. As a matter of fact, in the simulations, the debris can be displaced along the positive radial ($\hat{\mathbf{x}}_O$), transverse ($\hat{\mathbf{y}}_O$), or normal ($\hat{\mathbf{z}}_O$) directions, in the RTN frame of the sailcraft (see Table 4). The orientation of such directions with respect to the sunlight changes as the spacecraft moves along the orbit. Due to the thrust generating principle of solar sails, the acceleration cannot be directed toward the Sun [11], and thus cannot be aligned with a specific basis vector of the frame $O(\hat{\mathbf{x}}_O, \hat{\mathbf{y}}_O, \hat{\mathbf{z}}_O)$ for some configurations.

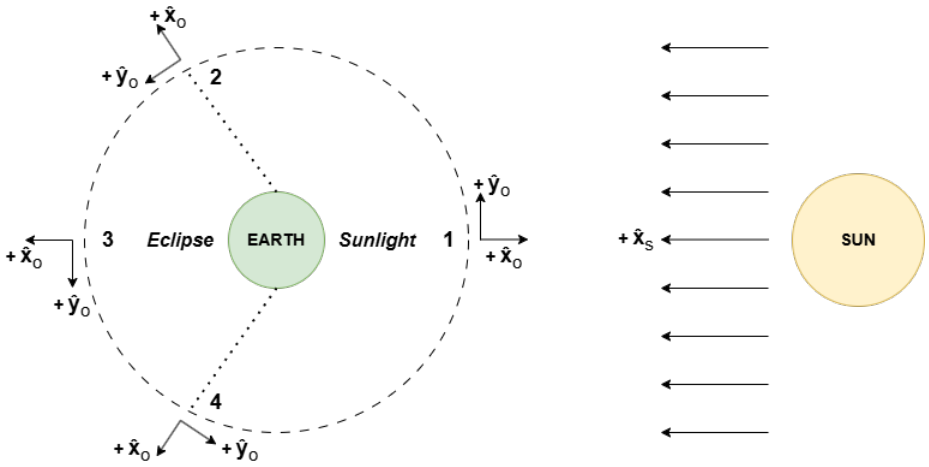

Fig. 8 Visualization of the four encounter locations along the sail orbit, for an equatorial orbit in LEO, with β = 90 degrees

The scenario corresponding to an aspect angle of 90 degrees is analyzed. In Fig. 8, an equatorial orbit, with an

aspect angle of 90 degrees, is depicted (for the correspondence between numbers, in Fig. 8, and sail true anomalies at the TCA, refer to Table 4). The sunlight direction lies in the orbital plane $(\hat{\mathbf{x}}_O, \hat{\mathbf{y}}_O)$. At the encounter location "1", the thrust will never be directed in the positive $\hat{\mathbf{x}}_O$ direction; vice versa, for the encounter location "2", the thrust will never be directed in the negative $\hat{\mathbf{x}}_O$ direction. Likewise, for the encounter location "3", the thrust will never be directed in the negative $\hat{\mathbf{y}}_O$ direction. Table 9 presents the average maneuver time for different combinations of encounter locations and miss directions, in LEO and GEO. Only results for the "ideal" case are shown, as the same trends are observed in the "real case. In LEO, it can be verified how the aforementioned considerations translate to variations in the maneuver time. What is displayed is that the maneuver time increases if the debris is displaced along the positive sunlight direction, as the sail will tend to move toward the object rather than escape from it. For the GEO region, results for encounter locations "2", "3", and "4" all seem to show a longer maneuver time if the debris is shifted along the positive $\hat{\mathbf{x}}_O$ direction. The reason is that, in GEO, the true anomalies corresponding to the entry (location "2") and exit (location "4") positions of the eclipsing arc are much closer to each other (and closer to encounter location "3", in Fig. 8), if compared to the LEO case. The fraction of the orbit spent in eclipse, in GEO, is only around 5% [37]. For the encounter locations "2", "3", and "4", the thrust will thus never be directed in the negative $\hat{\mathbf{x}}_O$ direction. This means the sailcraft will tend to move toward the debris if it is located along the positive $\hat{\mathbf{x}}_O$ direction, requiring a longer time to maneuver.

Table 9 Average maneuver time, as a function of the encounter location along the sail orbit and the miss directions, in LEO and GEO

True anomaly at TCA (sail)	Miss direction	Average maneuver time [min]	
		LEO	GEO
1 - Full sunlight	$\hat{\mathbf{x}}_O$	20.56	27.66
	$\hat{\mathbf{y}}_O$	23.70	33.01
	$\hat{\mathbf{z}}_O$	23.30	32.56
2 - Sunlight/eclipse	$\hat{\mathbf{x}}_O$	28.38	39.37
	$\hat{\mathbf{y}}_O$	30.45	33.05
	$\hat{\mathbf{z}}_O$	28.40	32.05
3 - Full shadow	$\hat{\mathbf{x}}_O$	29.04	54.30
	$\hat{\mathbf{y}}_O$	27.45	49.72
	$\hat{\mathbf{z}}_O$	27.74	49.58
4 - Eclipse/sunlight	$\hat{\mathbf{x}}_O$	40.08	82.53
	$\hat{\mathbf{y}}_O$	39.47	79.12
	$\hat{\mathbf{z}}_O$	39.70	79.98

V.B. Optimal Control Profile

To examine the results in terms of the direction of the control vector, the temporal evolution of the optimal control profile is averaged, for each component along the basis vectors of the sunlight reference frame $S(\hat{\mathbf{x}}_S, \hat{\mathbf{y}}_S, \hat{\mathbf{z}}_S)$. The

averaging process includes only the control values corresponding to the spacecraft being in sunlight, as the control is negligible during eclipses. In Fig. 9, a histogram representing the number of occurrences of the values assumed by the average components of the optimal control vector, in the sunlight frame, is presented. Both in the "ideal" and "real" cases, for the acceleration along $\hat{\mathbf{x}}_S$ (aligned with the incoming solar radiation), a cluster can be identified close to unity. This means the acceleration generally tends to align itself with the direction of sunlight to perform the CAM.

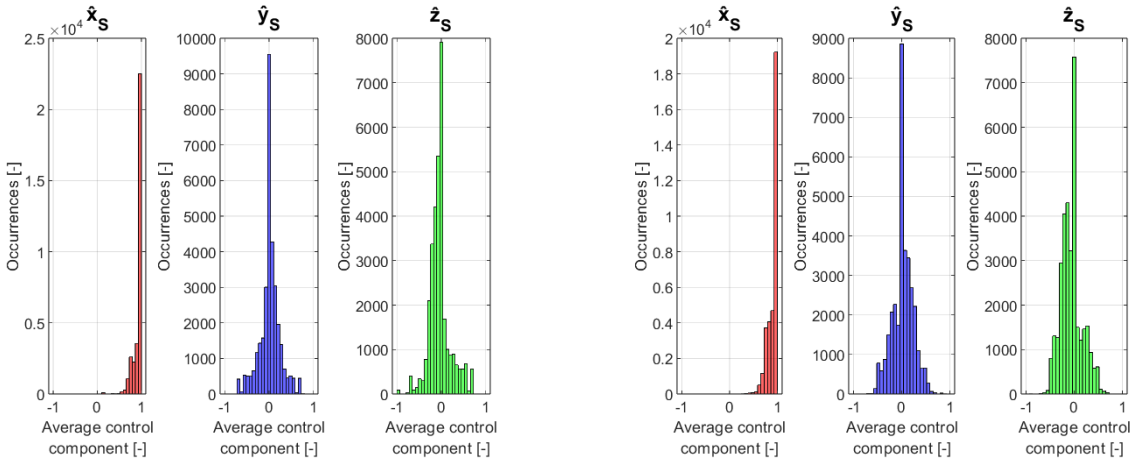

(a) "Ideal" case **(b) "Real" case**

Fig. 9 Average components of the optimal control profile, in the sunlight frame, for all optimized scenarios

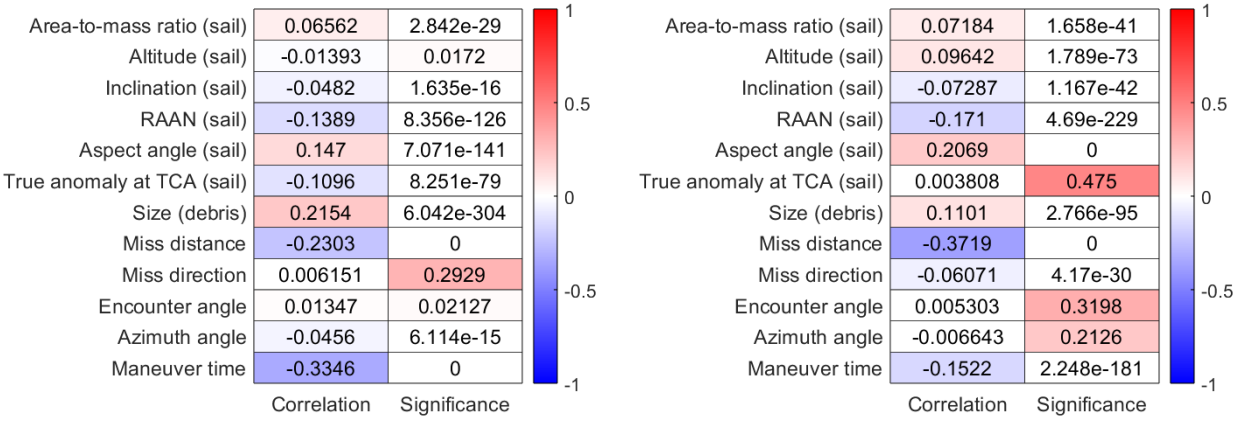

(a) "Ideal" case **(b) "Real" case**

Fig. 10 Correlation and significance analysis to identify the influence of the design parameters on the average component of the control vector in the sunlight direction

In Fig. 10, the results of a correlation and significance analysis are shown, to identify the influence of the design parameters on the average component of the control vector in the sunlight direction, along $\hat{\mathbf{x}}_S$. In addition to the parameters already included in Fig. 4, also the maneuver time is added. In both the "ideal" and "real" cases, correlation coefficients with the largest absolute values are sought (as explained in the previous subsection). Parameters with large

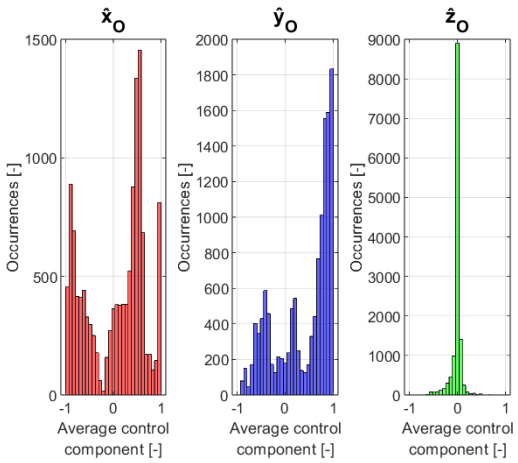

(a) β = 90 degrees

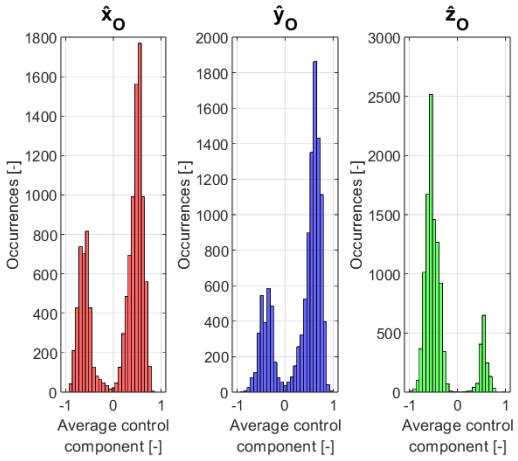

(b) 45 degrees $\leq \beta \leq$ 60 degrees

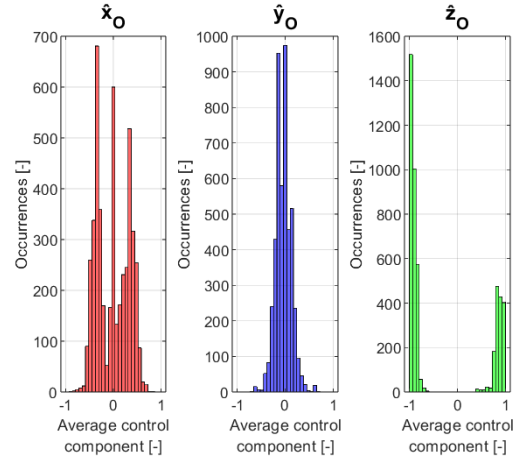

(c) $\beta \leq$ 10 degrees

Fig. 11 Average components of the optimal control profile, in the RTN frame of the sail, for different sail aspect angles

correlation coefficients are the debris size, the miss distance, and the maneuver time. A negative correlation with maneuver time highlights that the average thrust component in the sunlight direction tends to grow with shorter maneuver time. Maneuver time thus benefits from thrusting in the direction of sunlight. This is confirmed by a positive correlation with the debris size, since shorter maneuver times are found for bigger debris sizes (Fig. 4). However, a negative correlation is found for the miss distance: all other parameters being equal, a smaller miss distance requires the control to be directed predominantly along the sunline vector, compared to less threatening conjunctions corresponding to larger miss distances. No strong correlation is found with the area-to-mass ratio nor the altitude: regardless of the sail control authority and distance from the Earth's surface, the optimal control profile shows similar trends. Finally, by looking at the large correlation coefficients registered for the aspect angle, as well as for the RAAN, it is clear that the optimal control profile is affected by the orbit orientation with respect to the Sun.

To investigate the thrust orientation, the average control components are plotted in the RTN frame of the sailcraft, for the "ideal" case without loss of generality. For the whole dataset, histograms are shown in Fig. 11, dividing the results based on the value of the aspect angle of the sailcraft orbit. For an aspect angle of 90 degrees (Fig. 11a), the sunlight direction lies in the orbital plane, and the thrust is also only directed in the orbital plane ($\hat{\mathbf{x}}_O$, $\hat{\mathbf{y}}_O$), while the out-of-plane component, along $\hat{\mathbf{z}}_O$, is zeroed out. For an aspect angle between 45 and 60 degrees (Fig. 11b), the sunlight direction has a component outside of the orbital plane: indeed, the acceleration still acts in the orbital plane, but the control acting in the out-of-plane direction is also not negligible. Finally, for the lowest aspect angles (Fig. 11c),

corresponding to an orbital plane perpendicular to the incoming sunlight, the component along $\hat{\mathbf{z}}_O$ is predominant. Nevertheless, there is also a component of the control in the orbital plane, mostly in the radial direction $\hat{\mathbf{x}}_O$, whereas the average thrust component along $\hat{\mathbf{y}}_O$ (parallel to the velocity) is clustered around zero. The analysis of the average control components, in the RTN frame of the sailcraft, thus concludes that the projection of the control vector onto the orbital plane is non-zero in all scenarios. In-plane maneuvering is therefore unavoidable in executing the CAM.

The orientation of the control within the orbital plane can be inferred by evaluating the average yaw angle throughout the maneuver, as a function of the true anomaly of the sail at the TCA, shown in Fig. 12 (for the "ideal" case, since the same considerations apply also to the "real" case). The yaw angle is defined as the angle between the projection of the control onto the orbital plane and the velocity vector. Figure 12a (for the largest aspect angles) highlights that, only for one encounter location, the acceleration tends to orient itself against the velocity (with the yaw angle being greater than 90 degrees), and, vice versa, is concordant with the velocity in the other three scenarios. The reason is found in Fig. 8: for encounter location "1", the final thrusting arc goes from the shadow-to-sun transition point (location "4") up to the closest approach point, in full sunlight. The solar sail acceleration can thus never be directed toward the positive $\hat{\mathbf{y}}_O$ direction, oriented as the velocity, explaining a yaw angle greater than 90 degrees. On the other hand, Fig. 12b shows no particular relation between the yaw angle and the encounter location, for the orbits not experiencing eclipsing events, corresponding to the lowest aspect angles. For all encounter locations, the average yaw angle encompasses 90 degrees, implying angles between the projected control and the orbital velocity close to a right angle: the average component of the acceleration along $\hat{\mathbf{y}}_O$ is indeed close to zero, as highlighted in Fig. 11c.

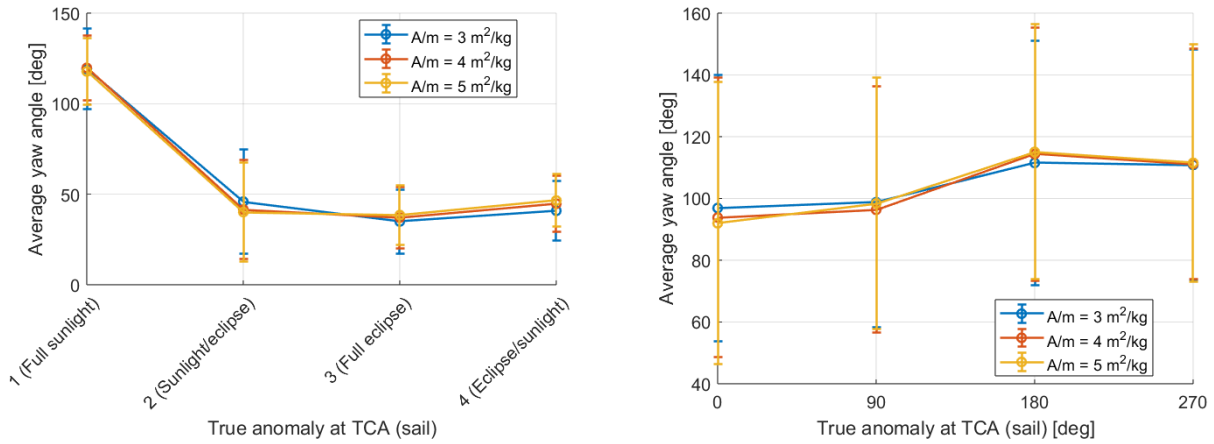

(a) β > 10 degrees **(b) $\beta \leq$ 10 degrees**

Fig. 12 Average yaw angle, as a function of the encounter location along the sail orbit

After identifying the main factors that govern the optimal control profile direction, potential relationships between the GPOPS-II control solution and the locally optimal steering laws are examined. The laws to maximize the rate of change of the SMA, eccentricity, inclination, and RAAN are applied to all scenarios, for a duration equal to the optimized maneuver

time. Since the PoC value at the TCA depends on the final state at the closest approach (as explained in Subsection III.B) and not on the state evolution, the control law considered the "closest" to the optimal solution is the one whose final state has the smallest difference compared to the optimized final state. It is also verified that the "closest" control law, among the tried ones, is the one that reduces the PoC the most. In 85.96% of scenarios in the "ideal" case and 91.65% in the "real" case, the steering laws that best approximate the optimal CAMs are those that modify either the SMA or the eccentricity. These laws require in-plane acceleration [64], confirming that in-plane maneuvering is generally unavoidable in the optimized CAMs.

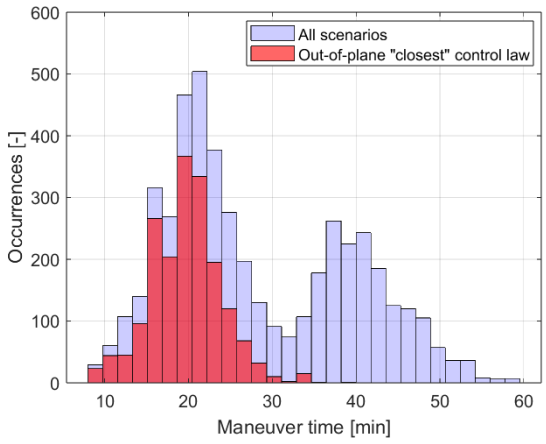

Fig. 13 Scenarios, in terms of maneuver time, for which the "closest" steering law acts fully outside the orbital plane (for $\beta \leq 10$ degrees)

However, for aspect angles below 10 degrees, the percentage of CAMs approximated by the laws changing SMA or eccentricity drops to 61.51% in the "ideal" case and 88.83% in the "real" case. A greater number of maneuvers align with "out-of-plane" steering laws, affecting inclination and RAAN, when the thrust has a component outside the orbital plane (Fig. 11c) [35]. This trend is evident for the shortest maneuver times, as illustrated in Fig. 13, which shows, for the "ideal" case, the scenarios best approximated by fully "out-of-plane" steering laws, to modify either inclination or RAAN. This suggests that, for longer maneuver durations, solar sails are more effective in changing SMA and eccentricity than in modifying inclination and RAAN, for low aspect angles. This also explains why, despite the sunlight being fully directed outward from the orbital plane, Fig. 11c still shows a non-zero control component within the orbital plane.

Moreover, the PoC (at the TCA) for the final state propagated through the "closest" control law, in the "ideal" case, falls below the required value in 29% of the scenarios. The PoC outputted by GPOPS-II is the minimum (since, in the "ideal" case, OCP 26 is solved, minimizing the PoC); however, in some cases, the minimum PoC found by GPOPS-II is smaller than the threshold of 10^{-4} (e.g., 10^{-5} is outputted), leaving room for the locally optimal laws to satisfy the requirement still. For scenarios that are uncompliant with the PoC requirement at the TCA, applying the locally optimal laws can be successful only if the maneuver time is increased. In the "real" case, characterized by longer maneuver times, in 95% of the scenarios, the PoC, computed at the TCA after propagating the state through the "closest" steering law, is below the threshold. Therefore, especially if mission constraints allow longer maneuver times, solar-sail collision avoidance maneuver planning could be streamlined, by only considering these straightforward locally optimal control laws.

VI. Conclusions

Envisioning potential applications of solar sails around Earth, this paper has characterized their performance in executing collision avoidance maneuvers, seeking the minimum maneuver time required to reduce the probability of collision below a threshold. The dynamical model includes Earth's central gravity, its J2 term, and the solar radiation pressure acceleration. An extensive set of conjunction scenarios is simulated (e.g., by varying orbital regimes, sail control authorities, and collision geometries), for an "ideal" and a "real" case, the latter accounting for greater position uncertainties and stricter probability requirements. A covariance-mapping algorithm is used to model uncertainties. The optimal control problem is derived and solved via direct collocation, seeking time-optimal maneuvers while constraining the collision probability.

For all simulated scenarios, the maneuver time is well below one day, fitting the current operational framework. In the "ideal" case, where the warning is issued later, at the start of the maneuver, the maneuver lasts less than one orbital revolution. In the "real" case, the maneuver time is longer, but no more than two orbital periods are generally required. A relation between collision probability and maneuver time is identified, through the parameters that define the debris state and position uncertainty. The better the knowledge of the debris state, the shorter the maneuver time. A negative correlation, for the maneuver time, is found with the control authority of the sail, and a positive one with the altitude. Solar-sail-specific effects are highlighted. First, eclipses cause an increase in the maneuver time, since sails cannot be maneuvered when in shadow. Second, if the debris is displaced along the sunlight direction, the sailcraft will tend to move toward (rather than escape from) the object, yielding longer maneuver times. The orbit orientation mainly affects the optimal control profile but does not significantly impact the maneuver time, which is thus independent of the Earth-Sun configuration. In terms of the optimal thrusting profile, it is found that the sail largely thrusts along the direction of sunlight and that there is always an in-plane control component. The locally optimal steering laws that better approximate the final state of the sailcraft (obtained by the optimized maneuvers) are those to change either the semi-major axis or the eccentricity, which indeed require in-plane maneuvering. Especially for longer maneuver times, these straightforward control laws comply with the requirement of the collision probability at the closest approach: this could streamline solar-sail collision avoidance maneuver planning.

References

[1] Byers, M., & Boley, A. (2023). *Who owns outer space?: International law, astrophysics, and the sustainable development of space* (1st ed.). Cambridge University Press. https://doi.org/10.1017/9781108597135

[2] Peter, N. (2024). The space debris challenge to the sustainability of the space economy. *European Review of International Studies*, *10*(3), 303–324. https://doi.org/https://doi.org/10.1163/21967415-10030003

[3] Kessler, D. J., & Cour-Palais, B. G. (1978). Collision frequency of artificial satellites: The creation of a debris belt. *Journal of Geophysical Research: Space Physics*, *83*, 2637–2646. https://doi.org/10.1029/JA083iA06p02637

[4] *ESA's annual space environment report 2024*. (2024). ESA's Space Debris Office.

[5] Flohrer, T., Braun, V., Krag, H., Merz, K., Lemmens, S., Virgili, B. B., & Funke, Q. (2015). Operational collision avoidance at ESOC.

[6] Dural, S., Tugcular, U., & Daser, B. (2021). General collision avoidance maneuver decision algorithm.

[7] Spencer, D. B., Sorge, M. E., & Skinner, M. A. (2024). Establishing "norms of behavior" for satellite collision avoidance maneuver planning. *Journal of Space Safety Engineering*, *11*(1), 120–126. https://doi.org/10.1016/j.jsse.2023.11.012

[8] Aida, S. (2016). Conjunction risk assessment and avoidance maneuver planning tools.

[9] Merz, K., Siminski, J., Bastida Virgili, B., Braun, V., Flegel, S., Flohrer, T., Funke, Q., Horstmann, A., Lemmens, S., Letizia, F., Mclean, F., Sanvido, S., & Schaus, V. (2021). ESA's collision avoidance service: Current status and special cases.

[10] Flohrer, T., Merz, K., Siminski, J., & Krag, H. (2020). Update on ESA's space safety programme and its cornerstone on collision avoidance.

[11] McInnes, C. R. (1999). *Solar sailing: Technology, dynamics and mission applications*. Springer.

[12] Garner, C. E. (2000). A solar sail design for a mission to the near-interstellar medium [ISSN: 0094243X]. *AIP Conference Proceedings*, *504*, 947–961. https://doi.org/10.1063/1.1290891

[13] Sawada, H., Mori, O., Okuizumi, N., Shirasawa, Y., Miyazaki, Y., Natori, M., Matunaga, S., Furuya, H., & Sakamoto, H. (2011). Mission report on the solar power sail deployment demonstration of IKAROS. *52nd AIAA/ASME/ASCE/AHS/ASC Structures, Structural Dynamics and Materials Conference*. https://doi.org/10.2514/6.2011-1887

[14] Alhorn, D. C., Casas, J. P., Agasid, E. F., Adams, Charles L., Laue, G., Kitts, C., & O'Brien, S. (2011). NanoSail-d: The small satellite that could! *25th Annual AIAA/USU Conference on Small Satellites*.

[15] Johnson, L., Betts, E., Heaton, A., Jones, C., McNutt, L., Pruitt, M., Stott, J., Wallace, D., Wilson, R., Castillo-Rogez, J., Lantoine, G., Seybold, C., & Sweetser, T. (2022). Near earth asteroid scout - mission update. *36th Annual Small Satellite Conference*.

[16] Mansell, J. R., Bellardo, J. M., Betts, B., Plante, B., & Spencer, D. A. (2023). LightSail 2 solar sail control and orbit evolution. *Aerospace*, *10*(7), 579. https://doi.org/10.3390/aerospace10070579

[17] Dono, A., Hendriks, T., & Wilkie, K. (2024). Navigation for the ACS3 solar sail mission.

[18] Kelly, P. W., Bevilacqua, R., Mazal, L., & Erwin, R. S. (2018). TugSat: Removing space debris from geostationary orbits using solar sails. *Journal of Spacecraft and Rockets*, *55*(2), 437–450. https://doi.org/10.2514/1.A33872

[19] Bombardelli, C., & Hernando-Ayuso, J. (2015). Optimal impulsive collision avoidance in low earth orbit. *Journal of Guidance, Control, and Dynamics*, *38*(2), 217–225. https://doi.org/10.2514/1.G000742

[20] Salemme, G., Armellin, R., & Di Lizia, P. (2020). Continuous-thrust collision avoidance manoeuvres optimization. *AIAA Scitech 2020 Forum*. https://doi.org/10.2514/6.2020-0231

[21] Palermo, M. F., DI Lizia, P., & Armellin, R. (2021). Numerically efficient methods for low-thrust collision avoidance manoeuvre design. *8th European Conference on Space Debris*, *8*.

[22] De Vittori, A., Palermo, M. F., Di Lizia, P., & Armellin, R. (2022). Low-thrust collision avoidance maneuver optimization. *Journal of Guidance, Control, and Dynamics*, *45*(10), 1815–1829. https://doi.org/10.2514/1.G006630

[23] Armellin, R. (2021). Collision avoidance maneuver optimization with a multiple-impulse convex formulation. *Acta Astronautica*, *186*, 347–362. https://doi.org/10.1016/j.actaastro.2021.05.046

[24] Pavanello, Z., Pirovano, L., Armellin, R., De Vittori, A., & Di Lizia, P. (2024). A convex optimization method for multiple encounters collision avoidance maneuvers. *AIAA SCITECH 2024 Forum*. https://doi.org/10.2514/6.2024-0845

[25] Kim, E.-H., Kim, H.-D., & Kim, H.-J. (2012). A study on the collision avoidance maneuver optimization with multiple space debris. *Journal of Astronomy and Space Sciences*, *29*(1), 11–21. https://doi.org/10.5140/JASS.2012.29.1.011

[26] Seong, J.-D., & Kim, H.-D. (2015). Collision avoidance maneuvers for multiple threatening objects using heuristic algorithms. *Proceedings of the Institution of Mechanical Engineers, Part G: Journal of Aerospace Engineering*, *229*(2), 256–268. https://doi.org/10.1177/0954410014530678

[27] Morselli, A., Armellin, R., Di Lizia, P., & Bernelli Zazzera, F. (2014). Collision avoidance maneuver design based on multi-objective optimization. *Advances in Astronautical Sciences*, *152*.

[28] Gonzalo, J. L., Colombo, C., & Di Lizia, P. (2018). Analysis and design of collision avoidance maneuvers for passive de-orbiting missions. *AAS 18-357*, 2189–2208.

[29] Colombo, C., Rossi, A., Dalla Vedova, F., Francesconi, A., Bombardelli, C., Trisolini, M., Gonzalo, J. L., Di Lizia, P., Giacomuzzo, C., Khan, S. B., Garcia-Pelayo, R., Braun, V., Virgili, B. B., & Krag, H. (2018). Effects of passive de-orbiting through drag and solar sails and electrodynamic tethers on the space debris environment. *IAC-18-A6.2.8*.

[30] Patera, R. P., & Peterson, G. E. (2003). Space vehicle maneuver method to lower collision risk to an acceptable level. *Journal of Guidance, Control, and Dynamics*, *26*(2), 233–237. https://doi.org/10.2514/2.5063

[31] Carzana, L., Visser, P., & Heiligers, J. (2022). Locally optimal control laws for earth-bound solar sailing with atmospheric drag. *Aerospace Science and Technology*, *127*, 107666. https://doi.org/10.1016/j.ast.2022.107666

[32] *U.s. standard atmosphere 1976*. (1976). United States Air Force.

[33] Verner, J. H. (2010). Numerically optimal runge–kutta pairs with interpolants. *Numerical Algorithms*, *53*(2), 383–396. https://doi.org/10.1007/s11075-009-9290-3

[34] Shampine, L. F., & Reichelt, M. W. (1997). The MATLAB ODE suite. *SIAM Journal on Scientific Computing*, *18*(1), 1–22. https://doi.org/10.1137/S1064827594276424

[35] Wakker, K. (2015). *Fundamentals of astrodynamics*. TU Delft Library.

[36] Wertz, J. R., & Larson, W. J. (1991). *Space mission analysis and design*. Kluwer.

[37] Kelly, P., & Bevilacqua, R. (2019). An optimized analytical solution for geostationary debris removal using solar sails. *Acta Astronautica*, *162*, 72–86. https://doi.org/10.1016/j.actaastro.2019.05.055

[38] Sumanth, M. R. (2019). Computation of eclipse time for low-earth orbiting small satellites. *International Journal of Aviation, Aeronautics, and Aerospace*. https://doi.org/10.15394/ijaaa.2019.1412

[39] Wilkie, W. K., Fernandez, J., Stohlman, O. R., Schneider, N., Dean, G., Kang, J. H., Cook, S., Warren, J., Brown, P., Denkins, T., Horner, S., Tapio, E., Straubel, M., Richter, M., & Heiligers, J. (2021). Overview of the NASA advanced composite solar sail system (ACS3) technology demonstration project. *AIAA Scitech 2021 Forum*. https://doi.org/10.2514/6.2021-1260

[40] *IADC space debris mitigation guidelines*. (2021, June). Inter-Agency Space Debris Coordination Committee.

[41] Gamez Losada, F., Visser, P., & Heiligers, J. (2024). Fundamentals of solar-sail transfers around planetary bodies. *Proceedings of the 29th International Symposium on Space Flight Dynamics*.

[42] Klinkrad, H. (2006). *Space debris: Models and risk analysis*. Springer ; Published in association with Praxis Pub.

[43] *Assessment of risk event statistics (ARES)*. (2021). ESA's Space Debris Office.

[44] Li, J.-S., Yang, Z., & Luo, Y.-Z. (2022). A review of space-object collision probability computation methods. *Astrodynamics*, *6*(2), 95–120. https://doi.org/10.1007/s42064-021-0125-x

[45] Alfano, S., & Oltrogge, D. (2018). Probability of collision: Valuation, variability, visualization, and validity. *Acta Astronautica*, *148*. https://doi.org/10.1016/j.actaastro.2018.04.023

[46] Jordaan, H. W. (2016). Spinning solar sail: The deployment and control of a spinning solar sail satellite.

[47] Foster, J. L. (1992). *A parametric analysis of orbital debris collision probability and maneuver rate for space vehicles*. NASA.

[48] Alfriend, K. T., Akella, M. R., Frisbee, J., Foster, J. L., Lee, D.-J., & Wilkins, M. (1999). Probability of collision error analysis. *Space Debris*, *1*, 21–35.

[49] Flohrer, T., Krag, H., & Klinkrad, H. (2008). Assessment and categorization of TLE orbit errors for the US SSN catalogue.

[50] Merz, K., Bastida Virgili, B., Braun, V., Flohrer, T., Funke, Q., Krag, H., & Lemmens, S. (2017). Current collision avoidance service by ESA's space debris office.

[51] Schiff, C. (2006). Adapting covariance propagation to account for the presence of modeled and unmodeled maneuvers. *AIAA/AAS Astrodynamics Specialist Conference and Exhibit*. https://doi.org/10.2514/6.2006-6294

[52] Bojkov, B., & Luus, R. (1996). Optimal control of nonlinear systems with unspecified final times. *Chemical Engineering Science*, *51*(6), 905–919. https://doi.org/10.1016/0009-2509(95)00340-1

[53] Longuski, J. M., Guzmán, J. J., & Prussing, J. E. (2014). *Optimal control with aerospace applications*. Springer New York. https://doi.org/10.1007/978-1-4614-8945-0

[54] Heiligers, J., Mingotti, G., & McInnes, C. (2014). Optimisation of solar sail interplanetary heteroclinic connections. *IAA-AAS-DyCoSS2-03-04*, *153*.

[55] Morante, D., Sanjurjo Rivo, M., & Soler, M. (2021). A survey on low-thrust trajectory optimization approaches. *Aerospace*, *8*(3), 88. https://doi.org/10.3390/aerospace8030088

[56] Topputo, F., & Zhang, C. (2014). Survey of direct transcription for low-thrust space trajectory optimization with applications. *Abstract and Applied Analysis*, *2014*, 1–15. https://doi.org/10.1155/2014/851720

[57] Mall, K. (2018). Advancing optimal control theory using trigonometry for solving complex aerospace problems. https://hammer.purdue.edu/articles/thesis/Advancing_Optimal_Control_Theory_Using_Trigonometry_For_Solving_Complex_Aerospace_Problems/7418204/1

[58] Song, Y., & Gong, S. (2019). Solar-sail deep space trajectory optimization using successive convex programming. *Astrophysics and Space Science*, *364*(7), 106. https://doi.org/10.1007/s10509-019-3597-x

[59] Patterson, M. A., & Rao, A. V. (2014). GPOPS-II: A MATLAB software for solving multiple-phase optimal control problems using hp-adaptive gaussian quadrature collocation methods and sparse nonlinear programming. *ACM Transactions on Mathematical Software*, *41*(1), 1–37. https://doi.org/10.1145/2558904

[60] Patterson, M. A., & Rao, A. V. (2016). *A general-purpose MATLAB software for solving multiple-phase optimal control problems version 2.3*.

[61] Macdonald, M., & McInnes, C. R. (2005a). Analytical control laws for planet-centered solar sailing. *Journal of Guidance, Control, and Dynamics*, *28*(5), 1038–1048. https://doi.org/10.2514/1.11400

[62] Macdonald, M., & McInnes, C. R. (2005b). Realistic earth escape strategies for solar sailing. *Journal of Guidance, Control, and Dynamics*, *28*(2), 315–323. https://doi.org/10.2514/1.5165

[63] Crowder, S., Delker, C., Forrest, E., & Martin, N. (2020). *Introduction to statistics in metrology*. Springer International Publishing. https://doi.org/10.1007/978-3-030-53329-8

[64] Montenbruck, O., & Gill, E. (2000). *Satellite orbits*. Springer Berlin Heidelberg. https://doi.org/10.1007/978-3-642-58351-3

6 Conclusions and Recommendations

The following is the final chapter of the thesis: it wraps up the main takeaway messages from the results given in the research paper, in Chapter 5, and highlights the main potential areas for expanding the presented research. First, in Section 6.1, the research questions presented in Chapter 3 are answered, based on the results of the project. Then, in Section 6.2, recommendations for future work are provided.

6.1 Conclusions

Envisioning the application of solar sails around Earth, due to the advantages brought by their propellantless nature, the objective of the work was to characterize the performance of solar sails in executing Collision Avoidance Maneuvers (CAMs). The dynamical model includes Earth's central gravity, its J2 term, and the Solar Radiation Pressure (SRP) acceleration. Collisions are evaluated based on the Probability of Collision (PoC), computed via Foster's method, and a covariance-mapping algorithm is used to model uncertainties, starting from an available dataset of Conjunction Data Messages (CDMs). CDMs are sent to notify satellite operators of threatening encounters. An extensive set of conjunctions is simulated (e.g., by varying orbital regimes, sail control authorities, and collision geometries), for an "ideal" and a "real" case. In the former, the covariance is retrieved exactly at the maneuver start epoch, and the target PoC for the maneuver is 10^{-4}; in the latter, a decision time is introduced, thus the covariance is retrieved one day before the maneuver start epoch, and the target PoC is 10^{-6}. The optimal control problem is derived and solved via direct collocation, seeking time-optimal maneuvers while constraining the collision probability.

In order to draw relevant conclusions, each research (sub-)question is answered in this section, based on the presented results.

Research Question 1

What is the minimum time required, before the closest approach, to maneuver and bring the probability of collision below a set threshold, for all simulated scenarios?

In the "ideal" case, where the warning is issued at the start of the maneuver, the minimum maneuver time usually lies between 10 and 40 minutes, and never exceeds one orbital period. The maximum time is found to be approximately 104 minutes (less than two hours), whereas the mean value is 25 minutes. On the other hand, in the "real" case, the maneuver time is intuitively larger, as the required collision probability is decreased and the uncertainty is enhanced due to the maneuver execution

upon an earlier CDM. Results are clustered between 30 and 60 minutes, with the average time being 47 minutes, and can exceed one orbital revolution. The maximum time is approximately six hours, although the vast majority of the maneuvers (99% of the scenarios) last less than three hours, and require less than two orbital periods to be allocated for the maneuver.

Research Question 1.a

What is the influence of the sail, debris, and conjunction parameters on the results?

Greater control authority (area-to-mass ratio) intuitively yields shorter maneuver times. A dependence on the altitude is found: although longer maneuver times are registered at higher altitudes, the fraction of the orbit spent for maneuvering shows a clear decreasing trend with orbital radius. This could comply with stricter mission constraints on the fraction of the orbit allocated for maneuvering. Symmetry is registered by analyzing the effect of the encounter angle (between the sailcraft and debris velocities at the closest approach), showing the results only depend on the azimuth angle (between the relative and the sailcraft velocities at the closest approach). The relation with the PoC is explicit as the parameters that mainly influence the maneuver time are those that enter the probability computation. Specifically, smaller miss distances cause the PoC, and the maneuver time, to grow. Likewise, smaller debris size requires longer maneuver times, since smaller objects are subject to greater uncertainties. The better the knowledge of the debris state, the shorter the maneuver time. Solar-sail-specific effects are highlighted. First, eclipses cause an increase in the maneuver time, since sails cannot be maneuvered when in shadow. Second, if the debris is displaced along the sunlight direction, the sailcraft will tend to move toward (rather than escape from) the object, yielding longer maneuver times. The time to maneuver is only weakly influenced by the orbit orientation with respect to the Sun: results are therefore independent of the Earth-Sun configuration (i.e., the time of the year).

Research Question 1.b

How do results fit within the current typical time frame of operational collision avoidance?

For all scenarios, the total maneuver time is well below the boundary value of one day, which is regarded as the latest time to decide whether to execute a maneuver. Therefore, results fit the current operational framework: collision avoidance maneuvers are feasible for solar sails. As a matter of fact, nowadays, CDMs are received by satellite operators even several days prior to the closest approach, and the decision to maneuver is taken approximately one day from the closest approach. For maneuvers requiring, at most, a few hours, the flight control team should be able to uplink the maneuver input to the sailcraft during a passage over the ground station.

Research Question 2

What is the optimal control profile of the solution, in terms of relative orientation between the acceleration provided by the solar sail and the direction of the sunlight throughout the maneuver, for all simulated scenarios?

Considering the average over time of the components of the control profile provided by the optimizer, for all simulated scenarios, a cluster is identified close to unity for the component along the sunlight direction. The acceleration tends to align itself with the direction of sunlight to perform the CAM.

Research Question 2.a

What is the influence of the sail, debris, and conjunction parameters on the results?

A negative correlation with maneuver time highlights that the average thrust component in the sunlight direction tends to grow with shorter maneuver time. Maneuver time thus benefits from thrusting in the direction of sunlight. This is confirmed by a positive correlation with the debris size, since shorter maneuver times are found for bigger debris sizes. However, a negative correlation is found for the miss distance: all other parameters being equal, a smaller miss distance requires the control to be directed predominantly along the sunline vector, compared to less threatening conjunctions given by a larger miss distance. No strong dependence on the area-to-mass ratio and altitude is registered: regardless of the control authority and altitude of the sail, the optimal control profile will show similar trends. The optimal control profile is greatly affected by the orientation of the orbit with respect to the Sun. If the sunlight acts in the orbital plane, the out-of-plane component is zeroed out; on the contrary, if the sunlight is parallel to the out-of-plane direction, then the component in such direction is predominant, and the average thrust component parallel to the velocity is clustered around zero. Nevertheless, the projection of the control vector in the orbital plane is found to always be non-zero, showing that in-plane maneuvering is unavoidable for executing a CAM. In the orbital plane, the yaw angle, between the projection of the control vector and the velocity, depends on the relative orientation between velocity and sunlight directions.

Research Question 2.b

Is the optimal control profile comparable to one of the locally optimal steering laws, to maximize the rate of change of a specific orbital element?

The locally optimal steering laws that better approximate the final state of the sail outputted by the optimizer tend to be those to change either the semi-major axis or the eccentricity: this happens in 86% and 92% of the scenarios, in the "ideal" and "real" cases, respectively. These laws require in-plane acceleration, confirming that in-plane maneuvering is generally unavoidable in the optimized CAMs. A greater percentage of maneuvers is closer to "out-of-plane" steering laws, to change the inclination and right ascension of the ascending node, when the aspect angle is lowest and the thrust has a component outside the orbital plane. Moreover, the PoC (at the closest approach) for the final state propagated through the "closest" control law, falls below the required value in 29% of the scenarios, for the "ideal" case, and in 95% of the scenarios, for the "real" case, characterized by longer maneuver times. This could streamline solar-sail collision avoidance maneuver planning by only considering these straightforward control laws, especially if mission constraints allow longer maneuver times.

6.2 Recommendations for Future Work

Since this work is the first-ever iteration of an analysis of the performance of solar sails in executing collision avoidance maneuvers in Earth orbit, there is room for expanding the research. In this section, first the assumptions made throughout the project are addressed in Subsection 6.2.1. Subsequently, additional research areas are proposed in Subsection 6.2.2.

6.2.1 Relaxation of Assumptions

Several simplifications were introduced to carry out the presented project. Therefore, the research would benefit from the relaxation of one or more of the simplifying assumptions. Recommendations for future work stemming from the assumptions made regarding the dynamical model, design parameters, encounter and probability model, and uncertainty retrieval are provided in this subsection.

Dynamical Model

Only Earth's central gravity, its J2 term, and the SRP perturbation were included in the dynamical model, since most studies concluded orbital perturbations are negligible in CAM design.

A higher-fidelity dynamical model could be implemented to verify perturbations are indeed negligible also for CAMs executed by solar sails. Moreover, an optical SRP model could be investigated, and planetary radiation pressure could be included. The atmospheric acceleration should be accounted for, given the high area-to-mass ratio of solar sails. In this study, the atmosphere was not modeled as the minimum operational altitude of the sail was fixed at 1000 km (where the atmosphere is so rarefied that its interactions can be ignored), yet additional research could be carried out for CAMs executed at altitudes lower than 1000 km.

Design Parameters

While the design parameters were selected to make the set of simulated scenarios as realistic and extensive as possible, there is room for further development.

More orbital regimes for the sailcraft could be modeled, for example considering altitudes below 1000 km. Moreover, it is suggested to act on the eccentricity, both of the sailcraft and the debris orbits, although, for the latter, most catalog objects are actually on near-circular orbits. Augmenting the eccentricity of the debris would also imply different uncertainty values (it is pointed out that, in the employed dataset for the uncertainty retrieval, one orbital class is already available for values of eccentricity greater than 0.1).

Encounter and Probability Model

This work only focused on short-term encounter models, given they are the most common ones. Additionally, the methods to compute the PoC rely on the assumption of zero-mean, Gaussian, and uncorrelated positional errors, and on modeling the objects as spheres.

Future research could focus on analyzing encounters for which one (or more) of the assumptions of the short-term encounter model do not hold. Long-term encounters could be investigated: in such cases, the covariance matrix could not be treated as constant, and also the uncertainty on the velocity of the objects would play a role. Moreover, it would be interesting, in future iterations of the study, to consider the implementation of methods that allow the errors to follow a non-Gaussian distribution.

Finally, although modeling the objects as spheres is conservative (with the total area being projected in the encounter plane), it could be worth analyzing the change in the PoC due to the change in the attitude of the sail at the closest approach.

Uncertainty Retrieval

To model the uncertainties, the same assumptions underlying the encounter and probability model definition hold. In addition, the sail position errors are neglected, assuming an onboard Global Positioning System (GPS) receiver, and the debris covariance is assumed to be diagonal in a radial-transverse-normal reference frame centered on the debris object. However, the greatest limitation of this work, concerning uncertainty retrieval, is represented by the limited dataset of CDMs that was employed.

The case of a spacecraft not having an onboard GPS could be simulated. In such a scenario, the uncertainty of the sailcraft would need to be modeled. This could be done either by estimating the tracking accuracy for objects with high area-to-mass ratio (also considering the uncertainty in the SRP and drag coefficients), and propagating the uncertainties in time, or deriving the sailcraft uncertainties through CDMs, if available.

The greatest improvement to the project would be given by accessing a complete dataset of CDMs. As a matter of fact, the employed dataset is limited in its representation of orbital classes, meaning that only one mapping factor could be computed, and this factor was applied to all orbital classes. Although the mapping algorithm was tested for a neighboring orbital class and the results were deemed satisfactory, there is no guarantee that this would hold for all orbital classes. This limit could be overcome if sufficient CDMs were available for all orbital classes under scrutiny.

6.2.2 Future Research Areas

Further research could be conducted to expand this study, starting from the conclusions drawn in Section 6.1, and two main recommendations are provided in this subsection.

This work focused on finding optimal maneuvers that would require the shortest warning time, before the closest approach, to be executed. This means that the maneuvers are designed to end exactly at the closest approach. However, future research could investigate optimal maneuvers with the introduction of a certain time interval (for instance, for safety constraints) between the maneuver end epoch and the closest approach epoch. Moreover, different covariance retrieval epochs could be simulated, for maneuvers executed even more than one day before the conjunction.

As was highlighted by this project, locally optimal steering laws, to maximize the rate of change of the orbital elements, can be a viable alternative to performing a CAM. Especially allowing a longer maneuver time (still well below the threshold of one day), it was proved that maneuvering through one of the locally optimal control laws satisfies the PoC requirement, in most simulated scenarios. Therefore, future work could aim at characterizing the performance of such control laws in executing CAMs, to simplify the maneuver planning process by only considering the locally optimal steering laws, or even a subset of them, such as the ones to change the semi-major axis and eccentricity.

Appendices

Additional information is provided in the appendices to allow a more complete understanding of the thesis document. The chapter is structured as follows. First, the integrator analysis is outlined in Appendix A. Subsequently, the dynamics matrix, to propagate the state transition matrix in time, is formulated in Appendix B. Then, the employed locally optimal steering laws are given in Appendix C. The main tasks to verify the codes written throughout the project are presented in Appendix D. Finally, the thesis research plan is provided in Appendix E.

A Integrator Selection

Three reference circular orbits (whose RAAN is set to 0 degrees) are selected as test cases:

1. LEO equatorial orbit, with an altitude of 1000 km and inclination of 0 degrees;
2. LEO polar orbit, with an altitude of 1000 km and inclination of 90 degrees;
3. GEO equatorial orbit, with an altitude of 35786 km and inclination of 0 degrees.

Benchmark trajectories are generated with a high-accuracy integrator (*ode78*, with relative and absolute tolerances set to 10^{-12}, constraining the maximum step size to less than one second). The reference propagations last one day and are deemed sufficient compared to the operational collision avoidance time frame. To consider the SRP effect, the sailcraft (with an area-to-mass ratio of 5 $\frac{m^2}{kg}$) is propagated by applying the control law to maximize the increase in the SMA.

It is chosen to require an accuracy of 0.1 m for the norm of the position error, by reducing by one order of magnitude the physical requirement for an accuracy of 1 m. Such a requirement stems from the fact that 1 m is the smallest value of miss distance to be simulated (see Table 4.6). As for the velocity, short-term encounters do not pose strict constraints on the velocity accuracy, as the relative velocities are of several kilometers per second. For this reason, the analysis focuses on position errors, and it is then verified that the velocity error norm is below 0.0001 $\frac{m}{s}$ (which is deemed a small enough value).

All integrators, available within MATLAB *ode* suite for non-stiff problems, are tested (Shampine and Richelt, 1997): *ode23*, *ode45*, *ode113*, *ode78*, *ode89*. As for the relative and absolute tolerances, after some trial and error runs, three values per parameter are selected: 10^{-8}, 10^{-10}, 10^{-12}. The accuracy is computed as the difference between the propagated state and the interpolated benchmark state. Figure A.1 shows the maximum error as a function of the number of function evaluations performed by the integrator, as the latter is proportional to the computational time: *ode23* is the slowest integrator, and in most cases fails to comply with the accuracy requirement, whereas *ode113* is the fastest one, but there are cases in which the accuracy is not met. As for *ode45*, *ode78*, and *ode89*, they all satisfy the accuracy requirement if the integration is performed with strict enough tolerances, but higher-order integrators perform better than *ode45* in terms of number of function evaluations. Although *ode78* and *ode89* show similar performances, the latter is chosen, as it can be more efficient than the former when tolerances are very tight (Shampine and Reichelt, 1997).

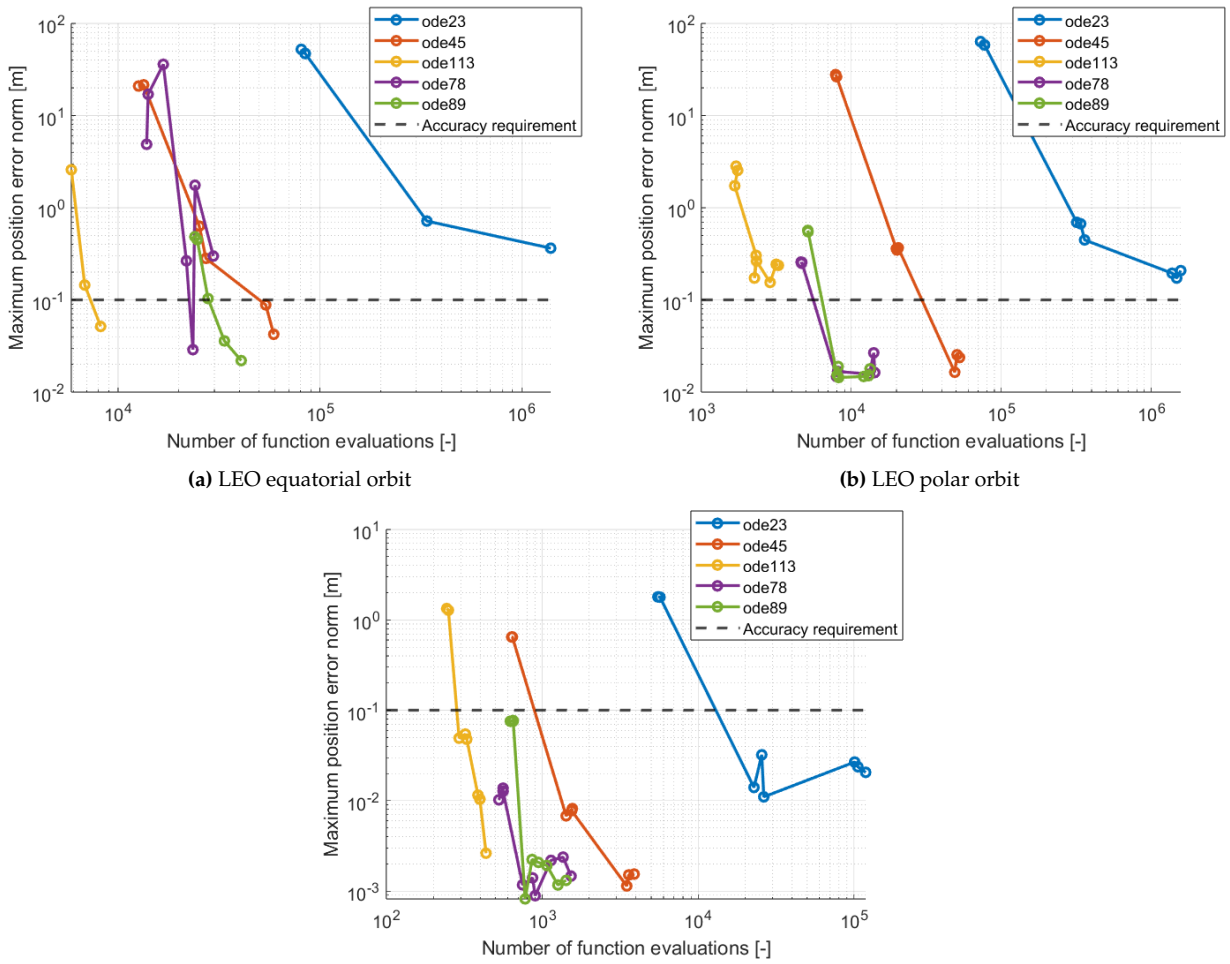

(a) LEO equatorial orbit

(b) LEO polar orbit

(c) GEO equatorial orbit

Figure A.1: Maximum norm of the position error as a function of the number of function evaluations, for different integrators

Once the integrator is chosen, the tolerances shall be selected. Figure A.2 shows the time evolution of the position error: the driver for the choice is the LEO equatorial orbit, for which only two combinations of tolerances successfully meet the requirement (Fig. A.1a). The combination with the largest tolerances is chosen, from Fig. A.2a, to save on runtime: the selected integrator is *ode89*, with relative and absolute tolerances of 10^{-12} and 10^{-8}, respectively.

B Dynamics Matrix

To propagate the STM, it is necessary to compute the dynamics matrix, which describes the relation between the derivative of the state vector and the state vector itself, at a given time epoch (Rugh, 1996). The formulation is given in the ECI frame, since dynamics are expressed in such a frame (the matrix can then be rotated to any other reference frame). Since the covariance matrix of the debris needs to be propagated through the STM, only the state vector of the debris (in position and velocity) is taken into account:

$$G_I(t) = \begin{bmatrix} \frac{\partial \mathbf{v}_{I,D}(t)}{\partial \mathbf{r}_{I,D}(t)} & \frac{\partial \mathbf{v}_{I,D}(t)}{\partial \mathbf{v}_{I,D}(t)} \\ \frac{\partial \mathbf{a}_{I,D}(t)}{\partial \mathbf{r}_{I,D}(t)} & \frac{\partial \mathbf{a}_{I,D}(t)}{\partial \mathbf{v}_{I,D}(t)} \end{bmatrix} = \begin{bmatrix} \tilde{0}_{3\times3} & \tilde{I}_{3\times3} \\ B_I(t) & \tilde{0}_{3\times3} \end{bmatrix} \tag{B.1}$$

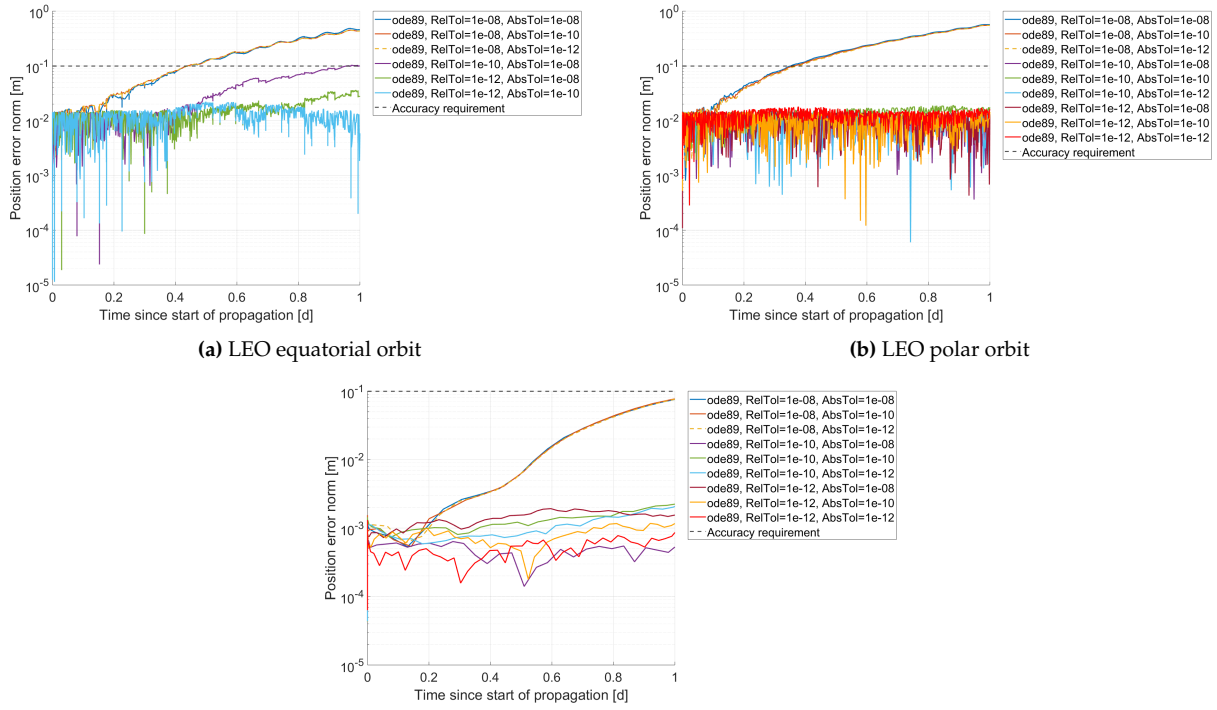

(a) LEO equatorial orbit

(b) LEO polar orbit

(c) GEO equatorial orbit

Figure A.2: Norm of the position error as a function of time, for *ode89*, with different relative and absolute tolerances

where $\tilde{0}$ is the zero matrix and the sub-matrix B_I describes the dependence of the acceleration vector on the position vector.

For the motion of the debris, governed by Earth's central gravity and its J2 term, Eqs. 4.5 and 4.6, written for the sailcraft S/C, can be accommodated to the debris object D:

$$\mathbf{a}_{I,D,\mu_\oplus} = -\frac{\mu_\oplus}{r_{I,D}^3}\mathbf{r}_{I,D} \tag{B.2}$$

$$\mathbf{a}_{I,D,J2} = -\frac{3}{2}\frac{\tilde{R}_\oplus^2}{r_{I,D}^5}J2\mu_\oplus[(r_{I,D,x}\hat{\mathbf{x}}_I + r_{I,D,y}\hat{\mathbf{y}}_I)(1-5\frac{r_{I,D,z}^2}{r_{I,D}^2}) + r_{I,D,z}(3-5\frac{r_{I,D,z}^2}{r_{I,D}^2})\hat{\mathbf{z}}_I] \tag{B.3}$$

This yields:

$$B_I(t) = \frac{\partial \mathbf{a}_{I,D}(t)}{\partial \mathbf{r}_{I,D}(t)} = \frac{\partial \mathbf{a}_{I,D,\mu_\oplus}(t)}{\partial \mathbf{r}_{I,D}(t)} + \frac{\partial \mathbf{a}_{I,D,J2}(t)}{\partial \mathbf{r}_{I,D}(t)} = B_{I,\mu_\oplus}(t) + B_{I,J2}(t) \tag{B.4}$$

Performing the analytical derivation of the two acceleration terms with respect to the Cartesian position vector, and omitting to explicitly write the dependence on time to ease the notation, yields:

$$B_{I,\mu_\oplus} = \begin{bmatrix} -\frac{\mu_\oplus}{r_{I,D}^3} + 3\frac{\mu_\oplus}{r_{I,D}^5}r_{I,D,x}^2 & 3\frac{\mu_\oplus}{r_{I,D}^5}r_{I,D,x}r_{I,D,y} & 3\frac{\mu_\oplus}{r_{I,D}^5}r_{I,D,x}r_{I,D,z} \\ 3\frac{\mu_\oplus}{r_{I,D}^5}r_{I,D,x}r_{I,D,y} & -\frac{\mu_\oplus}{r_{I,D}^3} + 3\frac{\mu_\oplus}{r_{I,D}^5}r_{I,D,y}^2 & 3\frac{\mu_\oplus}{r_{I,D}^5}r_{I,D,y}r_{I,D,z} \\ 3\frac{\mu_\oplus}{r_{I,D}^5}r_{I,D,x}r_{I,D,z} & 3\frac{\mu_\oplus}{r_{I,D}^5}r_{I,D,y}r_{I,D,z} & -\frac{\mu_\oplus}{r_{I,D}^3} + 3\frac{\mu_\oplus}{r_{I,D}^5}r_{I,D,z}^2 \end{bmatrix} \tag{B.5}$$

$$B_{I,J2} = \begin{bmatrix} b_{11} & b_{12} & b_{13} \\ b_{21} & b_{22} & b_{23} \\ b_{31} & b_{32} & b_{33} \end{bmatrix} \tag{B.6}$$

After defining the multiplying factor

$$\tilde{k} = -\frac{3}{2} R_{\oplus}^2 J2 \mu_{\oplus} \tag{B.7}$$

the coefficients of the $B_{I,J2}$ matrix can be expressed as:

$$\begin{cases}
b_{11} &= -5 \cdot \tilde{k} \cdot \frac{1}{r_{I,D}^7} r_{I,D,x}^2 \left(1 - 5\frac{r_{I,D,z}^2}{r_{I,D}^2}\right) + \tilde{k} \cdot \frac{1}{r_{I,D}^5} \left(1 - 5\frac{r_{I,D,z}^2}{r_{I,D}^2}\right) + 10 \cdot \tilde{k} \cdot \frac{1}{r_{I,D}^9} r_{I,D,x}^2 r_{I,D,z}^2 \\
b_{12} &= -5 \cdot \tilde{k} \cdot \frac{1}{r_{I,D}^7} r_{I,D,x} r_{I,D,y} \left(1 - 5\frac{r_{I,D,z}^2}{r_{I,D}^2}\right) + 10 \cdot \tilde{k} \cdot \frac{1}{r_{I,D}^9} r_{I,D,x} r_{I,D,y} r_{I,D,z}^2 \\
b_{13} &= -5 \cdot \tilde{k} \cdot \frac{1}{r_{I,D}^7} r_{I,D,x} r_{I,D,z} \left(1 - 5\frac{r_{I,D,z}^2}{r_{I,D}^2}\right) + 5 \cdot \tilde{k} \cdot \frac{1}{r_{I,D}^7} r_{I,D,x} \cdot 5\frac{2r_{I,D,z} r_{I,D}^2 - 2r_{I,D,z}^3}{r_{I,D}^4} \\
b_{21} &= -5 \cdot \tilde{k} \cdot \frac{1}{r_{I,D}^7} r_{I,D,x} r_{I,D,y} \left(1 - 5\frac{r_{I,D,z}^2}{r_{I,D}^2}\right) + 10 \cdot \tilde{k} \cdot \frac{1}{r_{I,D}^9} r_{I,D,x} r_{I,D,y} r_{I,D,z}^2 \\
b_{22} &= -5 \cdot \tilde{k} \cdot \frac{1}{r_{I,D}^7} r_{I,D,y}^2 \left(1 - 5\frac{r_{I,D,z}^2}{r_{I,D}^2}\right) + \tilde{k} \cdot \frac{1}{r_{I,D}^5} \left(1 - 5\frac{r_{I,D,z}^2}{r_{I,D}^2}\right) + 10 \cdot \tilde{k} \cdot \frac{1}{r_{I,D}^9} r_{I,D,y}^2 r_{I,D,z}^2 \\
b_{23} &= -5 \cdot \tilde{k} \cdot \frac{1}{r_{I,D}^7} r_{I,D,y} r_{I,D,z} \left(1 - 5\frac{r_{I,D,z}^2}{r_{I,D}^2}\right) + 5 \cdot \tilde{k} \cdot \frac{1}{r_{I,D}^7} r_{I,D,y} \cdot 5\frac{2r_{I,D,z} r_{I,D}^2 - 2r_{I,D,z}^3}{r_{I,D}^4} \\
b_{31} &= -5 \cdot \tilde{k} \cdot \frac{1}{r_{I,D}^7} r_{I,D,x} r_{I,D,z} \left(3 - 5\frac{r_{I,D,z}^2}{r_{I,D}^2}\right) + 10 \cdot \tilde{k} \cdot \frac{1}{r_{I,D}^9} r_{I,D,x} r_{I,D,z}^3 \\
b_{32} &= -5 \cdot \tilde{k} \cdot \frac{1}{r_{I,D}^7} r_{I,D,y} r_{I,D,z} \left(3 - 5\frac{r_{I,D,z}^2}{r_{I,D}^2}\right) + 10 \cdot \tilde{k} \cdot \frac{1}{r_{I,D}^9} r_{I,D,y} r_{I,D,z}^3 \\
b_{33} &= -5 \cdot \tilde{k} \cdot \frac{1}{r_{I,D}^7} r_{I,D,z}^2 \left(3 - 5\frac{r_{I,D,z}^2}{r_{I,D}^2}\right) + \tilde{k} \cdot \frac{1}{r_{I,D}^5} \left(3 - 5\frac{r_{I,D,z}^2}{r_{I,D}^2}\right) + 5 \cdot \tilde{k} \cdot \frac{1}{r_{I,D}^7} r_{I,D,z} \cdot 5\frac{2r_{I,D,z} r_{I,D}^2 - 2r_{I,D,z}^3}{r_{I,D}^4}
\end{cases} \tag{B.8}$$

C Locally Optimal Steering Laws

The thrust direction, in the RTN frame of the sail, to maximize the four analyzed orbital elements, is:

Semi-major axis ($\tilde{a}$)

$$\boldsymbol{\lambda}_{O,\tilde{a}} = \begin{bmatrix} e \cdot sin(\theta) \\ 1 + e \cdot cos(\theta) \\ 0 \end{bmatrix} \tag{C.1}$$

Eccentricity (e)

$$\boldsymbol{\lambda}_{O,e} = \begin{bmatrix} sin(\theta) \\ cos(\theta) + cos(\tilde{E}) \\ 0 \end{bmatrix} \tag{C.2}$$

Inclination (i)

$$\boldsymbol{\lambda}_{O,i} = \begin{bmatrix} 0 \\ 0 \\ sgn(cos(\omega + \theta)) \end{bmatrix} \tag{C.3}$$

RAAN (Ω)

$$\boldsymbol{\lambda}_{O,\Omega} = \begin{bmatrix} 0 \\ 0 \\ sgn(sin(\omega + \theta)) \end{bmatrix} \tag{C.4}$$

where θ is the true anomaly, $\tilde{E}$ is the eccentric anomaly, and ω is the argument of perigee.
Equations C.1-C.4 increase the orbital element: to obtain a decrease, the direction should be flipped.

The formulation of the locally optimal steering laws is given by Macdonald and McInnes (2005a, 2005b) for planet-centered applications, starting from the formulation by McInnes (1999). The direction $\boldsymbol{\lambda}$, from Eqs. C.1-C.4, is rotated in the sunlight frame. Since, in the ideal force model, the acceleration is directed along the normal, and employing the relation between normal and attitude

angles in the sunlight frame (Eq. 4.7), the required cone and clock angle are derived:

$$\boldsymbol{\lambda}_S = \begin{bmatrix} \lambda_{S,x} \\ \lambda_{S,y} \\ \lambda_{S,z} \end{bmatrix} \rightarrow \begin{cases} \alpha_{req} = acos(\lambda_{S,x}) \\ \delta_{req} = acos(\frac{\lambda_{S,z}}{\sqrt{\lambda_{S,y}^2 + \lambda_{S,z}^2}}) \end{cases} \tag{C.5}$$

However, the actual cone angle will be different from the one in Eq. C.5. The optimal cone angle is found by a standard optimization process (Green, 1977):

$$tan(\alpha_{opt}) = \frac{-3cos(\alpha_{req}) + \sqrt{9cos^2(\alpha_{req}) + 8sin^2(\alpha_{req})}}{4sin(\alpha_{req})} \tag{C.6}$$

D Verification

In the following section, a summary of the techniques employed to verify the methods used throughout the project is provided. The verification of the dynamical model, of the collision scenario definition, and of the optimization setup is addressed in Appendices D.1, D.2, and D.3, respectively.

D.1 Dynamical Model

To test the correct formulation of the dynamical model, first the correct implementation of the rotation matrices is tested. Every sample rotation matrix is tested, to check the basic properties are respected (Swokowski, 1979): the inverse of a rotation matrix is its transpose; the determinant of a rotation matrix is equal to one (for right-handed rotations); rotating two random vectors, the angle between them is preserved; rotating a random vector, its magnitude is preserved.

In the dynamical model, three sources of acceleration are considered: Earth's central gravity, Earth's J2 perturbation, and SRP perturbation. Their magnitude and direction are tested and compared to the expected values. As for the Earth's gravitational pull, Montenbruck and Gill (2000) provide the evolution of the acceleration magnitude with altitude. As for the SRP, the force produced by an ideal square sail with a side of 100 m, for a set of cone angles, is computed by McInnes (1999). Figure D.1 shows the reproduction of the two test cases, presenting the evolution of the acceleration with altitude (Fig. D.1a), and of the SRP force with the sail attitude (Fig. D.1b).

To test the correct propagation of the equations of motion (Eqs. 4.4), the effect of the acceleration sources is compared to theoretical expectations. The chosen reference orbit is a "dawn-dusk" SSO, at an altitude of 1000 km, for which the orbital parameters are given in Table D.1. A Sun-synchronous orbit allows verifying the expected J2 effect on the RAAN; moreover, a "dawn-dusk" orbit allows testing the SRP effect without considering eclipsing events.

$\tilde{a}$ [km]	e [-]	i [deg]	Ω [deg]	ω [deg]
7385.5255	0.001	99.5125	269.0767	0

Table D.1: Keplerian elements of the test orbit

1. **Earth's central gravity**
   The motion of a spacecraft subject to Earth's central gravity is modeled through the two-body problem (Wakker, 2015): all orbital elements, except for the true anomaly, are expected to stay

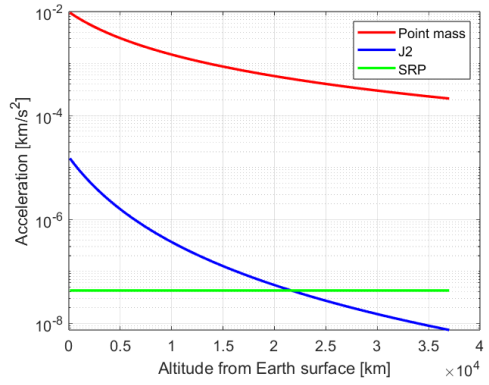

(a) Acceleration magnitude, as a function of the altitude (reproducing Montenbruck and Gill (2000))

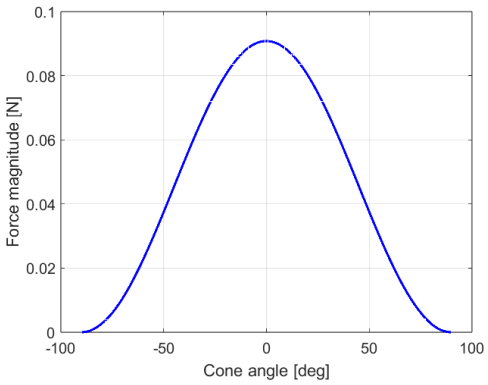

(b) Force from the SRP, as a function of the cone angle (reproducing McInnes (1999))

Figure D.1: Reproduction of two test cases to test the dynamical model

constant. This can be appreciated in Fig. D.2, which presents the evolution in time of the orbital elements: only the true anomaly changes, going from 0 to 360 degrees.

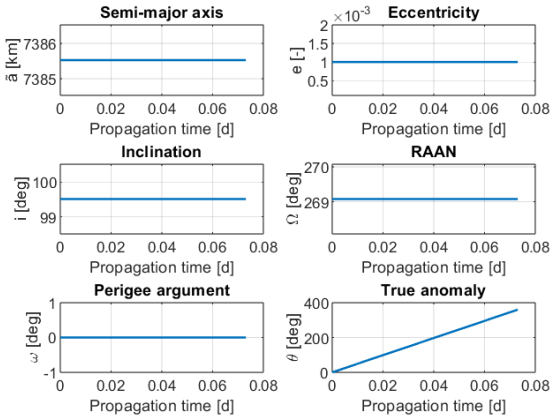

(a) 1-orbit propagation

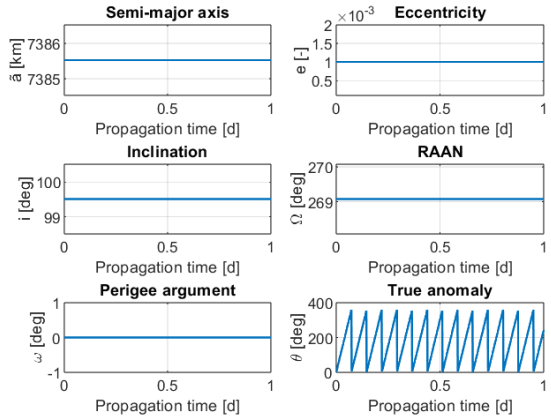

(b) 1-day propagation

Figure D.2: Time-evolution of the Keplerian elements, under Earth's central gravity attraction

2. **Earth's oblateness**
   If the J2 perturbation is added, all elements are expected to change: this is observed in Fig. D.3, showing the evolution in time of the orbital elements propagated under the J2 perturbation. Among other effects, the SMA and inclination are shown to be subject to short-periodic changes (Wertz and Larson, 1991). As the propagated orbit is Sun-synchronous, it is verified that the precession of the orbit matches the theoretical expectations: indeed, the change in the RAAN over one day (in Fig. D.3b) equals 0.9856 degrees (Wakker, 2015).

3. **Solar radiation pressure**
   To test the SRP effect, McInnes (1999) is used as reference, as his work, focusing on the derivation of the steering laws to increase the semi-major axis, gives formulas to approximate the change in the SMA over one orbit. Hence, the locally optimal steering law to increase the SMA is applied, with the SRP being the only perturbation acting on the spacecraft motion, in order to isolate its effect (hence, the J2 effect is not included). The expected change in the SMA, over one orbit, is

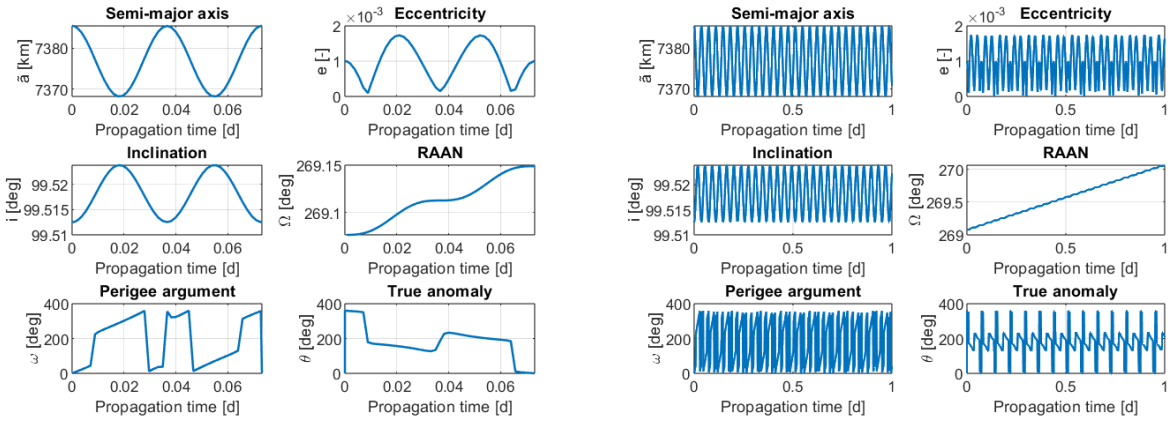

(a) 1-orbit propagation

(b) 1-day propagation

Figure D.3: Time-evolution of the Keplerian elements, for a dynamical model which includes the J2 perturbation

given by:

$$\Delta\tilde{a} = \frac{5.52 \cdot a_c}{\mu_\oplus} \cdot \tilde{a}^3 \tag{D.1}$$

The evolution over time of the Keplerian elements is shown in Fig. D.4, whereas the numerical results are provided in Table D.2, and results are deemed satisfactory compared to theoretical expectations.

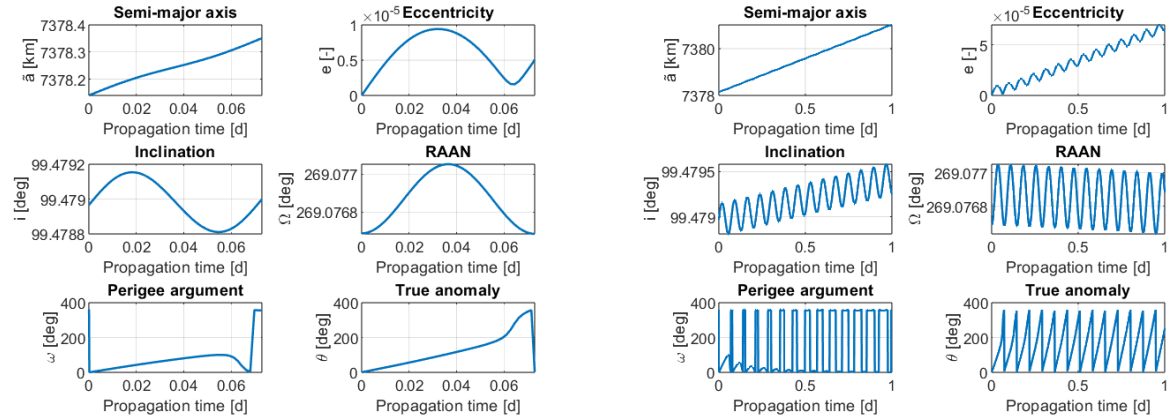

(a) 1-orbit propagation

(b) 1-day propagation

Figure D.4: Time-evolution of the Keplerian elements, for a dynamical model which includes the SRP perturbation, applying the locally optimal steering law to maximize the increase of the semi-major axis

	One orbit	**One day**
Approximated $\Delta\tilde{a}$ [km] (Eq. D.1)	0.237	3.256
Computed $\Delta\tilde{a}$ [km]	0.211	2.878

Table D.2: Approximated and computed values for the change in the semi-major axis, applying the locally optimal steering law to maximize its increase

Finally, the correct eclipse modeling is verified. Fig. D.5 shows the eclipse time for LEO and GEO

orbits. For circular orbits, the eclipse time is a fraction of the orbital period, proportional to the angular difference between the true anomalies at the edges of the shadow region. In LEO (Fig. D.5a), test cases from the work of Sumanth (2019) are reproduced (considering a circular orbit whose RAAN is 0 degrees), showing how larger fractions of the orbit spent in shadow are registered at lower altitudes. In all cases, the maximum fraction of the orbit spent in eclipse is at the vernal equinox. In GEO (Fig. D.5b), where eclipses only occur twice per year, at equinoxes, the maximum duration of an eclipsing event is approximately 72 minutes, which is registered exactly at the equinoxes (Kelly and Bevilacqua, 2021).

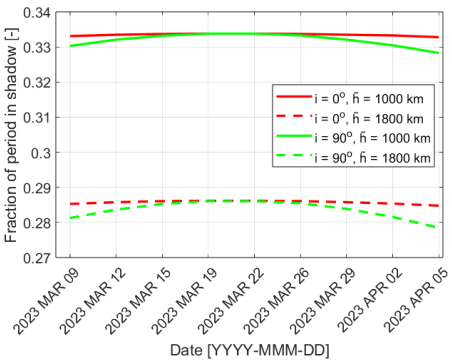

(a) Orbit fraction in eclipse, in LEO (reproducing Sumanth (2019)

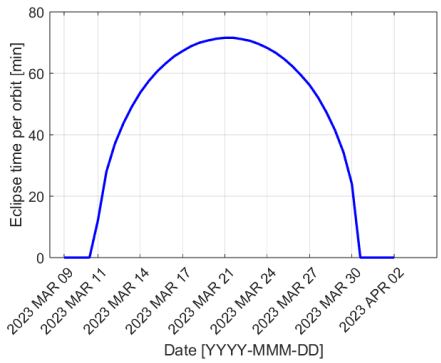

(b) Time in eclipse, in GEO

Figure D.5: Eclipse time analysis, as a function of the time of the year

The ephemerides retrieval is treated as already tested and verified, since it is carried out via SPICE.

D.2 Collision Scenario Definition

To test the uncertainty generation algorithm, for the orbital class which is taken as reference (near-circular orbits, with altitudes between 800 km and 25000 km and inclinations above 60 degrees), it is verified that the mapping algorithm can match exactly the uncertainties extrapolated by the CDMs, starting from the TLE uncertainties, for the three reference directions, and for the "small" and "large" debris sizes. The linear regression is performed employing MATLAB's *polyfit*.

The second orbital class for which CDM data is available (near-circular orbits, with altitudes below 800 km and inclinations above 60 degrees) is used to test the goodness of the assumption upon which the uncertainty mapping is based, as the same mapping factor is applied to multiple orbital classes. Figure D.6 shows the results from the mapping against those obtained directly from the available CDMs: the uncertainty evolution follows a similar shape.

To verify the analytical propagation of the STM, the STM is also computed numerically, through finite differencing techniques (Schiff, 2006). The change in the final state is evaluated, when the initial state is perturbed by a known quantity. If central differencing is applied:

$$\Phi(t_f, t_0)_{\tilde{i},\tilde{j}} \approx \frac{\boldsymbol{\rho}_{\tilde{i}}(t_f, \boldsymbol{\rho}_0 + \epsilon \hat{\mathbf{e}}_{\tilde{j}}) - \boldsymbol{\rho}_{\tilde{i}}(t_f, \boldsymbol{\rho}_0 - \epsilon \hat{\mathbf{e}}_{\tilde{j}})}{2\epsilon} \tag{D.2}$$

where the subscripts $(\tilde{i}, \tilde{j})$ determine the generic row and column, $\hat{\mathbf{e}}_{\tilde{j}}$ is a unit vector with components $\hat{\mathbf{e}}_{\tilde{j}}(\tilde{i}) = \tilde{\delta}_{\tilde{j},\tilde{i}}$ ($\tilde{\delta}_{\tilde{j},\tilde{i}}$ is the Kronecker delta), and ϵ is a small enough number. Comparing the analytical and the numerical formulation yields matching results.

The collision probability computation is treated as already tested and verified, since it is carried out by means of Foster's method, publicly available on the CARA website.

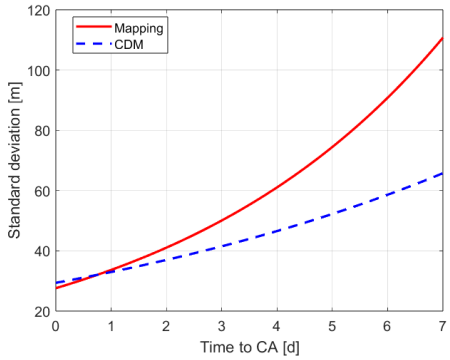

(a) $\hat{\mathbf{x}}_Q$ direction

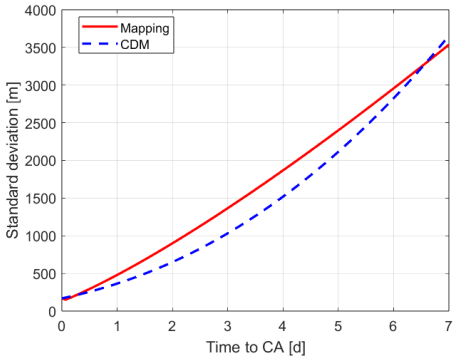

(b) $\hat{\mathbf{y}}_Q$ direction

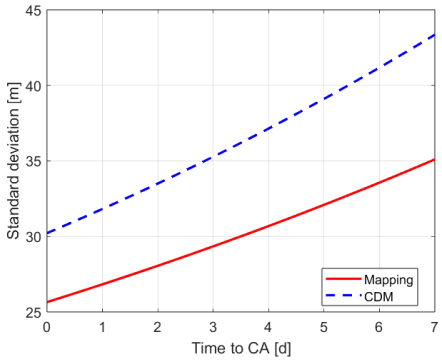

(c) $\hat{\mathbf{z}}_Q$ direction

Figure D.6: Results of the covariance-mapping algorithm, for an orbital class different from the reference one

D.3 Optimization Setup

The GPOPS-II license is purchased and employed to solve the OCP, thus the software is treated as already tested and verified. The correct formulation of the problem is checked. A new optimization problem is thus set up, for a sample case: an orbit-raising maneuver, for the same orbit presented in Table D.1. The optimization setup is the one described in Section 4.3, in terms of scaling, variables, simplifying assumptions, and settings. The *main* script and the *dynamics* function are also the same. What changes is the objective function, formulated as the maximization of the final SMA:

$$J = -\tilde{a}(t_f) \tag{D.3}$$

The optimization is carried out for a fixed-time interval, lasting half the orbital period of the spacecraft.

Two optimizations are performed: either the initial guess is the locally optimal steering law to maximize the SMA (exactly the optimum to find) or the initial guess is obtained by not maneuvering the sail, for a constant cone angle of 90 degrees (different from the optimum to find). Figure D.7 shows both the initial guesses and the outputted solutions, in terms of control profile: in both cases, it is verified that GPOPS-II can find the expected optimal control law.

The choice of the GPOPS-II settings (see Table 4.8) is justified by ensuring that, for several test cases,

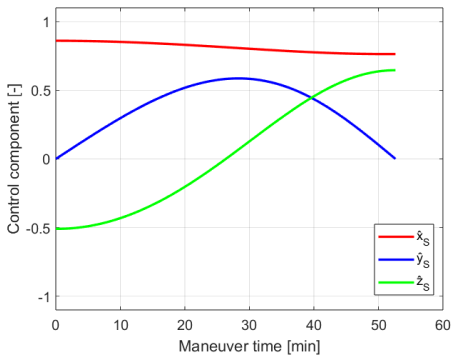

(a) Maneuvered initial guess

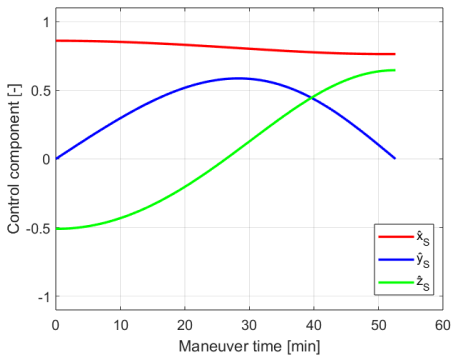

(b) Optimal solution, from maneuvered initial guess

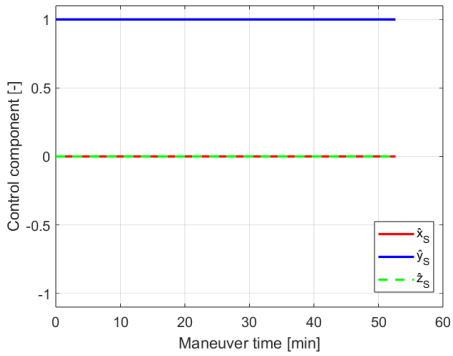

(c) Non-maneuvered initial guess

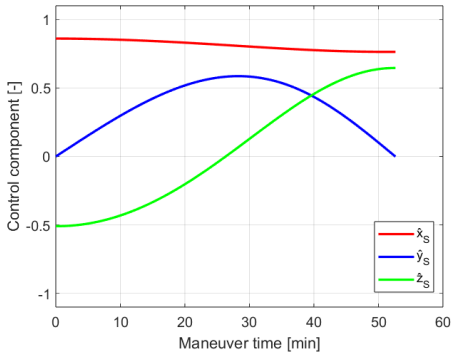

(d) Optimal solution, from non-maneuvered initial guess

Figure D.7: Time-evolution of the controls

the numerical integration of the solution results in errors below a set threshold. The thresholds are set to 1 m for position errors and 0.001 $\frac{\text{m}}{\text{s}}$ for velocity errors, loosening the integrator requirements by an order of magnitude (see Appendix A). The state is propagated at the same time nodes as in the GPOPS-II output, using the control history from GPOPS-II. Then, the difference between the resulting state history and the state from GPOPS-II is computed. For a generic solution, the evolution over time of the errors is shown in Fig. D.8, proving the discrepancies satisfy the accuracy requirements.

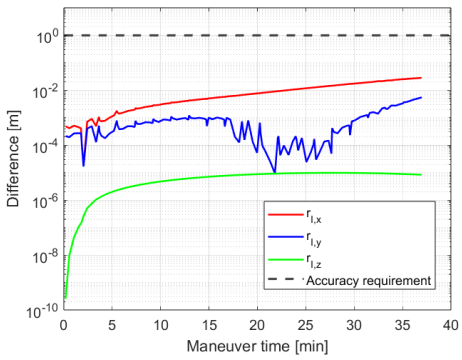

(a) Position discrepancy

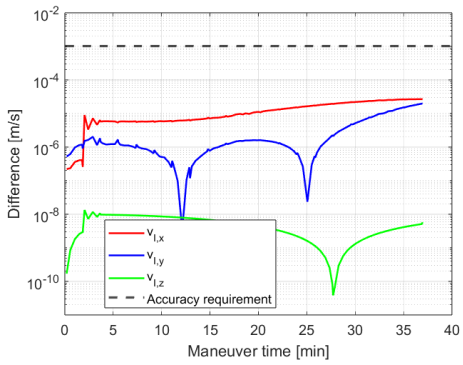

(b) Velocity discrepancy

Figure D.8: Discrepancies over time between the state histories from the numerical integration and from the GPOPS-II output, for the same optimal control profile

E Work Breakdown Structure

To organize the thesis workload, a research plan, in the form of a work breakdown structure, is built. All the implementation is carried out in MATLAB. The work packages are presented in the remainder of this section, showing both the amount of time spent to carry out the tasks of the specific work package and the time allocated for verification. As the thesis duration is (nominally) 32 weeks, Table E.1 presents the amount of time spent on each defined work package: the total sums up to 32 weeks. Figure E.1 shows the Gantt chart, with the visual representation of the distribution of the workload in time and the development of the different work packages as months progress.

0 Work package: Literature review [7.0 + 0.0 WEEKS]

- 0.1 Collect relevant pieces of literature
- 0.2 Identify research gap
- 0.3 Formulate research questions

A Work package: Create environment [1.5 + 0.5 WEEKS]

- A.1 Define reference frames
- A.2 Create rotation matrices
- A.3 Create environment
  - A.3.1 Create perturbing acceleration functions
  - A.3.2 Create eclipse model

B Work package: Create bodies [1 + 0.5 WEEKS]

- B.1 Create solar sail object
- B.2 Create Solar System bodies
  - B.2.1 Load ephemerides for the bodies of interest
- B.3 Create debris objects

C Work package: Create simulation scenario [0.5 + 0.5 WEEKS]

- C.1 Define minimum operating altitude for the sail
- C.2 Define simulation time of interest
- C.3 Define sail, debris, and conjunction parameters
- C.4 Select propagator and integrator

D Work package: Create collision avoidance scenario [2.5 + 1.0 WEEKS]

- D.1 Create debris state at closest approach based on the conjunction parameters
- D.2 Retrieve covariance data for the different orbital regimes
- D.3 Define the state transition matrix for the propagation of the covariance
- D.4 Define regression and mapping algorithm to generate uncertainties
- D.5 Select method to compute the probability of collision

E Work package: Analyze planetary equations [2.0 + 1.0 WEEKS]

- E.1 Retrieve sail attitude to maximize the rate of change of orbital elements

E.2 Assess performance of the locally optimal control laws

F Work package: Set up optimization scenarios [6.0 + 1.0 WEEKS]

F.1 Define optimal control problem (objective function, variables, constraints)
F.1 Familiarize with the chosen solver (GPOPS-II)
F.2 Code the optimization problem
F.2.1 Define main GPOPS-II functions
F.2.3 Define boundaries
F.2.4 Define scaling
F.3 Define initial guess generation
F.4 Set up time-iteration scheme
F.5 Choose GPOPS-II settings
F.6 Finalize algorithm for the different cases

G Work package: Run simulations [1.5 + 0.0 WEEKS]

G.1 Carry out optimization for all test scenarios and store data

H Work package: Analyze and post-process results [2.0 + 0.5 WEEKS]

H.1 Post-process results computing relevant quantities and analyze them
H.1.1 Maneuver time
H.1.2 Optimal control profile
H.2 Identify trends and correlations in the results
H.3 Generate plots to support analyses

I Work package: Finalize thesis document [3.0 + 0.0 WEEKS]

I.1 Summarize findings of literature review into a coherent introductory chapter
I.2 Describe algorithms and assumptions in the methodology chapter
I.3 Write thesis in "research paper" format, presenting the results
I.4 Add executive summary, conclusions, and recommendations
I.5 Refine thesis document

Work package	Allocated weeks
Literature review	7.0
A	2.0
B	1.5
C	1.0
D	3.5
E	3.0
F	7.0
G	1.5
H	2.5
I	3.0

Table E.1: Number of allocated weeks per thesis work package

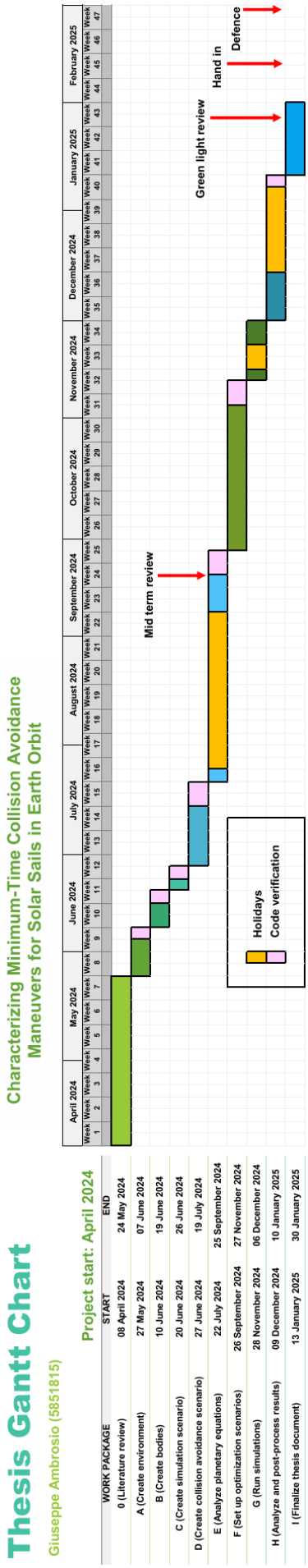

Figure E.1: Gantt chart of the thesis project

References

[1] Wakker, K. (2015). *Fundamentals of astrodynamics*. TU Delft Library.

[2] Wertz, J. R., & Larson, W. J. (1991). *Space mission analysis and design*. Kluwer.

[3] Byers, M., & Boley, A. (2023). *Who Owns Outer Space?: International Law, Astrophysics, and the Sustainable Development of Space* (1st ed.). Cambridge University Press. https://doi.org/10.1017/9781108597135

[4] Peter, N. (2024). The Space Debris Challenge to the Sustainability of the Space Economy. *European Review of International Studies*, *10*(3), 303–324. https://doi.org/https://doi.org/10.1163/21967415-10030003

[5] *ESA's Annual Space Environment Report 2024*. (2024). ESA's Space Debris Office.

[6] Klinkrad, H. (2006). *Space debris: Models and risk analysis*. Springer ; Published in association with Praxis Pub.

[7] Rossi, A. (2004). Population models of space debris. *Proceedings of the International Astronomical Union*, *2004*(IAUC197), 427–438. https://doi.org/10.1017/S1743921304008956

[8] Lewis, H. G., & Marsh, N. (2021). Deep time analysis of space debris and space sustainability. *8th European Conference on Space Debris*, *8*.

[9] Kessler, D. J., & Cour-Palais, B. G. (1978). Collision frequency of artificial satellites: The creation of a debris belt. *Journal of Geophysical Research: Space Physics*, *83*(A6), 2637–2646. https://doi.org/10.1029/JA083iA06p02637

[10] Mariappan, A., & Crassidis, J. L. (2023). Kessler's syndrome: A challenge to humanity. *Frontiers in Space Technologies*, *4*, 1309940. https://doi.org/10.3389/frspt.2023.1309940

[11] *ESA Space Debris Mitigation Requirements*. (2023). ESA Space Debris Mitigation Working Group.

[12] *State-of-the-Art of Small Spacecraft Technology*. (2024). NASA.

[13] Colombo, C., Rossi, A., Dalla Vedova, F., Braun, V., BastidaVirgili, B., & Krag, H. (2017). Drag and solar sail deorbiting: Re-entry time versus cumulative collision probability. *68th International Astronautical Congress*.

[14] Colombo, C., Rossi, A., Dalla Vedova, F., Francesconi, A., Bombardelli, C., Trisolini, M., Gonzalo, J. L., Di Lizia, P., Giacomuzzo, C., Khan, S. B., Garcia-Pelayo, R., Braun, V., Virgili, B. B., & Krag, H. (2018). Effects of passive de-orbiting through drag and solar sails and electrodynamic tethers on the space debris environment. *IAC-18-A6.2.8*.

[15] Colombo, C., Rossi, A., Francesconi, A., Dalla Vedova, F., Gonzalo, J. L., Braun, V., Virgili, B. B., & Krag, H. (2019). Long-term simulations to assess the effects of drag and solar sails on the space debris environment. *IAC-19-A6.4.2*.

[16] Underwood, C., Viquerat, A., Schenk, M., Taylor, B., Massimiani, C., Duke, R., Stewart, B., Fellowes, S., Bridges, C., Aglietti, G., Sanders, B., Masutti, D., & Denis, A. (2019). InflateSail de-orbit flight demonstration results and follow-on drag-sail applications. *Acta Astronautica*, *162*, 344–358. https://doi.org/10.1016/j.actaastro.2019.05.054

[17] Kelly, P. W., Bevilacqua, R., Mazal, L., & Erwin, R. S. (2018). TugSat: Removing Space Debris from Geostationary Orbits Using Solar Sails. *Journal of Spacecraft and Rockets*, *55*(2), 437–450. https://doi.org/10.2514/1.A33872

[18] McInnes, C. R. (1999). *Solar sailing: Technology, dynamics and mission applications*. Springer.

[19] Fu, B., Sperber, E., & Eke, F. (2016). Solar sail technology—A state of the art review. *Progress in Aerospace Sciences*, *86*, 1–19. https://doi.org/10.1016/j.paerosci.2016.07.001

[20] Wright, J. L. (1993). *Space sailing* (2nd print). Gordon & Breach.

[21] Ceriotti, M., & May-Wilson, G. (2021). A simple control law for reducing the effective characteristic acceleration of a solar sail. *Advances in Space Research*, *67*(9), 2865–2877. https://doi.org/10.1016/j.asr.2020.04.028

[22] Jordaan, H. W. (2016). Spinning Solar Sail: The Deployment and Control of a Spinning Solar Sail Satellite.

[23] Wie, B. (2004). Solar Sail Attitude Control and Dynamics, Part 1. *Journal of Guidance, Control, and Dynamics*, *27*(4), 526–535. https://doi.org/10.2514/1.11134

[24] Garner, C. E. (2000). A solar sail design for a mission to the near-interstellar medium [ISSN: 0094243X]. *AIP Conference Proceedings*, *504*, 947–961. https://doi.org/10.1063/1.1290891

[25] Mori, O., Shirasawa, Y., Mimasu, Y., Tsuda, Y., Sawada, H., Saiki, T., Yamamoto, T., Yonekura, K., Hoshino, H., Kawaguchi, J., & Funase, R. (2014). Overview of IKAROS Mission. In M. Macdonald (Ed.), *Advances in Solar Sailing* (pp. 25–43). Springer Berlin Heidelberg. https://doi.org/10.1007/978-3-642-34907-2_3

[26] Tsuda, Y., Mori, O., Funase, R., Sawada, H., Yamamoto, T., Saiki, T., Endo, T., Yonekura, K., Hoshino, H., & Kawaguchi, J. (2013). Achievement of IKAROS — Japanese deep space solar sail demonstration mission. *Acta Astronautica*, *82*(2), 183–188. https://doi.org/10.1016/j.actaastro.2012.03.032

[27] Johnson, L., Whorton, M., Heaton, A., Pinson, R., Laue, G., & Adams, C. (2011). NanoSail-D: A solar sail demonstration mission. *Acta Astronautica*, *68*(5-6), 571–575. https://doi.org/10.1016/j.actaastro.2010.02.008

[28] Ridenoure, R., Munakata, R., Diaz, A., Wong, S., Plante, B., Stetson, D., Spencer, D., & Foley, J. (2015). LightSail Program Status: One Down, One to Go.

[29] Mansell, J. R., Bellardo, J. M., Betts, B., Plante, B., & Spencer, D. A. (2023). LightSail 2 Solar Sail Control and Orbit Evolution. *Aerospace*, *10*(7), 579. https://doi.org/10.3390/aerospace10070579

[30] Johnson, L., Betts, E., Heaton, A., Jones, C., McNutt, L., Pruitt, M., Stott, J., Wallace, D., Wilson, R., Castillo-Rogez, J., Lantoine, G., Seybold, C., & Sweetser, T. (2022). Near Earth Asteroid Scout - Mission Update. *36th Annual Small Satellite Conference*.

[31] Dono, A., Hendriks, T., & Wilkie, K. (2024). Navigation for the ACS3 solar sail mission.

[32] Sawada, H., Mori, O., Okuizumi, N., Shirasawa, Y., Miyazaki, Y., Natori, M., Matunaga, S., Furuya, H., & Sakamoto, H. (2011). Mission Report on The Solar Power Sail Deployment Demonstration of IKAROS. *52nd AIAA/ASME/ASCE/AHS/ASC Structures, Structural Dynamics and Materials Conference*. https://doi.org/10.2514/6.2011-1887

[33] Alhorn, D. C., Casas, J. P., Agasid, E. F., Adams, Charles L., Laue, G., Kitts, C., & O'Brien, S. (2011). NanoSail-D: The Small Satellite That Could! *25th Annual AIAA/USU Conference on Small Satellites*.

[34] Spencer, D. A., Betts, B., Bellardo, J. M., Diaz, A., Plante, B., & Mansell, J. R. (2021). The LightSail 2 solar sailing technology demonstration. *Advances in Space Research*, *67*(9), 2878–2889. https://doi.org/10.1016/j.asr.2020.06.029

[35] Wilkie, W. K., Fernandez, J., Stohlman, O. R., Schneider, N., Dean, G., Kang, J. H., Cook, S., Warren, J., Brown, P., Denkins, T., Horner, S., Tapio, E., Straubel, M., Richter, M., & Heiligers, J. (2021). Overview of the NASA Advanced Composite Solar Sail System (ACS3) Technology Demonstration Project. *AIAA Scitech 2021 Forum*. https://doi.org/10.2514/6.2021-1260

[36] Merz, K., Bastida Virgili, B., Braun, V., Flohrer, T., Funke, Q., Krag, H., & Lemmens, S. (2017). Current Collision Avoidance service by ESA's Space Debris Office.

[37] Flohrer, T., Braun, V., Krag, H., Merz, K., Lemmens, S., Virgili, B. B., & Funke, Q. (2015). Operational collision avoidance at ESOC.

[38] Li, J.-S., Yang, Z., & Luo, Y.-Z. (2022). A review of space-object collision probability computation methods. *Astrodynamics*, *6*(2), 95–120. https://doi.org/10.1007/s42064-021-0125-x

[39] Gonzalo, J. L., Colombo, C., & Di Lizia, P. (2021). Analytical Framework for Space Debris Collision Avoidance Maneuver Design. *Journal of Guidance, Control, and Dynamics*, *44*(3), 469–487. https://doi.org/10.2514/1.G005398

[40] Flohrer, T., Krag, H., & Klinkrad, H. (2008). Assessment and Categorization of TLE Orbit Errors for the US SSN Catalogue.

[41] *Recommendation for Space Data System Standards - Conjunction Data Message*. (2021). NASA - The Consultative Committee for Space Data Systems.

[42] Merz, K., Siminski, J., Bastida Virgili, B., Braun, V., Flegel, S., Flohrer, T., Funke, Q., Horstmann, A., Lemmens, S., Letizia, F., Mclean, F., Sanvido, S., & Schaus, V. (2021). ESA's Collision Avoidance Service: Current Status and Special Cases.

[43] Dural, S., Tugcular, U., & Daser, B. (2021). General Collision Avoidance Maneuver Decision Algorithm.

[44] Spencer, D. B., Sorge, M. E., & Skinner, M. A. (2024). Establishing "norms of behavior" for satellite collision avoidance maneuver planning. *Journal of Space Safety Engineering*, *11*(1), 120–126. https://doi.org/10.1016/j.jsse.2023.11.012

[45] Aida, S. (2016). Conjunction Risk Assessment and Avoidance Maneuver Planning Tools.

[46] Bombardelli, C., & Hernando-Ayuso, J. (2015). Optimal Impulsive Collision Avoidance in Low Earth Orbit. *Journal of Guidance, Control, and Dynamics*, *38*(2), 217–225. https://doi.org/10.2514/1.G000742

[47] Salemme, G., Armellin, R., & Di Lizia, P. (2020). Continuous-thrust collision avoidance manoeuvres optimization. *AIAA Scitech 2020 Forum*. https://doi.org/10.2514/6.2020-0231

[48] Palermo, M. F., DI Lizia, P., & Armellin, R. (2021). Numerically efficient methods for low-thrust collision avoidance manoeuvre design. *8th European Conference on Space Debris*, *8*.

[49] De Vittori, A., Palermo, M. F., Di Lizia, P., & Armellin, R. (2022). Low-Thrust Collision Avoidance Maneuver Optimization. *Journal of Guidance, Control, and Dynamics*, *45*(10), 1815–1829. https://doi.org/10.2514/1.G006630

[50] De Vittori, A., Dani, G., Di Lizia, P., & Armellin, R. (2023). Low-thrust collision avoidance design for LEO missions with return to nominal orbit.

[51] Armellin, R. (2021). Collision avoidance maneuver optimization with a multiple-impulse convex formulation. *Acta Astronautica*, *186*, 347–362. https://doi.org/10.1016/j.actaastro.2021.05.046

[52] Pavanello, Z., Pirovano, L., Armellin, R., De Vittori, A., & Di Lizia, P. (2024). A Convex Optimization Method for Multiple Encounters Collision Avoidance Maneuvers. *AIAA SCITECH 2024 Forum*. https://doi.org/10.2514/6.2024-0845

[53] Kim, E.-H., Kim, H.-D., & Kim, H.-J. (2012). A Study on the Collision Avoidance Maneuver Optimization with Multiple Space Debris. *Journal of Astronomy and Space Sciences*, *29*(1), 11–21. https://doi.org/10.5140/JASS.2012.29.1.011

[54] Morselli, A., Armellin, R., Di Lizia, P., & Bernelli Zazzera, F. (2014). Collision Avoidance Maneuver Design based on Multi-Objective Optimization. *Advances in Astronautical Sciences*, *152*.

[55] Seong, J.-D., & Kim, H.-D. (2015). Collision avoidance maneuvers for multiple threatening objects using heuristic algorithms. *Proceedings of the Institution of Mechanical Engineers, Part G: Journal of Aerospace Engineering*, *229*(2), 256–268. https://doi.org/10.1177/0954410014530678

[56] Seong, J.-D., & Kim, H.-D. (2016). Multiobjective optimization for collision avoidance maneuver using a genetic algorithm. *Proceedings of the Institution of Mechanical Engineers, Part G: Journal of Aerospace Engineering*, *230*(8), 1438–1447. https://doi.org/10.1177/0954410015611699

[57] Gonzalo, J. L., Colombo, C., & Di Lizia, P. (2018). Analysis and design of collision avoidance maneuvers for passive de-orbiting missions. *AAS 18-357*, 2189–2208.

[58] Patera, R. P., & Peterson, G. E. (2003). Space Vehicle Maneuver Method to Lower Collision Risk to an Acceptable Level. *Journal of Guidance, Control, and Dynamics*, *26*(2), 233–237. https://doi.org/10.2514/2.5063

[59] Bombardelli, C., Hernando-Ayuso, J., & Pelayo, R. G. (2014). Collision avoidance maneuver optimization.

[60] Hernando-Ayuso, J., & Bombardelli, C. (2021). Low-Thrust Collision Avoidance in Circular Orbits. *Journal of Guidance, Control, and Dynamics*, *44*(5), 983–995. https://doi.org/10.2514/1.G005547

[61] Carzana, L., Visser, P., & Heiligers, J. (2022a). Locally optimal control laws for Earth-bound solar sailing with atmospheric drag. *Aerospace Science and Technology*, *127*, 107666. https://doi.org/10.1016/j.ast.2022.107666

[62] Mengali, G., & Quarta, A. A. (2005). Near-Optimal Solar-Sail Orbit-Raising from Low Earth Orbit. *Journal of Spacecraft and Rockets*, *42*(5), 954–958. https://doi.org/10.2514/1.14184

[63] *U.S. Standard Atmosphere 1976*. (1976). United States Air Force.

[64] Klinkrad, H., & Fritsche, B. (1999). Orbit and attitude perturbations due to aerodynamics and radiation pressure.

[65] Carzana, L., Visser, P., & Heiligers, J. (2022b). A new model for the planetary radiation pressure acceleration for solar sails. *2022 AAS/AIAA Astrodynamics Specialist Conference*.

[66] Kelly, P., & Bevilacqua, R. (2019). An optimized analytical solution for geostationary debris removal using solar sails. *Acta Astronautica*, *162*, 72–86. https://doi.org/10.1016/j.actaastro.2019.05.055

[67] McInnes, C. R., & Brown, J. C. (1990). Solar sail dynamics with an extended source of radiation pressure. *Acta Astronautica*, *22*, 155–160. https://doi.org/10.1016/0094-5765(90)90017-F

[68] Neta, B., & Vallado, D. (1998). On Satellite Umbra/Penumbra Entry and Exit Positions. *The Journal of the Astronautical Sciences*, *46*(1), 91–103. https://doi.org/10.1007/BF03546195

[69] Curtis, H. (2020). *Orbital Mechanics for Engineering Students*. Elsevier. https://doi.org/10.1016/B978-0-08-102133-0.09982-7

[70] Pollock, K. R. (1994, September). *An Analysis Of Orbital Propagators for Low Earth Orbit Rendezvous* [, University of Virginia].

[71] Verner, J. H. (2010). Numerically optimal Runge–Kutta pairs with interpolants. *Numerical Algorithms*, *53*(2-3), 383–396. https://doi.org/10.1007/s11075-009-9290-3

[72] Shampine, L. F., & Reichelt, M. W. (1997). The MATLAB ODE Suite. *SIAM Journal on Scientific Computing*, *18*(1), 1–22. https://doi.org/10.1137/S1064827594276424

[73] Kelly, P., & Bevilacqua, R. (2021). Geostationary debris mitigation using minimum time solar sail trajectories with eclipse constraints. *Optimal Control Applications and Methods*, *42*(1), 279–304. https://doi.org/10.1002/oca.2676

[74] Sumanth, M. R. (2019). Computation of Eclipse Time for Low-Earth Orbiting Small Satellites. *International Journal of Aviation, Aeronautics, and Aerospace*. https://doi.org/10.15394/ijaaa.2019.1412

[75] *IADC Space Debris Mitigation Guidelines*. (2021, June). Inter-Agency Space Debris Coordination Committee.

[76] Gamez Losada, F., Visser, P., & Heiligers, J. (2024). Fundamentals of Solar-Sail Transfers Around Planetary Bodies. *Proceedings of the 29th International Symposium on Space Flight Dynamics*.

[77] *Assessment of Risk Event Statistics (ARES)*. (2021). ESA's Space Debris Office.

[78] Chan, K. (2004). Short-Term vs. Long-Term Spacecraft Encounters. *AIAA/AAS Astrodynamics Specialist Conference and Exhibit*. https://doi.org/10.2514/6.2004-5460

[79] Alfano, S., & Oltrogge, D. (2018). Probability of Collision: Valuation, variability, visualization, and validity. *Acta Astronautica*, *148*. https://doi.org/10.1016/j.actaastro.2018.04.023

[80] Foster, J. L. (1992). *A parametric analysis of orbital debris collision probability and maneuver rate for space vehicles*. NASA.
[81] Alfano, D. S. (2007). Review of Conjunction Probability Methods.
[82] Capuano, V., Shehaj, E., Botteron, C., Blunt, P., & Farine, P.-A. (2017). GNSS/INS/Star Tracker Integration for Real-Time On-Board Autonomous Orbit and Attitude Determination in LEO, MEO, GEO and Beyond.
[83] Alfriend, K. T., Akella, M. R., Frisbee, J., Foster, J. L., Lee, D.-J., & Wilkins, M. (1999). Probability of Collision Error Analysis. *Space Debris*, *1*, 21–35.
[84] Braun, V., Horstmann, A., Reihs, B., Lemmens, S., Merz, K., & Krag, H. (2019). Exploiting Orbital Data and Observation Campaigns to Improve Space Debris Models. *The Journal of the Astronautical Sciences*, *66*(2), 192–209. https://doi.org/10.1007/s40295-019-00155-6
[85] Sánchez-Ortiz, N., Domínguez-González, R., Krag, H., & Flohrer, T. (2015). Impact on mission design due to collision avoidance operations based on TLE or CSM information. *Acta Astronautica*, *116*, 368–381. https://doi.org/10.1016/j.actaastro.2015.04.017
[86] Schiff, C. (2006). Adapting Covariance Propagation to Account for the Presence of Modeled and Unmodeled Maneuvers. *AIAA/AAS Astrodynamics Specialist Conference and Exhibit*. https://doi.org/10.2514/6.2006-6294
[87] Rugh, W. J. (1996). *Linear system theory* (2nd ed). Prentice Hall.
[88] Gonzalo, J. L., Colombo, C., & Di Lizia, P. (2019). Drag- and SRP-induced effects in uncertainty evolution for close approaches. *4th International Workshop on Key Topics in Orbit Propagation Applied to Space Situational Awareness*.
[89] Song-hua, H., & Jing-shi, T. (2023). Reference Dynamic Models for Space Debris Orbit Prediction. *Chinese Astronomy and Astrophysics*, *47*(4), 872–893. https://doi.org/10.1016/j.chinastron.2023.11.003
[90] Bojkov, B., & Luus, R. (1996). Optimal control of nonlinear systems with unspecified final times. *Chemical Engineering Science*, *51*(6), 905–919. https://doi.org/10.1016/0009-2509(95)00340-1
[91] Longuski, J. M., Guzmán, J. J., & Prussing, J. E. (2014). *Optimal Control with Aerospace Applications*. Springer New York. https://doi.org/10.1007/978-1-4614-8945-0
[92] Song, Y., & Gong, S. (2019a). Solar-sail deep space trajectory optimization using successive convex programming. *Astrophysics and Space Science*, *364*(7), 106. https://doi.org/10.1007/s10509-019-3597-x
[93] Heiligers, J., Mingotti, G., & McInnes, C. (2014). Optimisation of solar sail interplanetary heteroclinic connections. *IAA-AAS-DyCoSS2-03-04*, *153*.
[94] Morante, D., Sanjurjo Rivo, M., & Soler, M. (2021). A Survey on Low-Thrust Trajectory Optimization Approaches. *Aerospace*, *8*(3), 88. https://doi.org/10.3390/aerospace8030088
[95] Topputo, F., & Zhang, C. (2014). Survey of Direct Transcription for Low-Thrust Space Trajectory Optimization with Applications. *Abstract and Applied Analysis*, *2014*, 1–15. https://doi.org/10.1155/2014/851720
[96] Patterson, M. A., & Rao, A. V. (2014). GPOPS-II: A MATLAB Software for Solving Multiple-Phase Optimal Control Problems Using hp-Adaptive Gaussian Quadrature Collocation Methods and Sparse Nonlinear Programming. *ACM Transactions on Mathematical Software*, *41*(1), 1–37. https://doi.org/10.1145/2558904
[97] Mall, K. (2018). Advancing Optimal Control Theory Using Trigonometry For Solving Complex Aerospace Problems. https://hammer.purdue.edu/articles/thesis/Advancing_Optimal_Control_Theory_Using_Trigonometry_For_Solving_Complex_Aerospace_Problems/7418204/1
[98] Song, Y., & Gong, S. (2019b). Solar sail trajectory optimization of multi-asteroid rendezvous mission. *Acta Astronautica*, *157*, 111–122. https://doi.org/10.1016/j.actaastro.2018.12.016

[99] Wächter, A., & Biegler, L. T. (2006). On the implementation of an interior-point filter line-search algorithm for large-scale nonlinear programming. *Mathematical Programming*, *106*(1), 25–57. https://doi.org/10.1007/s10107-004-0559-y

[100] Babuška, I. (1988). The p and h-p Versions of the Finite Element Method: The State of the Art [Series Title: ICASE/NASA LaRC Series]. In *Finite Elements* (pp. 199–239). Springer New York. https://doi.org/10.1007/978-1-4612-3786-0_10

[101] Patterson, M. A., & Rao, A. V. (2012). Exploiting Sparsity in Direct Collocation Pseudospectral Methods for Solving Optimal Control Problems. *Journal of Spacecraft and Rockets*, *49*(2), 354–377. https://doi.org/10.2514/1.A32071

[102] Patterson, M. A., & Rao, A. V. (2016). *A General-Purpose MATLAB Software for Solving Multiple-Phase Optimal Control Problems Version 2.3*.

[103] Braun, V., Flohrer, T., Krag, H., Merz, K., Lemmens, S., Bastida Virgili, B., & Funke, Q. (2016). Operational support to collision avoidance activities by ESA's space debris office. *CEAS Space Journal*, *8*(3), 177–189. https://doi.org/10.1007/s12567-016-0119-3

[104] Stewart, J. (2008). *Calculus: Early transcendentals* (6th ed). Thomson Brooks/Cole.

[105] Macdonald, M., & McInnes, C. R. (2005a). Analytical Control Laws for Planet-Centered Solar Sailing. *Journal of Guidance, Control, and Dynamics*, *28*(5), 1038–1048. https://doi.org/10.2514/1.11400

[106] Macdonald, M., & McInnes, C. R. (2005b). Realistic Earth Escape Strategies for Solar Sailing. *Journal of Guidance, Control, and Dynamics*, *28*(2), 315–323. https://doi.org/10.2514/1.5165

[107] Green, A. J. (1977, September). *Optimal escape trajectory from a high Earth orbit by use of solar radiation pressure* [, Massacheussets Institute of Technology].

[108] Swokowski, E. W. (1979). *Calculus with analytic geometry* (2nd ed) [OCLC: 1338523975]. Prindle, Weber & Schmidt.

[109] Montenbruck, O., & Gill, E. (2000). *Satellite Orbits*. Springer Berlin Heidelberg. https://doi.org/10.1007/978-3-642-58351-3